Gas Embolotherapy: Bubble Evolution in Acoustic Droplet Vaporization and Design of a Benchtop Microvascular Model

by

Zheng Zheng Wong

A dissertation submitted in partial fulfillment
of the requirements for the degree of
Doctor of Philosophy
(Biomedical Engineering)
in the University of Michigan
2009

Doctoral Committee:

Associate Professor Joseph L. Bull, Chair
Professor J. Brian Fowlkes
Professor William W. Schultz
Associate Professor Shuichi Takayama

Dedicated to

my parents, Mr Wong Kim Sang & Mdm Lee Mee Chin

my wife, Chun-Ling

my sister, Shing Liu

my brother-in-law and sister, You Jiang and Shing Dih

my daughter, Jiah-Yueh

Acknowledgements

My graduate student education has been long but fruitful, and I would like to thank all the people who have helped me along the way. First, I thank my dissertation committee members, Professors Joseph Bull, William Schultz, Brian Fowlkes and Shuichi Takayama, for their insightful comments and kind patience. My advisor, Prof. Bull, is one of the most understanding and supportive people I have ever met, and is unequivocally the best "boss" I have ever worked for, though his style of mentoring has always made me feel more like his colleague than his subordinate. I am thankful to Prof Fowlkes for giving very useful advice during our semi-monthly group meetings. I am very grateful to an excellent mentor outside of my dissertation committee, Dr. Oliver Kripfgans, who is a great experimentalist with a great sense of humor and has helped me tremendously in the setup and usage of the ultra-high speed camera, and many other aspects of my experiments. If not for another of my mentors, Prof. Albert Yee, I might not have entered graduate school at all. I thank him for believing in me and sharing with me his wisdom and experience.

I really appreciate the help from, and the stimulating discussions with, my previous and present labmates (James Stephen, Andres Calderon, Yu-Chun Lin, Marty Schlicht, Stan Samuel, Adnan Qamar, Ambroise Duprey), as

well as colleagues from other labs (Kevin Haworth, Mario Fabiilli, Andrea Lo, Tzu-Yin Wang, Terry Zhu, Dan Huh, Albert Chueh, Jon Song, Dan Estes, Jeff Uram), throughout my stay at U of M. In particular, I would like to acknowledge James' and Marty's generous time and efforts in machining my experimental devices and molds.

My research could not have made progress without the administrative and computer support from departmental colleagues and friends, such as Tonya Thompson, Chuck Nicholas, Dan McHugh, Maria Steele, Dana Jackson, Kristin Romelhardt. Their friendship has also made my working environment much more pleasant.

In addition, I thank my other friends (Jason Smith, Stanley Shih, Hui-Chun Chang, Glenda Rhodes, Shu-Hui Hsu, Ying Zheng), from within and outside the BME department, who have helped me get through smooth and rough days of my graduate student life with their warm friendship. My thoughts go out to my departed friends, Teddy Yong and Lee Hong Wee, because their tragedies have enlightened me on the unpredictable's of life.

I wish to acknowledge A*STAR (Singapore) and NIH for their funding of my graduate education.

Last, but certainly not least, I thank my parents, wife, sisters, brother-in-law and daughter for their love and support, and seek their pardon for my not spending enough time with them.

Table of Contents

List of Figures

List of Tables

List of Appendices

Abstract

This work was motivated by an ongoing development of a potential embolotherapy technique to occlude blood flow to tumors using gas bubbles selectively formed by in vivo acoustic droplet vaporization (ADV) of liquid perfluorocarbon droplets. Mechanisms behind the ADV, transport and lodging of emboli need to be understood before gas embolotherapy can translate to the clinic.

Evolution of a bubble from acoustic droplet vaporization in a rigid tube, under physiological and room temperature conditions, was observed via ultra-high speed imaging. Effective radii and radial expansion ratios were obtained by processing the images using ImageJ software. At physiological temperature, a radial expansion ratio of 5.05 was attained, consistent with theoretical prediction. The initial radial growth rate was linear, after which the growth rate increased proportionally with square root of time. Non-dimensionalization revealed that the subsequent growth rate also varied inversely with square root of initial radius. Eventually growth became asymptotic. No collapse was observed.

A theoretical model derived from a modified Bernoulli equation, and a computational model by Ye & Bull (2004), were compared respectively with experimental results. Initial growth rates were predicted correctly by both

models. Experimental results showed heavy damping of growth rate as the bubble grew towards the wall, whereas both models predicted an overshoot in growth followed by multiple oscillations. The theoretical model broke down near the wall; the computational model gave a reasonable bubble shape near the wall but would require correct initial pressure values to be accurate.

At room temperature, the expansion ratio shot to 1.43 initially and oscillated down to 1.11, far below the theoretical prediction. Failure of the bubble to expand fully could be due to unconsumed or condensed liquid perfluorocarbon.

A new fabrication method via non-lithographic means was devised to make a circular-lumen microchannel out of PDMS, with a diameter as small as 80 microns to mimic the size of a medium arteriole. The microchannel was endothelialized successfully, with a fairly homogeneous distribution along the length. Cell viability assays confirmed the viability of cells maintained in the microchannel. Bubble motion experiments performed with the benchtop microvascular model demonstrated its feasibility.

Chapter 1

Introduction

1.1 Overview of Embolotherapy

In interventional radiology, embolization refers to the procedure in which blood vessels are closed off with various foreign substances in order to achieve partial or complete occlusion of blood flow. It is commonly used for reasons such as:

- To control bleeding from injury, a tumor, a stomach ulcer or other cause on an emergency basis
- To decrease blood loss and allow better visualization of the tumor in the brain, spine and head/neck during surgery
- To occlude blood vessels that feed a tumor, with the ultimate goal of starving the tumor (this form of cancer therapy is often termed embolotherapy ; if drugs are administered via the embolic materials, it is termed chemoembolization or chemoembolotherapy)
- To treat other conditions where surgery is very difficult or undesirable, e.g. uterine fibroids (as an alternative to hysterectomy), arteriovenous

malformations, brain aneurysms, hemangiomas (these are often found on the face where surgical removal might leave an unsightly scar)

Since the early experiments of using silicon tubings and balloons, many different materials have been introduced through intravascular catheters and percutaneously to occlude blood flow, e.g. absorbable materials such as blood clot, cellulose, gelatin sponge, or nonabsorbable materials such as particulates, coils, streamers.

Currently, embolotherapy methods are being investigated in a research setting or are used as a last resort when conventional therapy has failed [4]. Embolotherapy's greatest potential lies in treating hypervascularized tumors which have a large number of blood vessels, e.g. in cancer of the liver and kidneys. Hepatocellular carcinoma (HCC) is the most common form of liver cancer, occurring in 2–30 per 100,000 males each year, and causes an estimated 1,250,000 deaths worldwide annually.

HCC has been difficult to treat with traditional methods because the accompanying liver cirrhosis makes most patients (70–85%) ineligible for treatment by resection, and the results of systemic chemotherapy have been disappointing, with no appreciable impact on survival rates. HCC has been treated effectively using embolotherapy in which localized drug delivery was included in the procedure [22]. Several articles in [7] have also indicated successful treatment by embolotherapy, including 78% tumor necrosis, suggesting that partial necrosis is sufficient for remission. Another suitable application of embolotherapy is renal carcinoma, the most common cancer in the urinary tract, accounting for ~3% of malignancies overall.

Most previous embolotherapy work has involved complicated procedures, requiring either surgical exposure of vessels near the target region or very selective catheter placement to minimize embolization of normal tissue. One of the major factors in the success of embolotherapy in treating tumors is the ability to direct and confine treatment to the target area. These difficulties are partially responsible for embolotherapy being used primarily as a last resort after trying conventional methods. A potentially better method is gas embolotherapy which will use gas bubbles instead of solid or liquid emboli.

1.2 Gas Embolotherapy

The envisioned gas embolotherapy scenario is as follows (see Figure 1.1 for an illustration). Blood flow carries superheated dodecafluoropentane (DDFP, C_5F_{12}) droplets, each encapsulated in an albumin shell, into the tumor region, where high-intensity ultrasound is used to initiate acoustic droplet vaporization (ADV) to form bubbles near the desired occlusion sites. Although the boiling point of DDFP (29°C) at atmospheric pressure is lower than body temperature, the superheated DDFP is maintained in droplets via the albumin shell and these droplets may circulate freely without sticking until activated by the ultrasound.

Although microbubbles have been used as contrast agents for 20 years, the use of gas emboli formed by ultrasonic activation of superheated droplets is a relatively new approach. These DDFP bubbles have been observed to

persist for long times in blood, ranging from over 30 minutes when exposed to flow to substantially over 2 hours (maximum time >2 days) when static. It has been shown that 90 minutes of myocardial ischemia leads to irreversible injury even when tissue is reperfused [12]. While it is expected that tumors tolerate hypoxia much better than myocytes, the extended persistence times of the DDFP bubbles may be sufficient to cause tumor necrosis. In addition, these emboli may potentially be used as drug delivery vehicles.

Gas embolotherapy has some inherent limitations of embolotherapy but it offers the following advantages:

- Less invasive (as simply as intravenous infusion)
- More precise delivery of emboli (standard diagnostic ultrasound can assist in imaging and positioning the droplets in the desired region)
- Lower risk of causing collateral damage to healthy tissue (once the region of interest has been targeted, high intensity ultrasound can be focused on the specific region for ADV)
- Facilitates drug delivery to the targeted sites (chemotherapeutic drugs can be added to the droplets and be released into the tumor region during ADV)

1.3 Gas Embolotherapy: Research Roadmap

Before the translation of gas embolotherapy to the clinic, it must be determined how and where this methodology can be used to produce localized embolization. This in turn requires understanding the mechanisms

of the three major steps of gas embolotherapy --- ADV, transport and lodging of the emboli. Only when the underlying mechanisms are elucidated can we expect to develop delivery strategies which will most likely need to be tailored to the specific application. Figure 1.2 shows a roadmap of the research topics in gas embolotherapy, with the related literature indicated on the figure.

Research in gas embolotherapy was pioneered by efforts concentrating on the ultrasound aspects of ADV and involving timelines of several microseconds. The only work on the fluid mechanics aspects of ADV, prior to the work described herein, had been done via computational modeling.

The work in this thesis constitutes the first experimental investigation of the fluid mechanics aspects of ADV, where timelines stretching into hundreds of microseconds, i.e. longer than those in previous research, have been used in the experiments. The fluid mechanics aspects of ADV covered in this thesis include:- experimental characterization of the ADV process (including the effect of droplet and flow parameters on the mechanics of bubble evolution); assessment of the validity of the computational model's predictions (including the predicted stresses from high pressure during ADV and their potential bioeffects); investigation of the effect of temperature; and coalescence of bubbles during ADV.

After ADV forms bubbles, it is crucial for these bubbles to be transported to the desired sites. Our research group has already made progress in investigating the fluid mechanics related to the bubble transport for gas embolotherapy. Benchtop experiments in transport of long air

bubbles (suspended in water) through an acrylic model of a single symmetric bifurcation have revealed that there is a critical capillary number below which the bubble does not split and moves entirely into the upper branch, and that the critical capillary number increases with roll angle and parent tube diameter [5]. Similar experiments of transport in an acrylic model with multiple bifurcations have demonstrated that bubbles can either stick at one of the second bifurcations or in the second-generation daughter tubes, even though the flow rate in the parent tube is constant [9].

Part of the work in this thesis contributes to the knowledge of bubble transport, via the design of a benchtop microvascular model and using it to investigate potential bioeffects of bubble transport.

The final major step in gas embolotherapy is lodging the transported bubbles at the desired sites. Although the work in this thesis does not address bubble lodging directly, its findings will help navigate the critical path leading to the bubble lodging.

1.4 Bubble Evolution in Acoustic Droplet Vaporization

Bubble expansion in a tube is different from an expansion away from boundaries. The existence of interaction between an expanding bubble and an elastic boundary has been demonstrated by [3] in a high-speed photographic study involving a laser-induced cavitation bubble and polyacrylamide gel. Their bubble was unconfined on the side away from the elastic boundary and of a much larger scale with its diameter ~O(1-3 mm).

No previous experimental studies have reported wall stresses resulting from droplet vaporization in a tube. Direct numerical simulation of bubble expansion in ADV has demonstrated that the wall pressure is typically highest at the start of the bubble expansion but the maximum wall shear stress occurs at a later time. [35, 37] The computational simulation has also found that smaller droplet diameters, relative to the vessel radius, have less potential to damage vessel walls. An indirect approach for validating the computational predictions is to compare them with experimental images of bubble evolution. As the bubble evolution occurs on a superfast timescale (<< 1 s), the best method of capturing images of the evolution is to rely on ultra-high speed imaging.

Vaporization of droplets in a flow tube significantly larger than the droplet diameter, due to their usage of droplets of mostly single-digit micron diameter, was imaged by [17, 18] using ultra-high speed video microscopy. It was observed that :-

- Droplets deformed when exposed to ultrasound, agreeing well with the theoretical prediction of up to 15% deformation
- Droplets underwent translational motion in the acoustic field with an average 2.6 µm peak to peak displacement, at which point vaporization occurred
- Nucleation started at the proximal and distal positions on the central axis of motion, with a second nucleation site typically observed at a diametrically opposite position

- The acoustic pressure threshold for ADV could be inversely related to the droplet size

A field of research that might be related to ADV is explosive boiling [1, 2, 27]. The major differences are that, more often than not, the energy for the phase change is via direct heating, the liquid droplets in explosive boiling are not enclosed by a shell of a third-party material and that the droplets are usually fairly large (about 1 mm in diameter). Theoretical work [23, 29] on explosive boiling has also developed hand in hand with the experimental work [13, 14, 25].

Other theoretical work on bubbles [24, 26, 38] might provide useful insight in the phenomenon of ADV, though their assumptions might not apply fully to ADV.

High-speed camera and video imaging, as well as other types of imaging, have often been employed to investigate bubble dynamics [8, 15, 28] and coalescence phenomenon [11].

1.5 Benchtop Model of a Microvessel

There exists a need for an in vitro model of a microvessel in such fields of biomedical research as circulation, hematology, vascular biology, anesthesiology (especially regarding thrombosis and gas embolism), interventional radiology, etc.

Ideally, the microvessel model should have physiologically representative dimensions (scale of an artery / arteriole / capillary) and

geometry (circular lumen), should be biocompatible for endothelialization (i.e. coating the lumen with endothelial cells) and optically clear for experimental observation, and should be fabricated quickly and easily.

The model should also provide a reproducible in vitro environment for controlled experimentation where certain experimental variables can be kept constant, which is difficult to achieve with in vivo methods such as intravital imaging of microvessels in live animals. Outside of biomedical research, experimental work in microfluidics will also benefit from using a microchannel with circular lumen because experimental results can be compared meaningfully with theoretical or computational work that utilizes assumptions of circular cross sections.

1.6 Organization of Thesis

Chapters 2 and 3 present work on the bubble evolution in a rigid tube at physiological temperature and room temperature respectively.

Chapter 4 discusses the design of a benchtop model of a microvessel.

Chapter 5 summarizes all preceding discussions and their conclusions.

At the end of each chapter will be a list of bibliography relevant to that chapter, followed by all the figures and tables of that chapter.

Supporting information deemed lengthy for inclusion in any chapter is assigned to the Appendices.

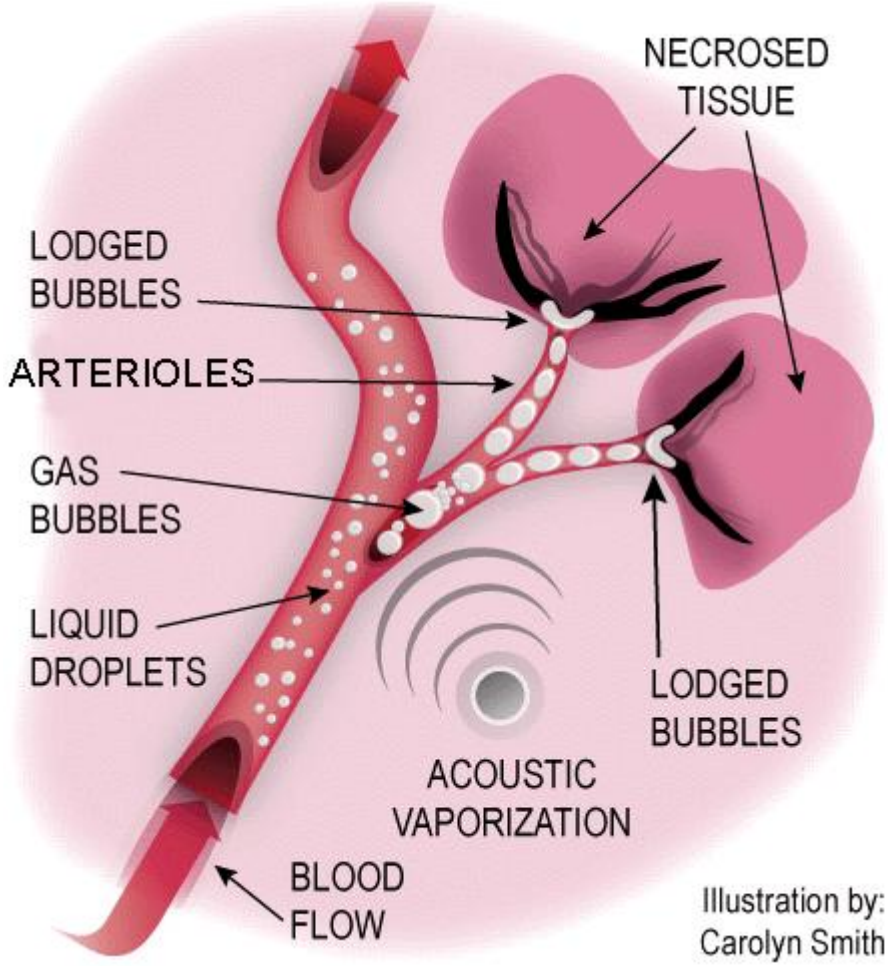

Figure 1.1: An illustration of how gas embolotherapy is envisioned to work.

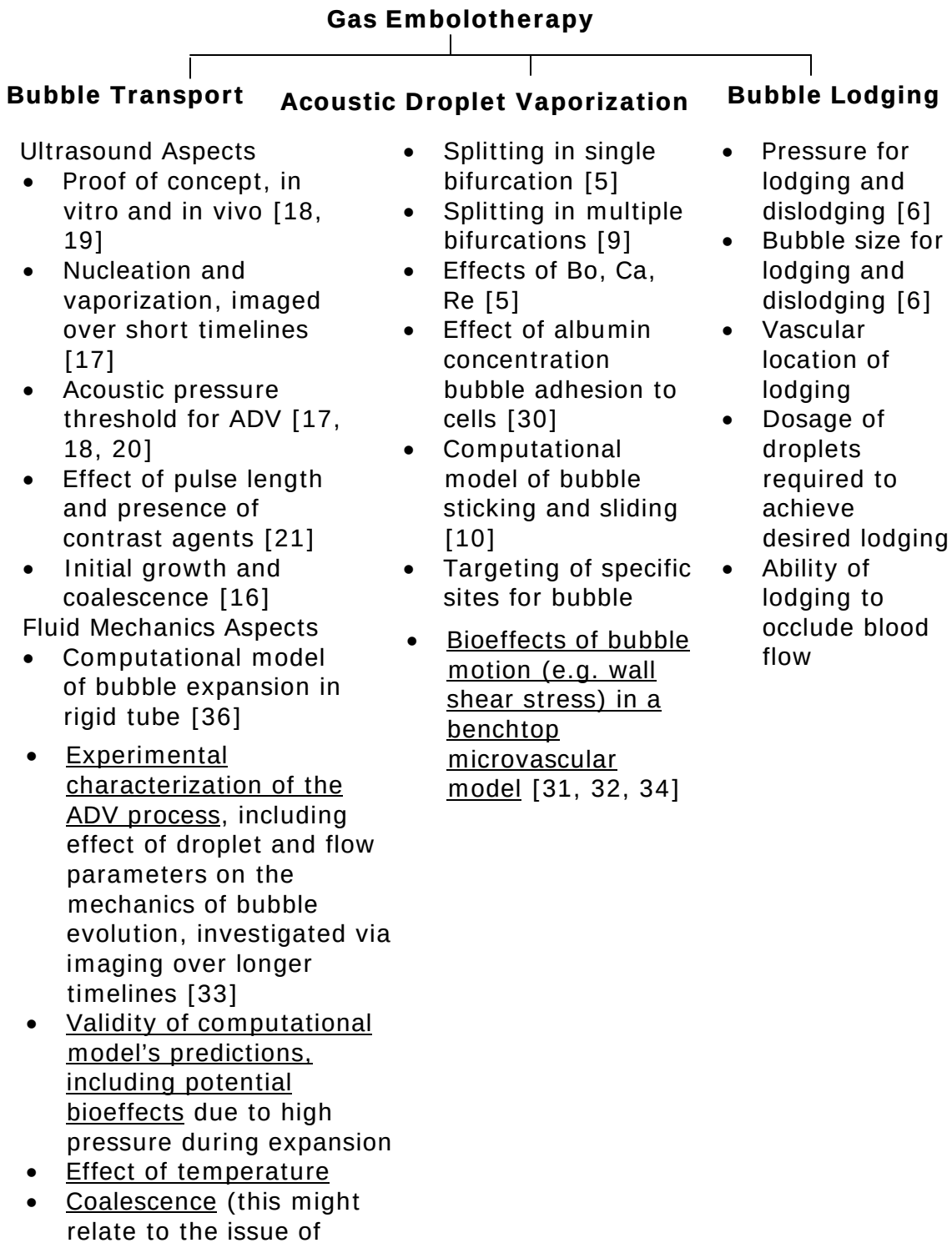

Figure 1.2: Research roadmap for gas embolotherapy. (the underlined points fall completely or partially under the scope of work in this thesis)

References

1. Apfel, R.E. and J.P. Harbison, *Acoustically Induced Explosions Of Superheated Droplets.* Journal Of The Acoustical Society Of America, 1975. **57**(6): p. 1371-1373.

2. Avedisian, C.T., *Bubble Growth in Superheated Liquid Droplets*. Encyclopedia of Fluid Mechanics. Vol. 3. 1986: Gulf Publishing Co., Houston, TX.

3. Brujan, E.A., et al., *Dynamics of laser-induced cavitation bubbles near elastic boundaries: influence of the elastic modulus.* Journal Of Fluid Mechanics, 2001. **433**: p. 283-314.

4. Bull, J.L., *Cardiovascular Bubble Dynamics.* Crit Rev Biomed Eng, 2005. **33**: p. 299-346.

5. Calderon, A.J., J.B. Fowlkes, and J.L. Bull, *Bubble splitting in bifurcating tubes: a model study of cardiovascular gas emboli transport.* J Appl Physiol, 2005. **99**: p. 479-487.

6. Calderon, A.J., et al., *Microfluidic model of bubble lodging in microvessel bifurcations.* Applied Physics Letters, 2006. **89**(24).

7. Di Segni, R., et al., *Embolotherapy: agents, equipment, and techniques.*, in *Interventional radiology*, W.R. Castaneda-Zuniga, Editor. 1997, Williams and Wilkins: Baltimore. p. 81-84.

8. Dietrich, N., et al., *Passage of a bubble through a liquid-liquid interface.* Aiche Journal, 2008. **54**(3): p. 594-600.

9. Eshpuniyani, B., J.B. Fowlkes, and J.L. Bull, *A bench top experimental model of bubble transport in multiple arteriole bifurcations.* International Journal Of Heat And Fluid Flow, 2005. **26**(6): p. 865-872.

10. Eshpuniyani, B., J.B. Fowlkes, and J.L. Bull, *A boundary element model of microbubble sticking and sliding in the microcirculation.* International Journal Of Heat And Mass Transfer, 2008. **51**(23-24): p. 5700-5711.

11. Fezzaa, K. and Y.J. Wang, *Ultrafast X-ray phase-contrast imaging of the initial coalescence phase of two water droplets.* Physical Review Letters, 2008. **100**(10).

12. Freude, B., et al., *Apoptosis is initiated by myocardial ischemia and executed during reperfusion.* J. Mol. Cell. Cardiol., 2000. **32**: p. 197-208.

13. Frost, D.L., *Dynamics Of Explosive Boiling Of A Droplet.* Physics Of Fluids, 1988. **31**(9): p. 2554-2562.

14. Frost, D.L., *Initiation Of Explosive Boiling Of A Droplet With A Shock-Wave.* Experiments In Fluids, 1989. **8**(3-4): p. 121-128.

15. Fu, B.R. and C. Pan, *Bubble growth with chemical reactions in microchannels.* International Journal of Heat and Mass Transfer, 2009. **52**(3-4): p. 767.

16. Haworth, K.J. and O.D. Kripfgans. *Initial growth and coalescence of acoustically vaporized perfluorocarbon microdroplets*. in *Ultrasonics Symposium, 2008. IUS 2008. IEEE*. 2008.

17. Kripfgans, O.D., et al., *On the acoustic vaporization of micrometer-sized droplets.* Journal Of The Acoustical Society Of America, 2004. **116**(1): p. 272-281.

18. Kripfgans, O.D., et al., *Acoustic droplet vaporization for therapeutic and diagnostic applications.* Ultrasound In Medicine And Biology, 2000. **26**(7): p. 1177-1189.

19. Kripfgans, O.D., et al., *Acoustic droplet vaporization for temporal and spatial control of tissue occlusion: A kidney study.* Ieee Transactions On Ultrasonics Ferroelectrics And Frequency Control, 2005. **52**(7): p. 1101-1110.

20. Lo, A.H., et al., *The Effect of Pulse Length on Acoustic Droplet Vaporization.* 2006 Ieee Ultrasonics Symposium, Vols 1-5, Proceedings, 2006: p. 285-288.

21. Lo, A.H., et al., *Acoustic droplet vaporization threshold: Effects of pulse duration and contrast agent.* Ieee Transactions On Ultrasonics Ferroelectrics And Frequency Control, 2007. **54**(5): p. 933-946.

22. Nakagawa, N. and W.R. Castaneda-Zuniga, *Transcatheter chemoembolization for hepatocellular carcinoma and other promising transarterial therapies*, in *Interventional radiology*, W.R. Castaneda-Zuniga, Editor. 1997, Williams and Wilkins: Baltimore.

23. Nguyen, V.T., R.M. Furzeland, and M.J.M. Ijpelaar, *Rapid Evaporation At The Superheat Limit.* International Journal Of Heat And Mass Transfer, 1988. **31**(8): p. 1687-1700.

24. Ory, E., et al., *Growth and collapse of a vapor bubble in a narrow tube.* Physics Of Fluids, 2000. **12**(6): p. 1268-1277.

25. Park, H.C., K.T. Byun, and H.Y. Kwak, *Explosive boiling of liquid droplets at their superheat limits.* Chemical Engineering Science, 2005. **60**(7): p. 1809-1821.

26. Robinson, A.J. and R.L. Judd, *The dynamics of spherical bubble growth.* International Journal Of Heat And Mass Transfer, 2004. **47**(23): p. 5101-5113.

27. Shepherd, J.E. and B. Sturtevant, *Rapid Evaporation At The Superheat Limit.* Journal Of Fluid Mechanics, 1982. **121**(AUG): p. 379-402.

28. Shintaku, H., S. Imamura, and S. Kawano, *Microbubble formations in MEMS-fabricated rectangular channels: A high-speed observation.* Experimental Thermal And Fluid Science, 2008. **32**(5): p. 1132-1140.

29. Shusser, M. and D. Weihs, *Explosive boiling of a liquid droplet.* International Journal Of Multiphase Flow, 1999. **25**(8): p. 1561-1573.

30. Stephen, J.H. and J.L. Bull, *Effect of albumin concentration on adhesion of perfluorocarbon gas bubbles for gas embolotherapy.* Faseb Journal, 2005. **19**(4): p. A728-A729.

31. Wong, Z.Z. and J.L. Bull, *An endothelialized, microfluidic model of a microvessel for in vitro research in gas embolotherapy.* Faseb Journal, 2005. **19**(4): p. A728-A728.

32. Wong, Z.Z., J.B. Fowlkes, and J.L. Bull, *A study of cell damage caused by bubble motion in a circular-lumen endothelialized model of a microvessel.* FASEB J., 2008. **22**(1_MeetingAbstracts): p. 1220.5-.

33. Wong, Z.Z., et al. *Microbubble Evolution due to Acoustic Droplet Vaporization: Observation via Ultra-High Speed Imaging*. in *American Physical Society, 61st Annual Meeting of the APS Division of Fluid Dynamics*. 2008.

34. Wong, Z.Z., J. Stephen, and J. Bull, *Effect of Bubbles on Cell Viability in a Circular-Lumen Endothelialized Microvascular Model.* ASAIO Journal, July/August 2006. **52**(4).

35. Ye, T. and J.L. Bull, *Direct numerical simulations of micro-bubble expansion in gas embolotherapy.* J Biomech Eng-T ASME, 2004. **126**(6): p. 745-759.

36. Ye, T. and J.L. Bull, *Direct numerical simulations of micro-bubble expansion in gas embolotherapy.* Journal Of Biomechanical Engineering-Transactions Of The Asme, 2004. **126**(6): p. 745-759.

37. Ye, T. and J.L. Bull, *Microbubble expansion in a flexible tube.* Journal Of Biomechanical Engineering-Transactions Of The Asme, 2006. **128**(4): p. 554-563.

38. Yuan, H., H.N. Oguz, and A. Prosperetti, *Growth and collapse of a vapor bubble in a small tube.* International Journal Of Heat And Mass Transfer, 1999. **42**(19): p. 3643-3657.

Chapter 2

Bubble Evolution in a Rigid Tube at Physiological Temperature

2.1 Synopsis

This chapter focuses on bubble evolution during experiments of ADV in a rigid tube under physiological temperature conditions.

A fluid that exists in the liquid form above its boiling temperature is said to be **superheated**. The liquid is in a metastable state in the thermodynamic sense and can be nucleated to form vapor by homogeneous nucleation or by the presence of heterogeneous nucleation sites such as gas pockets, solid impurities, etc [7]. The liquid cannot be superheated up to its critical temperature, and the maximum temperature attainable beyond which it must boil is known as the "superheat limit temperature" of the liquid [2].

In these physiological-temperature experiments, the DDFP liquid (with a boiling point of 29°C) inside the droplet was superheated since the ambient water in the tank was at 37°C. Using the formulae in [6], derived from the spinodal conditions of the van der Waals equation, the theoretical superheat limit of DDFP was calculated to be about 84°C at atmospheric pressure. It

should be noted that, since the theoretical superheat limit assumes "pure" homogeneous nucleation and excludes all possibilities of heterogeneous nucleation, the practical superheat limit of DDFP might differ from 84°C. Based on the data presented in [7], the differences between experimental and theoretical values of the superheat limit for several organic liquids were at most 12%. Therefore, for DDFP, the practical superheat limit can be as low as 73°C. Unless some event triggers nucleation, vaporization will not occur until the droplet's temperature attains the superheat-limit value.

In the case of ADV, ultrasound provides the triggering, but details of the mechanisms of nucleation, the subsequent vaporization and expansion, are still largely unknown. It was hypothesized in [10] that ADV could be caused by acoustic (inertial) cavitation, while recent work in [8] showed that ADV could be achieved with or without inertial cavitation. Previous ultra-high speed imaging of ADV [9-12] utilized short timelines up to several microseconds, and focused primarily on the acoustics and/or clinical-related aspects of ADV. The present study utilized both short and longer timelines (up to nearly one millisecond) and focused on the aspects of fluid mechanics and bubble dynamics.

Ultra-high speed images of bubble evolution during ADV in a rigid flow tube will be presented. Based on information extracted from processing images from the experiments, an empirical, experimental law for the growth rate during bubble evolution will be proposed. In proposing the experimental law, the question of whether phase change was completed before the bubble

expansion will also be discussed. Comparison with a computational model [19], as well as with a new theoretical model, will be made, and possible reasons for the differences between experimental results and them will be considered.

2.2 Materials and Methods

2.2.1 Droplets Preparation

The droplets used in our experiments were supplied by collaborators from the Basic Radiological Sciences Ultrasound Group at the University of Michigan. The preparation of these droplets [10] was in accordance with the general procedures described below:

- A mixture of 75% (volume) saline-albumin solution of 5 mg/mL concentration and 25% (volume) dodecafluoropentane (DDFP, C_5F_{12}, CAS #678-26-2) was sealed in a 3 mL auto sampler glass vial.
- The mixture was shaken for 30 s at 5000 cpm in a mixer (Wig-L-Bug, Crescent Dental Mfg. Co., Elgin, IL, USA), resulting in a droplet emulsion containing about 9.5×10^9 droplets per mL.
- The droplet emulsions were stored in a refrigerator at 4°C.

2.2.2 Acoustics Setup

A single acoustic pulse was produced by an immersion ultrasound transducer (3.5MHz, single-element, 0.75” element diameter, 1.5” focal distance, A381S, Panametrics-NDT, Olympus, Waltham, MA, USA). The transducer had been calibrated (refer to Appendix A for the calibration data) by a fiber optic probe hydrophone developed by the Basic Radiological Sciences Ultrasound Group at the University of Michigan [13, 14]. The pre-amplified tone burst signal was produced by using two function generators (HP33120A and HP3314A, Agilent Technologies, Santa Clara, CA, USA), where one function generator provided the waveform and the other function generator gated it. This tone burst was amplified by a RF pulse amplifier (GA-2500A, Ritec, Warwick, RI, USA), after which the amplified signal was transmitted to the ultrasound transducer.

The ultrasound transducer was micro-positioned with its focus at the center of the flow tube diameter, by first using a physical aluminium pointer with a tip length of 1.5” and then confirmed by maximizing a pulse-echo via a pulser receiver (5900PR model, Panametrics-NDT, Olympus, Waltham, MA, USA). The transducer was immersed fully in water and orientated below the flow tube at an angle such that the ultrasound approached with a clear path. Monitoring of signals was done on a digital oscilloscope (9310L, Lecroy Corp., Chestnut Ridge, NY, USA).

2.2.3 Flow Tube Selection

Ideally, the flow tube should mimic physiological parameters as closely as possible. These include: a circular lumen; an inner diameter similar to that of a large first-order arteriole, i.e. about 150 μm [5] ; and elastic properties similar to those of native microvessels. At the same time, the acoustic attenuation and impedance mismatch of the flow tube should be low enough to allow ADV, and it should have a high degree of optical transparency for optimal imaging. The following candidates for the flow tube were tried with no success:

(i) Polydimethylsiloxane (PDMS) microchannel, fabricated as described in Chapter 4. PDMS has an acoustic attenuation coefficient of 3.5 dB cm^{-1} MHz-1 and a sound velocity of 1020 ms^{-1} [15]. The acoustic attenuation was reduced by making the PDMS material in the microchannel wall as thin as about 2 mm. However, ADV was still not achieved in the PDMS microchannel --- probably the combination of a reduced but finite acoustic attenuation and the high impedance mismatch of 30% between water and PDMS prevented the droplets from being vaporized.

(ii) Polyethylene (PE) tubing of 400 μm inner diameter, stretched manually down to an inner diameter of approximately 200 μm. Although the stretched PE tubing was acoustically suitable, the stretched portion had a flattened lumen that was non-circular. Furthermore, the varying inner diameter along the stretched portion could contribute potentially additional experimental error.

(iii) Polyurethane (PU) tubing (SAI Infusion Technologies) of 127 μm inner diameter and 63.5 μm wall thickness. As for the case in (i), the PU tubing posed attenuation and/or impedance mismatch issues, and prevented the droplets from being vaporized.

Polyacrylamide gel was another possible choice for the flow tube but it was not fully transparent and there was concern about its material collapsing into the small lumen after prolonged usage [1], which could introduce potentially additional experimental error.

A micro-dialysis bundle of 20 hollow fibers made from biologically inert regenerated cellulose (Spectra/Por, Spectrum Labs, Rancho Dominguez, CA, USA) provided the best candidate for the flow tube, where only one of the 20 hollow fibers was used as the flow tube of interest. Its advantages included excellent optical and acoustical transmission, an inner diameter of 200 μm for each hollow fiber, Luer-lock ports at both ends of fibers to facilitate flow infusion, and relatively easy swapping of other hollow fibers for replacement of a broken fiber. In addition, the presence of other hollow fibers made it less likely for droplets to clog up and cause blockage in the hollow fiber of interest.

Figures 2.1a and 2.1b show a photo of the flow tube setup in a water tank containing de-ionized water and an illustrated plan view of the setup respectively. A single hollow fiber was separated gently from the other 19 fibers and secured by tape onto the U-shaped holder. This fiber of interest was moved into the field of view of the microscope by using the micro-positioners. The other 19 fibers were also taped down to prevent them from floating around. One Luer-lock port of the fiber bundle was connected via a

microbore tubing to a T-connector which in turn connected the infusion syringes for deionized water and droplets respectively, and the other Luer-lock port of the fiber bundle opened into the water tank. Microbore tubings were used for all connections in the flow system.

Since the droplets in our ADV experiments would be stationary initially in non-moving water, the presence of the other 19 hollow fibers did not affect any boundary or initial conditions in the flow tube of interest. The inlet and outlet Luer-lock ports of the fiber bundle were approximately level, so there was no pressure gradient due to difference in water heads. Care was taken to keep the fiber bundle immersed and wet at all times, because drying out of the fibers would result in breakage and leakage.

2.2.4 Ultra-High Speed Imaging

An ultra-high speed framing camera (SIM802 Model, Specialised Imaging Ltd, Hertfordshire, UK) with eight discrete intensified optical channels was used to give sixteen (1360 horizontal x 1024 vertical pixels) 12-bit images. The camera allowed exposures ranging from 5 nanoseconds to 10 milliseconds and inter-frame times between 0 nanoseconds and 10 milliseconds. Attached to the camera port was a tandem combination of two Nikkor camera lenses (Nikon, Melville, NY, USA), a 50-mm f/1.4D lens and a 70-300-mm f/4-5.6D zoom lens, which gave a magnification between 1.4x and 6x. (Figures 2.2a and 2.2b)

An industrial microscope (Eclipse infinity series system with a modular focus mount, Nikon, Melville, NY, USA) with 10x or 20x water immersion objectives (Nikon, Melville, NY, USA), was used together with the above-mentioned camera lenses setup, to achieve the final desired magnification. The maximum cumulative magnification utilized for the experimental work described herein was 60x, which corresponded to a resolution of **6.5 pixels per micron** for the full frame images (note: the scale was determined by calibrating an image with a microscope calibration slide). Using an industrial microscope provided more space on the benchtop for the water tank, transducer and flow tube, because it enabled the light path to go up through the microscope objectives and camera lenses into the ultra-high speed framing camera and streak camera, which were both mounted on a vertical base plate. The base plate could be moved up or down by rotating a turn wheel, which was useful for rough focusing of the ultra-high speed camera. The transducer and flow tube were each controlled by a set of 3-axis micro-positioners, which enabled critical fine-tuning of positioning as well as focusing for the imaging. In addition, the microscope's own focusing knob was also used for fine focusing of the image.

Streak images, at a temporal resolution of 5 picoseconds and spatial resolution of 1392 horizontal x 1024 vertical pixels, were provided by a streak camera (Optoscope SC-10 System, Optronis GmbH, Kehl, Germany) connected to the framing camera.

For initial positioning of the droplet of interest and general viewing via the microscope eyepiece or camera monitor screen, illumination was

provided by a fiber-optic illumination system (Fiber-Lite DC-950, Dolan-Jenner Industries, Boxborough, MA, USA). For the ultra-high speed imaging, illumination was provided by a high-power 300 Joules, 13 microseconds flash lamp (Adaptec AD300, Adapt Electronics, Essex, UK) or a 500 Joules, 2 milliseconds flash lamp (Adaptec AD500, Adapt Electronics, Essex, UK). A 50x microscope objective was sealed in a waterproof acrylic cover and placed within a white enclosure (see Figures 2.1a and 2.2a). This 50x objective focused the light from the fiber optic upwards into a cone. The flow tube was positioned at the tip of the cone so as to reap the maximum light intensity for the imaging. The waterproof enclosure was attached to the microscope body by two stainless steel rods but minor adjustments of the position of the 50x microscope objective itself within the enclosure was possible by loosening or tightening a bolt.

2.2.5 Temperature Control

At the start of each experimental session, the water tank was filled partially with deionized water from the tap. A conical flask of deionized water was heated on a heating plate with a magnetic stirrer, and the hot water was added to the partially filled tank. The temperature of the water in the immediate vicinity of the site of ADV (easily judged by the bright cone of light emanating upwards onto the flow tube from the 50x focusing objective) was measured with a quick-read digital thermometer (Model 9840N, Taylor, Oak Brook, IL, USA). A household coffee-mug immersion heater (Model

CH101, 120V/125W, Chun Tai Electric Co., Taipei, Taiwan R.O.C.) was immersed in the water tank by attaching its power cable on a retort stand, and switching this immersion heater on/off provided a means to maintain the temperature of the water in the desired range of 95°F (35°C) and 101°F (38°C). The normal human physiological temperature is about 98.6°F (37°C).

2.3 Experiments

2.3.1 Experimental Procedures

The general procedures for setting up each imaging experiment were as follows:

- A small volume (less than 0.1 mL) of the droplet emulsion was injected into one port of the T-connector, after which the port was closed, and the other inlet port was opened to inject water to dilute the droplet emulsion. Subsequent gentle pressing of the water syringe was sufficient to transport the droplets into the hollow fiber. A few practices were usually required to get the desired inter-droplet spacing.
- An individual droplet was positioned, as closely as possible, at the cross-hairs of the SIM framing camera onboard screen. Figure 2.3 shows the initial droplet size distribution for the physiological-temperature experiments. While searching for target droplets for ADV, the bigger droplets were chosen for better imaging as well as possible investigation of contact (if any) of the expanding bubble with the walls. In addition, the

droplets came from an Ostwald-ripened batch prepared almost one year before the date of the experiments. Therefore, it was not surprising that the droplets in these experiments were between 15 and 40 microns in initial diameter.

- It was critical to position correctly the respective trigger signals on the timeline in the SIM camera software, so that the entire imaging event was well-coordinated. The light and ultrasound needed to arrive at the appropriate times, and the framing camera and streak camera also needed to execute the image capture at the right moment. An example of a typical timeline is shown in Figure 2.4. For each imaging event, a TIFF-format image showing 16 frames and a IMG-format file showing the streak image were generated. The timings of the image frames could be evenly distributed or staggered. For example, if the initial twenty microseconds of a 500-microseconds event were of greatest interest, a greater number of frames, say 12, could be assigned to the first ten microseconds, while the remaining 4 frames could be used for the ensuing 480 microseconds. The complete list of timelines used for the physiological-temperature experiments is shown in Table 2A.
- Before actually imaging the ADV process, the quality of the images was optimized by taking several test images while adjusting the charged-couple-device (CCD) gain (note: nominal gain of 1 through 8 could be set via the software), and/or adjusting the exposure and interframe times. In general, as a rule of thumb, longer exposure times or higher CCD gain

resulted in brighter images while shorter exposure and interframe times resulted in sharper images.

- Before and after each imaging event, the temperature of the water in the immediate vicinity of the site of ADV was measured.
- Nearly 100 experiments were run at physiological temperature, of which a total of 64 image sets of good quality were captured for experiments with peak negative acoustic pressures of 4.7 to 10.8 MPa and 3 to 17 cycles in the acoustic pulse. (see Table 2B) For completeness of experimental information, Tables 2C and 2D are included.

2.3.2 Processing of Images

A key parameter of study was the radius of the droplet and expanding bubble. In consideration of the difficulty in determining objectively the radius of non-spherical bubble profiles with jagged boundaries, an **effective radius** of a spherical bubble was calculated from the measured area of the droplet/bubble (based on the methodology reported in [16]). In this thesis, many discussions regarding "radius" refer to this "effective radius".

The measurement of areas was made in ImageJ, a public-domain, Java-based image processing program developed at the National Institutes of Health (NIH). Outlined below are the processing steps applied to the images :

- Knowing the number of pixels per mm of the image (Section 2.2.4), the scale of the image was keyed into the program.
- The image of the droplet/bubble in Frame 1 was cropped.

- The image was converted to a 8-bit binary format and its threshold was auto-adjusted.
- The program's "Analyze Particles" function was called, and by excluding pixel group sizes below a certain number (say, 200), the droplet/bubble was identified with its outline displayed.
- The area within the outlined droplet/bubble was measured and displayed in accordance to the scale set earlier.
- The above steps were applied to Frame 2, 3, and so on, until Frame 16, thereby completing the processing for one experimental set.

A macro was written in ImageJ to automate most of the above-mentioned steps. However, the macro would fail occasionally to identify the correct object outline (due to poor brightness or contrast of the original image), and it would be necessary to do the thresholding and outlining manually. If part of the expanding bubble was outside the frame window, its area could be measured by superimposing a circular or elliptical profile in ImageJ which would display the area of the superimposed profile.

2.4 Results and Discussion

2.4.1 Examples of Images

Figures 2.5 and 2.6 show two examples of typical images of the ADV of a droplet in a rigid tube. Figure 2.5 was taken at a higher magnification than Figure 2.6 in which the tube walls were visible. Regardless of the

magnification of the images (i.e. whether they appeared "zoomed-in" without the tube walls being visible or "zoomed-out" with the tube walls visible), the orientation of all images had the the tube walls longitudinally in the north-south direction and the ultrasound pulse approaching the droplet transversely from the left and at an angle out of the plane. The assumption that the tube was rigid was supported by all the images --- there was no wall movement or deformation seen in any of the images.

Qualitatively, judging from the interior color of the droplet/bubble turning from white to black, the example images revealed that the phase change from DDFP liquid into DDFP vapor was completed within the initial microseconds. (more discussion on this in latter sections) After the phase change, the bubble would expand rather rapidly but its shape did not always remain spherical. During the intermediate stage between the phase change and the eventual stable spherical bubble shape, the bubble's boundary would sometimes exhibit protrusions or irregularities and its interior would sometimes exhibit folds and wrinkles. Unfortunately, the bubble's color or intensity could not provide quantitative information, because they were affected by the reflection and refraction of light at the boundary [3], as well as any optical interference from violent movement of the liquid/vapor within the boundary. Collapse of the bubble was rarely observed in the physiological-temperature experiments. (more discussion in later sections)

2.4.2 Expansion Ratio

Given that the ultra-high speed camera could yield only 16 full frames in a single shot, it was important to have an idea of when the bubble evolution started to be asymptotic, so that more frames could be used for the earlier times. The effective bubble diameters of several experiments were plotted against time, as shown in Figure 2.7. The plots suggested that the bubble size started to approach its maximum value asymptotically sometime between 100 and 150 μs on the timeline. With this information, it was decided that the majority of experiments would use timelines ending at about 300 μs.

A useful indicator of the bubble growth was an expansion ratio, i.e. the bubble diameter normalized by the initial droplet diameter. Figure 2.8 shows the time evolution, for the bubbles in Figure 2.7, re-plotted in terms of expansion ratios.

An approximate value of 125 for the expected volume expansion ratio (i.e. radial expansion ratio of roughly 5) using the ideal gas law, without consideration of surface tension, was estimated in [11]. In our present work, by applying mass conservation principles and using the ideal gas law and the Young-Laplace equation to take into account surface tension, the theoretical expansion ratio was calculated to be **5.27** (see Appendix B). The surface tension of DDFP gas and water was estimated as 70 mN/m, based on the work reported in [18].

The average expansion ratio for all the physiological-temperature experiments was **5.05** (standard deviation of 0.097), i.e. about 4.2% lower than the theoretical value. According to an analytical method using

geometrical optics as reported in [3], the volume of a spherical gas bubble would be underestimated for large values of θ_L (angle of the light source) due to reflected rays. By estimating the dark ring width of the bubble in the final frame of our images, it was determined that θ_L was moderately large (about $\pi/10$) in our setup, and the error of volume underestimation was about 5%. This implied that the error of radius underestimation was about 1.6%. However, this would not be an issue for the expansion ratio as the numerator error cancelled the denominator error.

2.4.3 Effect of Initial Droplet Size on Expansion Ratio

As shown in Figure 2.9, the expansion ratio was independent of the initial droplet size (low correlation coefficient of 0.0091), and it ranged from 4.81 to 5.29.

2.4.4 Effect of Acoustic Pressure and Pulse Cycles on Expansion Ratio

Figure 2.10 suggested that the expansion ratio was independent of the acoustic pressure, since there was no clear upward or downward trend, and there was a lot of overlapping in the error bars based on standard deviations. To confirm this, a statistical T-test was applied to the data (see Appendix C). Except for the T-test between 10.8MPa and 6.1MPa ($p < 0.05$ but > 0.01), the p-scores were all larger than 0.05.

Figures 2.11 and 2.12 suggested that the expansion ratio was independent of the number of cycles in the acoustic pulse. Again, a T-test was applied to the data (Appendix C), and except for one case ($p= 0.047$), the other p-scores were all larger than 0.05.

Based on the plots and p-scores, one could assert that the acoustic pressure and the number of pulse cycles did not affect the expansion ratio. The threshold pressure for ADV depends on frequency [11], and according to the findings of [11], the threshold for a frequency of 3.5MHz would be about 1.4 MPa. Once the threshold pressure to trigger ADV was satisfied, the vaporization proceeded (i.e. an all-or-none event), and the additional acoustic pressure or additional cycles did not further increase the expansion ratio.

2.4.5 Growth Rate and Experimental Law of 4-Stage Growth

The radial growth rate was a key finding in the work on explosive boiling by Shepherd and Sturtevant [16]. A close examination of the evolution curves for our experiments (e.g. Figures 2.13 and 2.14) suggested that the bubble evolution could be described by an empirical, experimental law of 4-stage growth:

- Stage I, from 0 to about 1.5 μs, with expansion ratio reaching about 1.5, and an explosive, linear growth rate

- Stage II, from about 1.5 μs to sometime between 3.5 and 7 μs, with expansion ratio reaching about 2, and a linear but less explosive growth rate
- Stage III, from sometime between 3.5 and 7μs, to sometime between 60 and 200μs, with expansion ratio reaching about 90 to 95% of maximum, and a non-linear growth rate that decreased with time
- Stage IV, beyond 60 to 200 μs, with expansion ratio reaching the maximum, and an asymptotic growth rate

An attempt was made to quantify the growth rate for each stage by curve-fitting the relevant data points. Unfortunately, for Stage I, there were insufficient (only one or two) data points in the early part of the timeline of most experiments.

For Stage II, the radial growth rates for the different experiments showed large variability but they were highly linear (average R^2 = 0.948). The mean Stage II growth rate was determined as **3.56 m/s**, with a standard deviation (S.D.) of 1.16 m/s. For Stage III, a rudimentary curve-fitting of the experimental data suggested a dependence on the square-root of time. For Stage III, by taking the square-root of the timelines and plotting the bubble radius data in Stage III against $t^{0.5}$, the radius R(t) was determined to expand linearly with the square-root of time, with a constant of proportionality of 4.19 (S.D. of 1.57). The correlation coefficient R^2 for this linear dependence on $t^{0.5}$ was 0.949.

Stage II: $R(t) = K_{II} \cdot t$, where K_{II} = 3.56 (with S.D. of 1.16) …… (2-1)

Stage III: $R(t) = K_{III}\sqrt{t}$, where K_{III} = 4.19 (with S.D. of 1.57) …… (2-2)

` The two equations (2-1) and (2-2) were non-dimensionalized. The bubble radius was scaled against the initial droplet radius, a. A pressure time scale $\tau_P = a \cdot \sqrt{\rho / (P_i - P_{out})}$ was used to non-dimensionalize time (with a: initial droplet radius, ρ: DDFP gas density of 12 kg m^{-3}, P_i: initial bubble pressure of 14.86 MPa, P_{out}: atmospheric pressure). Dimensionless radii constants, C, were also added to the non-dimensionalized equations to account for the transitions between Stage I and Stage II, as well as between Stage II and Stage III. The final non-dimensionalized equations, in which the overbars represent dimensionless variables, are:

Stage II: $\overline{R} = 3.21\times10^{-3} \cdot \bar{t} + C_{I-II}$, where $C_{I\text{-}II}$ ~1.5 ……..(2-3)

Stage III: $\overline{R} = \frac{0.126}{\sqrt{a}} \cdot \sqrt{\bar{t}} + C_{II-III}$, where $C_{II\text{-}III}$ ~ 2 ……..(2-4)

Equation (2-3) showed that the growth rate in Stage II was independent of the initial droplet radius. Further evidence of this independence was provided by the plot in Figure 2.15.

Equation (2-4) showed that the growth rate in Stage III was not independent of the initial droplet radius. This inverse relation between the

expanding bubble radius and the square root of the initial droplet radius was reflected in the slopes of the Stage III curves plotted in Figure 2.8.

In Stage IV, the bubble radius approached asymptotically its maximum value (which would be about five times its initial droplet radius).

2.4.6 Qualitative Discussion of the Stages I to IV

The following discussion will attempt to explain or speculate what could have happened physically during each growth stage.

During Stage I, the arrival of the ultrasound caused the droplet boundary to appear grainy and blurred. One possible reason was that vibrations of the droplet and its surrounding water brought the image out of focus. Another possible reason was the formation of capillary waves under the action of the ultrasound. A timescale for the capillary waves was estimated by balancing viscous and surface tension terms, which gave $\tau_{V-ST} = {(2\mu \cdot a)}/{\sigma}$, with μ being viscosity and σ being surface tension. If phase change had not been completed, by using viscosity (0.465 mPa.s) and surface tension (9.5 mN/m) values for DDFP liquid, the timescale was 0.98 μs for a droplet of initial radius 10 μm. If phase change had been completed, by using viscosity (0.02 mPa.s) of air as a proxy and surface tension (70 mN/m) of DDFP gas-water, the timescale was 0.0057 μs. In either scenario, capillary waves would not be present beyond the initial microseconds of ADV. It should be noted that, with an ultrasound wavelength of about 429 μm corresponding to the 3.5MHz frequency, there was no pressure gradient

across the droplet diameter of 15 to 40 μm. Depending on the number of cycles in the acoustic pulse (between 3 and 17), the presence of the ultrasound spanned between 0.86 μs and 4.86 μs. Most of the experiments were conducted with 4 or 7 cycles, which corresponded to times of presence of 1.1 μs and 2 μs respectively.

The ultrasound triggered the vaporization process, as shown by the formation and rapid growth of nucleation site(s) in the droplet's interior (Figure 2.16). Despite the limited resolution of details in the images, the nucleation was observed to begin on the central axis of the droplet, which was consistent with the findings in [10]. During the rarefaction half-cycle of the acoustic pulse, the nucleation could have been brought about by a localized, rapid pressure drop, or if micro-voids were already present in the liquid DDFP (due to impurities), these micro-voids could have expanded into nucleation sites under the action of ultrasound. The recent work in [8] suggested that the nucleus for ADV came from within the droplet.

Stage II growth involved irregular bubble shapes with crinkles, jags and protrusions in their boundaries, as well as interior appearances that were sometimes all black but often a mix of black and grey wrinkled folds. Research on explosive boiling had found that explosive boiling involved a dynamic instability that distorted and roughened the evaporating surface, and the increased surface area increased the heat transfer rate correspondingly. To determine whether some of the mechanisms of explosive boiling might apply to ADV, the key question of: "At what point in

time was the phase change from liquid to gas completed?" needs to be answered.

Depending on the particular model of heat transfer, the evaporation rate could vary with molar mass, saturation temperature and pressure, thermal conductivity, latent heat, etc. Estimates of the time required for complete vaporization, obtained by using models cited in [4, 17], ranged from 18 to 50 microseconds for a 20-micron diameter DDFP droplet. We will proceed with a solely qualitative discussion on this matter.

Guided by the general assumptions of incompressibility of a liquid and compressibility of a gas, if the phase change and subsequent gas expansion were two distinct processes, one would expect to see a bubble remain at the same diameter as its pre-vaporization droplet size before any expansion. In the experimental images recorded, this did not appear to be the case. There were three pieces of evidence from the images that could refute the hypothesis that phase change was completed in the first several microseconds:

(i) As shown in Figures 2.5, 2.13 and 2.14, in the frames immediately after initiation of the vaporization (seen as blurring of the droplet's outline), the bubble was already expanding while vaporization was probably still ongoing (suggested by the evaporating surface marked by wrinkled interior folds).

(ii) As seen in the third row of images in Figure 2.16, the arrival of ultrasound and its subsequent motion through the droplet darkened the droplet interior and left a trail of its motion (it looked as if the

droplet had a wake). But, after the ultrasound pulse had departed the droplet, the fourth frame in this third row of images showed clearly that the nucleation site had now become a vapor embryo with a triangular evaporating surface.

(iii) In Figure 2.18, small "bubbles" could be seen within the interior of the expanding bubble from Frame 8 to perhaps Frame 12 or 14. The presence of these smaller "bubbles" weakened the assertion of a single gaseous phase in the interior.

However, the increase in volume during phase change for some cases was not significant, which implied that the assumption of phase change being completed before expansion was not totally invalid. Figure 2.17 shows the Stage II growth of different bubbles.

The transition between Stages II and III was sometimes marked by a "saddle-point" in the evolution curve (data points 9 and 10 in Figure 2.13, data points 10 and 11 in Figure 2.14) where the bubble radius stayed constant for that short instant in time. During this transition period, the following observations could be made about the corresponding image frames:

- The bubble boundary shed its irregularities such as crinkles, jags and protrusions.
- The bubble shape increased in circularity, such that by the start of Stage III, the bubble was almost spherical.

Throughout Stage III and IV, the bubble remained spherical but grew larger. The Bond numbers, $Bo = \frac{\rho g R^2}{\sigma}$, for both the initial liquid droplet (Bo = 0.686×10^{-3}, assuming the largest droplet radius of 20 microns used in the experiments, and using density and surface tension values for liquid DDFP) and final gas bubble (Bo = 16.8×10^{-6}, assuming expansion ratio of five, and using density and surface tension values for gaseous DDFP) were small, which implied that surface tension dominated gravity and maintained the spherical shape.

If phase change were still taking place in Stages II and III, the quantitative relationships depicted by equations 2-1 to 2-4 would match the established theoretical models [6] of inertia-controlled bubble growth and heat-transfer-controlled bubble growth respectively.

Collapse of the bubble was observed in only 2 of the 64 image sets (Figure 2.20). The collapse started at around 5 μs and lasted for a period of 2.5 to 5 μs. However, the collapse was probably due to external pressure influences from nearby bubbles. For example, the bottom image set in Figure 2.20 showed a nearby expanding bubble that eventually coalesced with the bubble of interest (Frames 13 to 15). Although the top image set did not display neighboring bubbles, their presence and influence could not be ruled out. Judging from our overall experimental data, we postulate that bubble evolution under ambient physiological temperature conditions does not involve collapse.

2.4.7 Comparison with Computational Model

To make a comparison with the computational model of [19], several experimental sets of results for initial droplet diameter of 20 $\pm$1 μm, i.e. matching the computational parameter of d/D = 0.1, were plotted. (Figure 2.19)

The computational model was able to predict the general trend of the expansion ratio increasing with time, with the computational growth rate within the range of experimental values. There were two aspects in which the computational model did not show agreement with the experiments: (i) the maximum expansion ratio attained for the case of initial pressure of 20 bar, and the growth rate for the case of initial pressure of 10 bar ; (ii) the prediction of bubble collapse, which was not ubiquitous in the experimental results.

It was stated in [19] that there was no direct relation between the initial bubble pressure chosen for the computational simulations and a readily measured physical quantity. In fact, it was proposed in [19] that experimental data be used to determine the initial bubble pressure and hence calibrate the simulations. Judging from Figure 2.19, initial pressure values between 10 and 20 bar could be chosen as inputs to re-run the computational model iteratively for a better cross-validation with experimental results.

The lack of a ubiquitous collapse process in the experimental results could perhaps be attributed to two factors :

(i) The computational model assumed a tube length 32 times of the tube diameter whereas the experiments were conducted in a flow tube of length at least 800 times of the tube diameter (note: the hollow fibers were about 16 cm between the two Luer-lock ports). In addition, the boundary conditions assumed by the computational model were significantly different from the experimental conditions. The numerical simulations modeled the blood vessel as an open-ended tube connecting two reservoirs, each with the same constant pressure. The Luer-lock outlet of the hollow fiber opened into the water tank, which could be treated as at atmospheric pressure, because the water level above Luer-lock outlet was negligibly small. (as seen in Figure 2.1a, the water level was just enough to facilitate the optics without risking damage to the water-immersion microscope objective)

As for the Luer-lock inlet of the hollow fiber, the situation was not straightforward. Although the Luer-lock inlet was linked to the T-connector, as described in Section 2.2, and the T-connector was closed during the imaging experiments, the presence of the other 19 fibers connected to the Luer-lock inlet could have allowed water to flow back into them via the Luer-lock port. The Luer-lock inlet port together with the other 19 fibers could also be thought of as a mini-reservoir, but whether this mini-reservoir was at atmospheric pressure was debatable.

(ii) The computational model had assumed that the droplet vaporized completely before it expanded as a gas bubble. Immediately after the phase change, the bubble had an initially high pressure and the same volume as the original droplet. Discussions in Section 2.4.6 casted some doubt on the

validity of this assumption. If phase change were still ongoing during the initial bubble expansion, the experimental expansion ratio might possibly lag the computational value, but it is not straightforward whether the experimental growth rate or computational growth rate should be faster. Pending further experimental investigation, it could be that this assumption of phase change being completed before bubble expansion would only be applicable if the total timeline of interest were relatively long.

The experimental data showed that, excluding the times of chaotic phase change, the bubble remained largely spherical during the expansion. This was different from the computational model, which predicted elongation of the bubble in the longitudinal (x) wall direction more than in the transverse (y) direction (Figure 2.19). The computational model predicted a large overshoot (due to high assumed initial pressure) which was mostly not present in the experiments. As will be presented and discussed in Chapter 3 (Section 3.3.5), there were several observations of the expanding bubble coming into contact with the wall, and in those cases, the bubble shape bore some similarity to that predicted by the computational model, albeit over a short part of the timeline before and after the contact with the wall.

2.4.8 Comparison with Simplified Theoretical Model

A simplified theoretical model of bubble expansion in a tube was derived from a modified Bernoulli equation, as shown in Appendix D. This model differs from the standard Rayleigh-Plesset equation in two aspects: (i)

a term for the head loss due to flow is included, and (ii) the configuration of the bubble being in a finite tube instead of being in an infinite liquid (note: Rayleigh-Plesset assumes radial flow in an infinite domain).

Parameters were changed to produce different solutions:- initial radii of 1, 5, 10 and 20 μm; tube lengths of 16, 30 and 60 cm; the two scenarios of only one tube end being open and both ends being open. The solutions were plotted in Figures 2.21 to 2.23. The theoretical results confirmed that having both tube ends open allowed the bubble to reach its maximum size faster than if one end were sealed, but the maximum size attained was not significantly bigger. The theoretical results also showed that a longer tube slowed down the bubble expansion as well as limited the maximum expansion.

The theoretical model over-predicted the maximum expansion ratio (about 9.4, as opposed to about 5 from the experiments), as shown in Figure 2.24. It under-predicted seemingly the growth rate for the first 30 or so microseconds, but the difference was within the experimental error range. Also, the theoretical model predicted oscillatory behavior with both growth and collapse (Figure 2.25), which was unlike the experimental data. However, the final theoretical solution for the expansion ratio converged at about 5.2, which was close to the average experimental value of 5.05. Therefore, the theoretical model predicted the initial growth rate with acceptable accuracy, overshot to a higher expansion ratio and eventually arrived at a final expansion ratio very similar to the experimental value, but the timeline

required to reach that final expansion ratio was very long, due to the oscillatory behavior in the theoretical solution.

As was the case with the computational model, the maximum expansion predicted by the theoretical solution was likely to be sensitive to the value of initial pressure assumed. In the simplified theoretical model, it was assumed that the mass of DDFP was conserved in the gas bubble after an instantaneous phase change but with no change in the diameter, hence giving a very high initial pressure value in excess of 14 MPa. This assumption relied on the underlying principle of the expansion time scale being slower than the phase change time scale, and was at least partially supported by some of our experiments where the increase in volume during phase change was not very significant.

The experimental results exhibited heavy damping which resulted in the final expansion ratio being attained much faster than predicted by the theoretical model. There were several possible factors in the experimental setup that could have led to the heavy damping:

- As the bubble expanded and approached the wall, the viscous contributions from the high shear stresses near the wall increased, which would then slow the bubble expansion. Referring back to Figure 2.24, as the bubble radius approached 40 to 50 μm (i.e. almost contacting the walls), the theoretical solution would break down because one of its key assumptions was to neglect the flow details near the bubble surface, where in this case the high shear stresses in the fluid gap between the bubble surface and the tube wall could not be ignored.

- The effective tube length in the experiments could have been longer than what was estimated.
- One end of the flow tube was effectively sealed, as discussed earlier.
- Other minor losses at the microbore tubing connections and in the other hollow fibers could also have contributed to the damping.

2.4.9 Comparison of Computational and Theoretical Models

A summary of the key similarities and differences between the computational and theoretical models is shown in Table 2E. Each had its limitations but was able to show reasonable agreement with experimental data in some respects. Further work will be required to improve the models.

2.5 Concluding Remarks

The first experimental efforts to image and investigate bubble evolution in a rigid tube under physiological temperature conditions have uncovered more questions than answers. An experimental law that characterizes the bubble growth in four stages has been proposed and discussed in detail. Both computational and theoretical models have their merits as well as limitations in predicting experimental results.

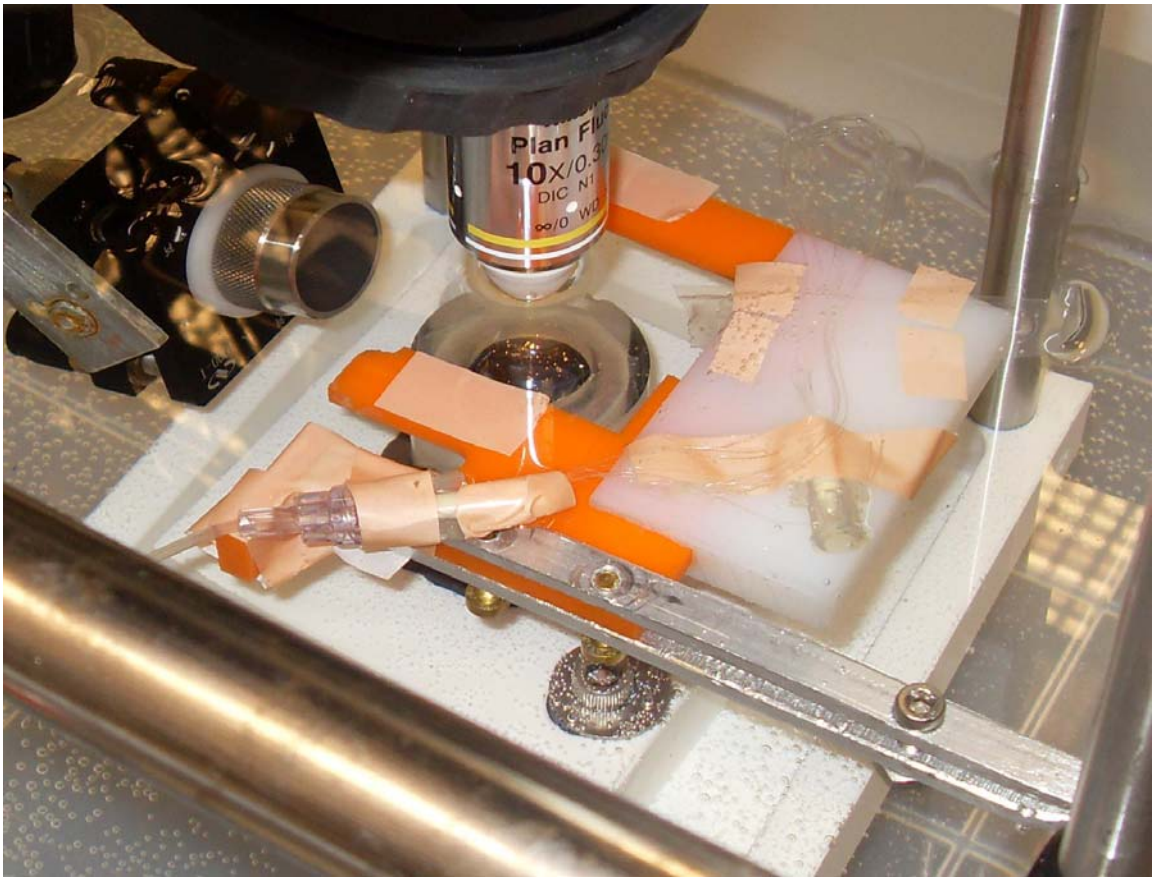

Figure 2.1a: Flow Tube Setup. (note: the hollow fiber of interest is barely discernible; the other 19 hollow fibers were taped onto the U-shape holder to prevent them from floating around in the tank)

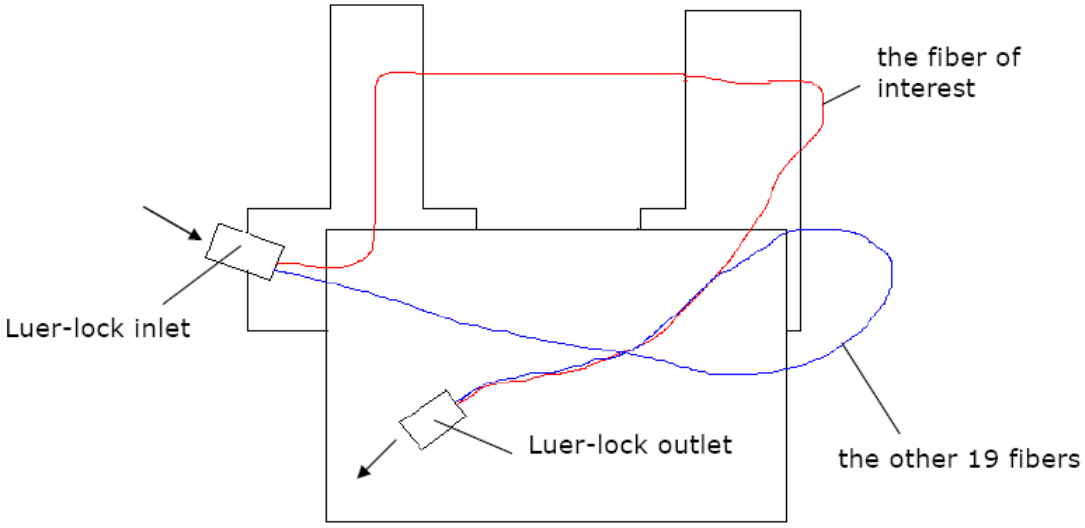

Figure 2.1b: Plan view of the flow tube setup. The fiber bundle was secured on a U-shape holder, with the fiber of interest isolated from the other 19 fibers. (direction of flow as indicated by the arrows next to the Luer-lock ports)

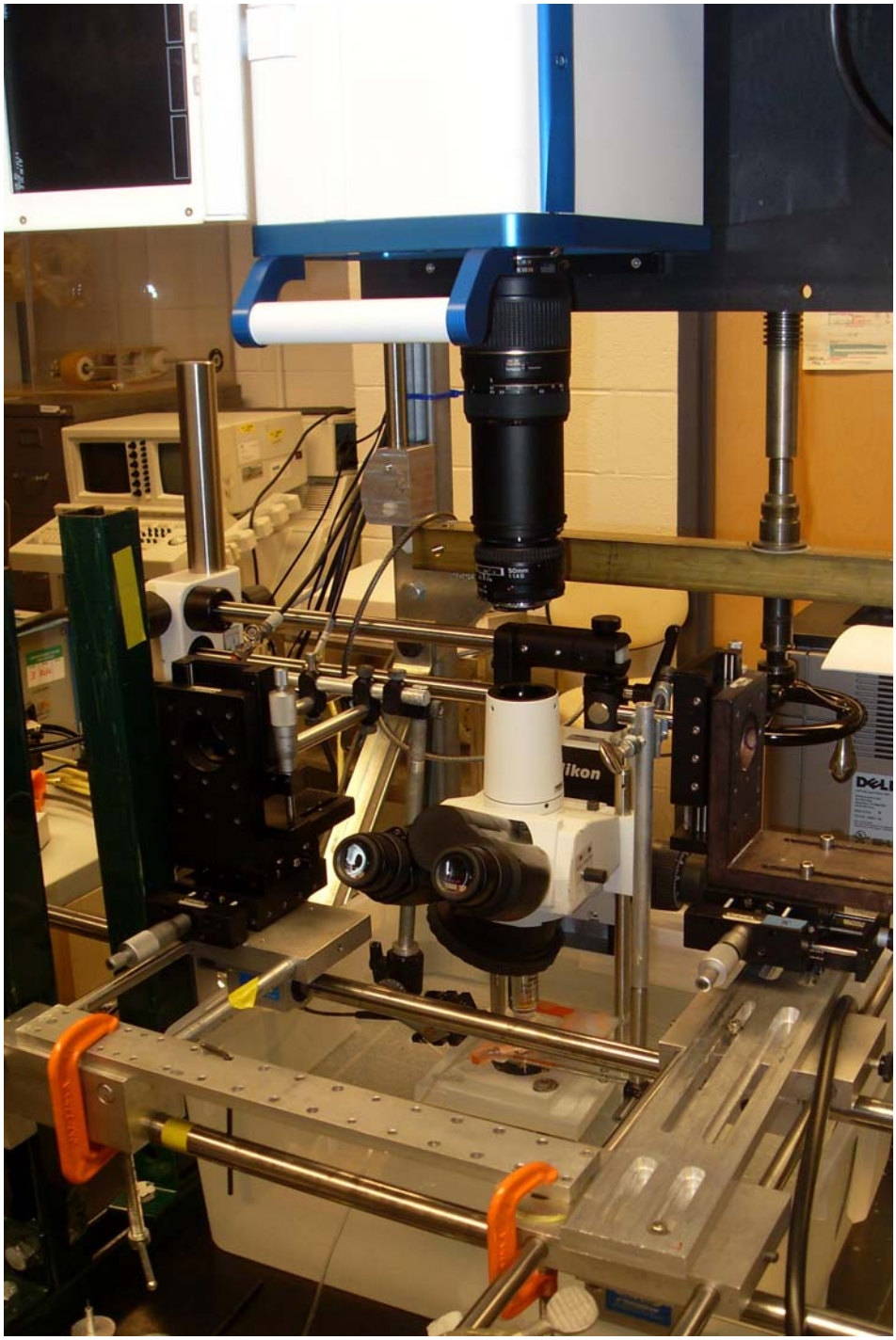

Figure 2.2a: Vertical positioning of the ultra-high speed camera and microscope. The left set of micro-positioners controlled the transducer while the right set controlled the flow tube.

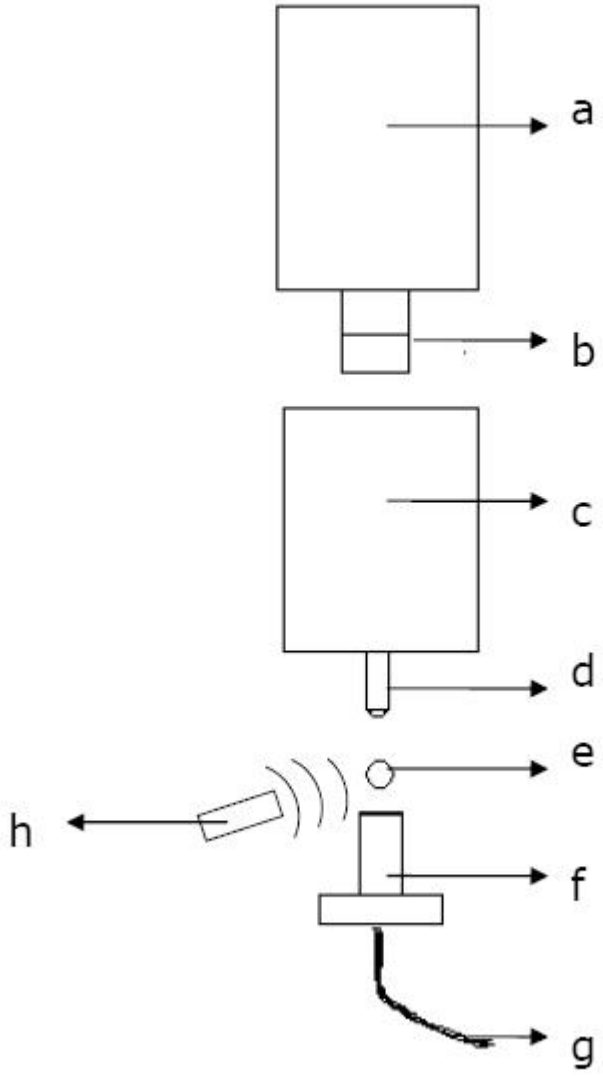

Figure 2.2b: Schematic of the experimental setup shown in the photograph of Figure 2.2a. The equipment are labeled as such: (a) SIM framing camera, (b) combination of two camera lenses, (c) industrial microscope, (d) water immersion objective, (e) flow tube, (f) light-focusing objective, (g) fiber optic cable, and (h) ultrasound transducer. (note: drawing not to scale)

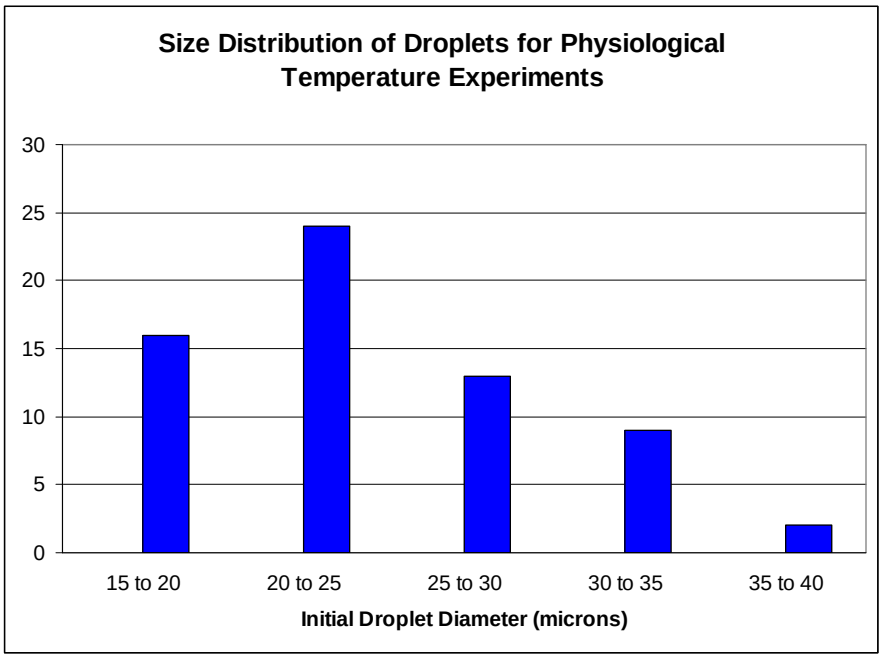

Figure 2.3: Size distribution of droplets for experiments

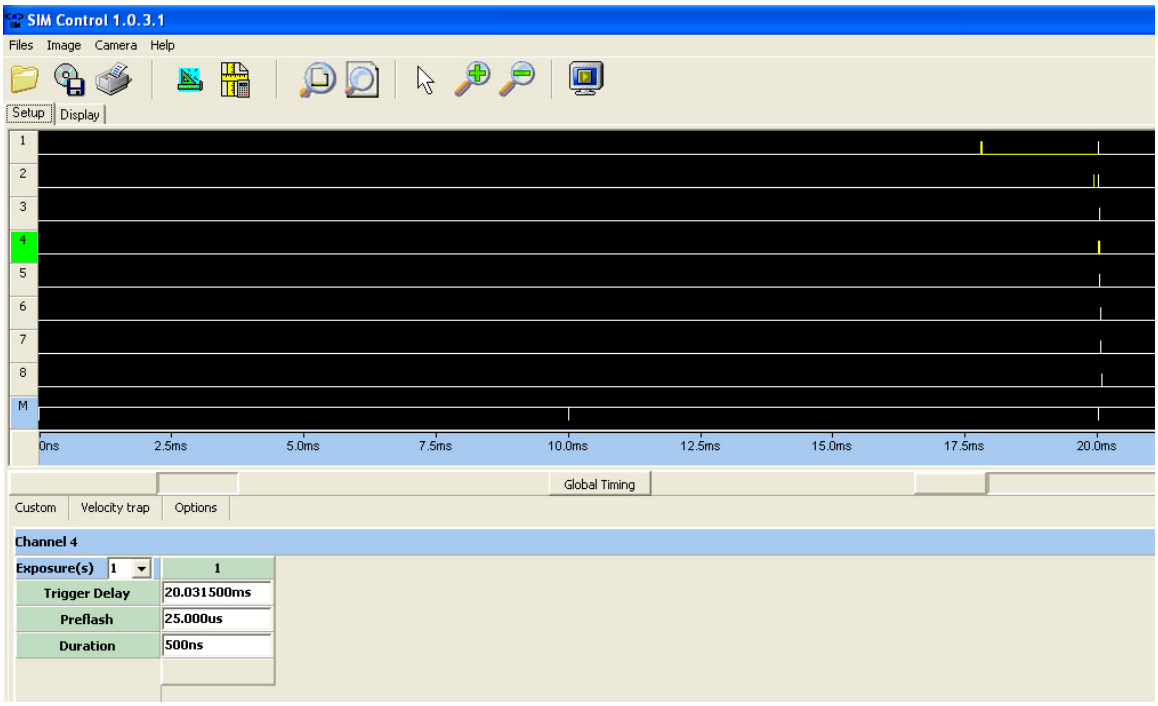

Figure 2.4: Example of a timeline in the SIM camera software. The positions of the different trigger signals, relative to the capture of the first image frame, are respectively : Channel 1, streak camera, -2.2 milliseconds ; Channel 2, flash lamp, -100 microseconds; Channel 4, ultrasound, -25 microseconds (yellow vertical lines on the timeline represent triggers while white vertical lines represent frame images).

Frame	TL1	TL2	TL3	TL4	TL5	TL6	TL7	TL8
1	0	0	0	0	0	0	0	0
2	1.2	0.505	7	0.505	10.5	11	0.5	23
3	2.4	1.01	14	1.01	21	22	1	46
4	3.6	1.515	21	1.515	31.5	33	1.5	69
5	4.8	2.02	28	2.02	42	44	2	92
6	6	2.525	35	2.525	52.5	55	2.5	115
7	7.2	3.03	42	3.03	63	66	3	138
8	8.4	3.535	49	3.535	73.5	77	4	161
9	9.6	4.04	56	7.04	84	88	5	184
10	10.8	4.545	63	12.545	94.5	99	7.5	207
11	12	5.05	70	20.05	105	110	10	230
12	13.2	5.555	77	25.555	115.5	121	15	253
13	14.4	6.06	84	35.06	126	132	30	276
14	15.6	6.565	91	50.565	136.5	143	60	299
15	16.8	7.07	98	87.07	147	154	120	322
16	18	7.575	105	150.575	157.5	165	300	345

Frame	TL9	TL10	TL11	TL12	TL13	TL14	TL15
1	0	0	0	0	0	0	0
2	25	0.5	27	25	0.5	65	80.5
3	30	1	28	26	1	130	161
4	40	1.5	29	27	1.5	195	241.5
5	50	2	29	28	2	260	322
6	75	2.5	30	29	2.5	325	402.5
7	125	3	30	30	3	390	483
8	175	5	31	33	5	455	563.5
9	200	10	32	38	10	520	644
10	225	14	35	50	18	585	724.5
11	250	18	40	70	50	650	805
12	275	30	55	100	80	715	885.5
13	300	50	80	150	100	780	966
14	325	80	130	230	250	845	1046.5
15	350	120	250	430	400	910	1127
16	375	400	600	650	750	975	1207.5

Table 2A: Fifteen different timelines used for physiological temperature experiments. (time units shown are in microseconds)

No. of Cycles	Peak Negative Pressure (M-Pa)				
	4.7	6.1	7.7	9.9	10.8
3				1	4
4			20	4	2
7		6	7	4	1
10	4		2		
14			5		
17	1	3			

Table 2B: Number of successful experiments (total = 64), and their corresponding experimental parameters

Tone Burst Duration (microseconds)	Number of Cycles
0.4	1
0.6	2
0.8	3
1	4
1.5	5
2	7
2.5	9
3	10
4	14
5	17

Table 2C: Number of cycles corresponding to various tone burst durations at 3.5MHz (obtained by counting from the Lecroy oscilloscope screen).

Input to Ritec (mV)	Peak Negative Pressure (M-Pa)
150	3.8
175	4.7
200	6.1
400	7.7
600	9.9
800	10.8

Table 2D: Acoustic pressures used in experiments, with the corresponding input signals into the Ritec pulse-amplifier shown

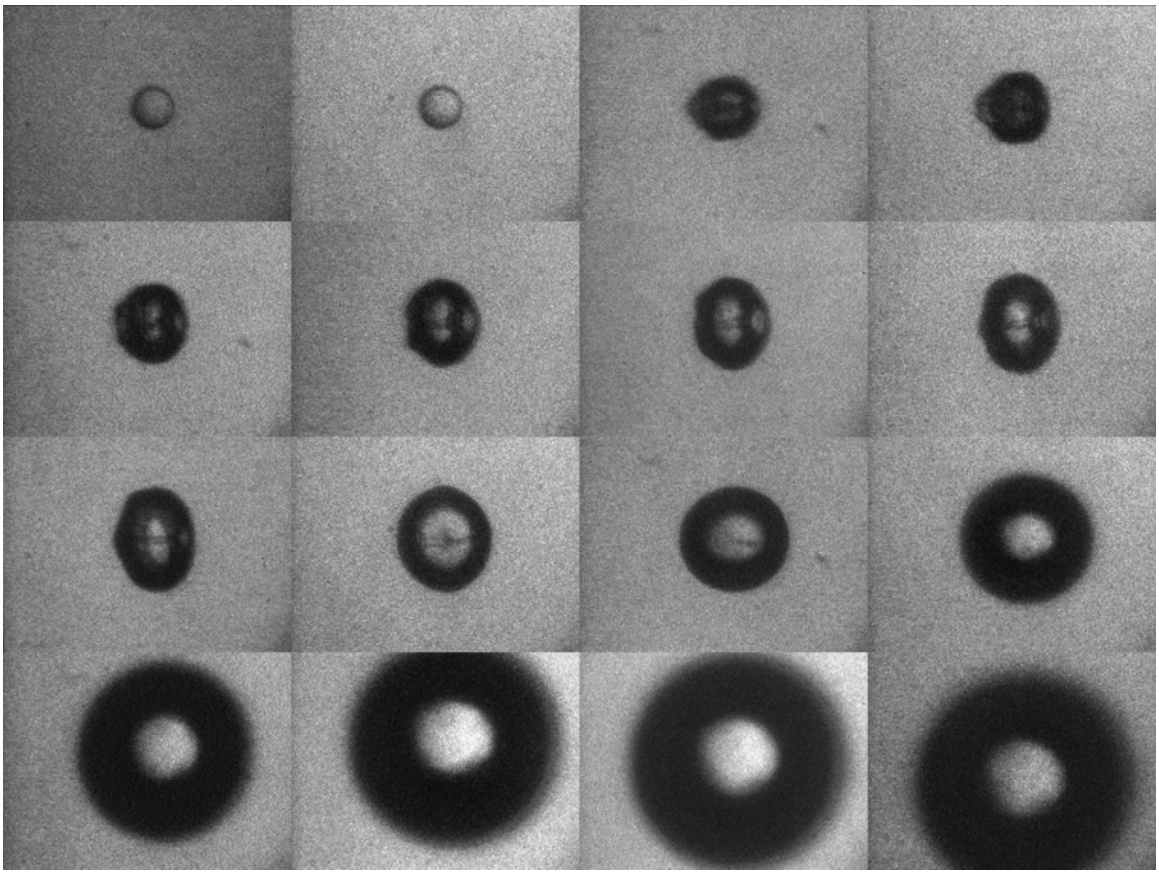

Figure 2.5: ADV of a 33 micron diameter droplet in a rigid tube, with 7.7MPa peak negative pressure and 4 cycles in acoustic pulse.
Timeline of ADV process in microseconds, starting from Frame 2: 0, 1.5, 2, 2.5, 3, 3.5, 4.5, 5.5, 8.5, 13.5, 28.5, 53.5, 103.5, 223.5, 573.5.

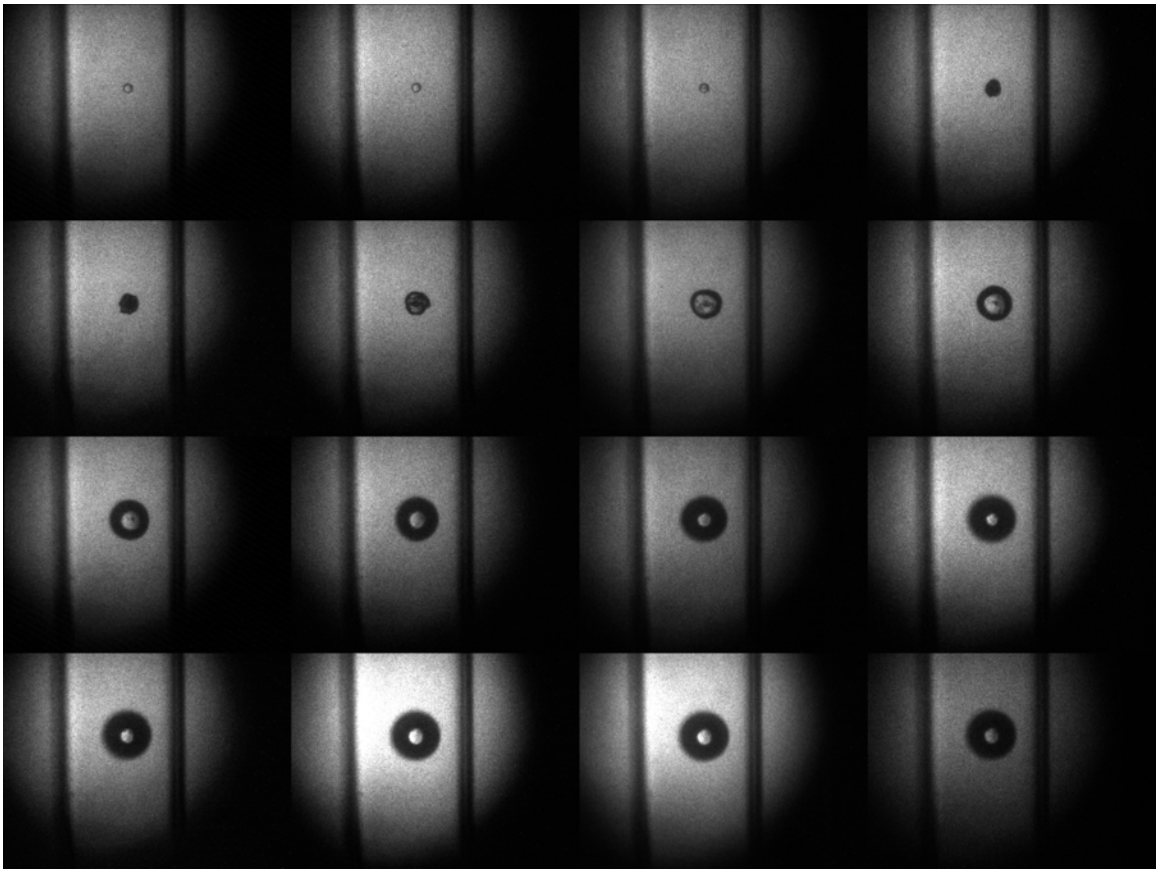

Figure 2.6: ADV of a 20 micron diameter droplet in a rigid tube, with 7.7MPa peak negative pressure and 7 cycles in acoustic pulse. (Magnification lower than that of Figure 2.5)
Timeline of ADV process in microseconds, starting from Frame 2: 0, 0.5, 1.5, 2.5, 4, 7, 11.5, 19.5, 29.5, 49.5, 79.5, 119.5, 249.5, 399.5, 799.5

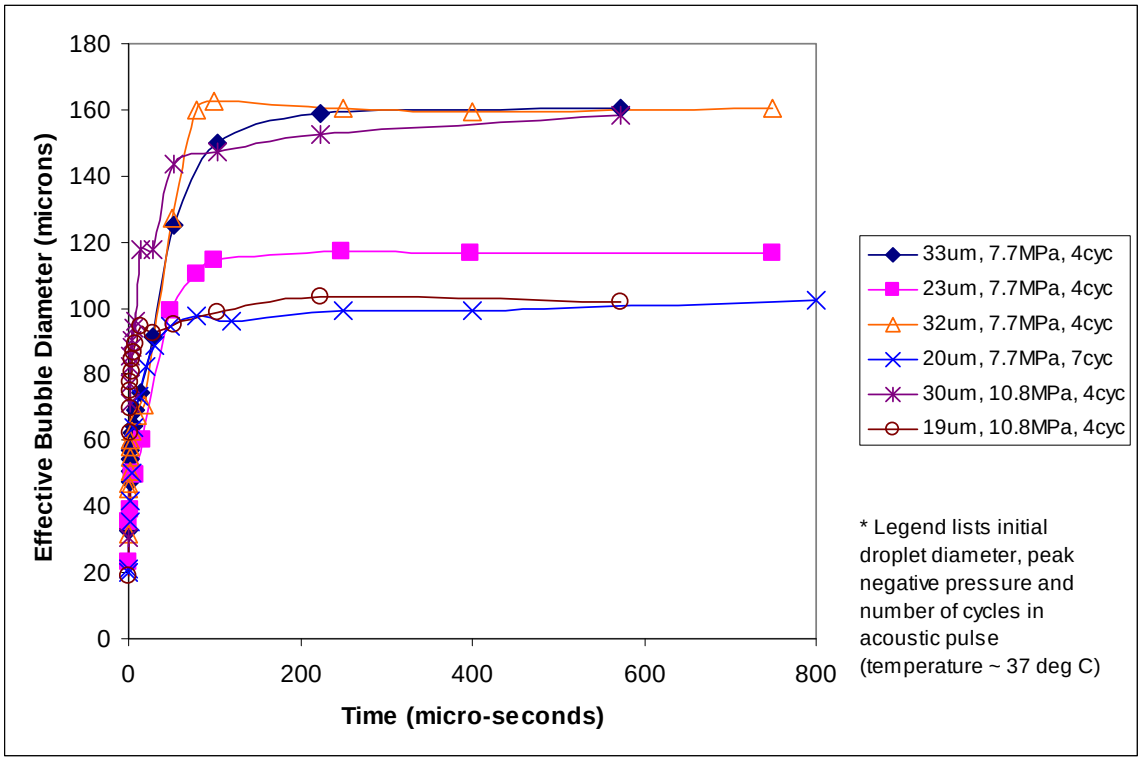

Figure 2.7: Time evolution of effective diameter for various initial droplet sizes and acoustic parameters.

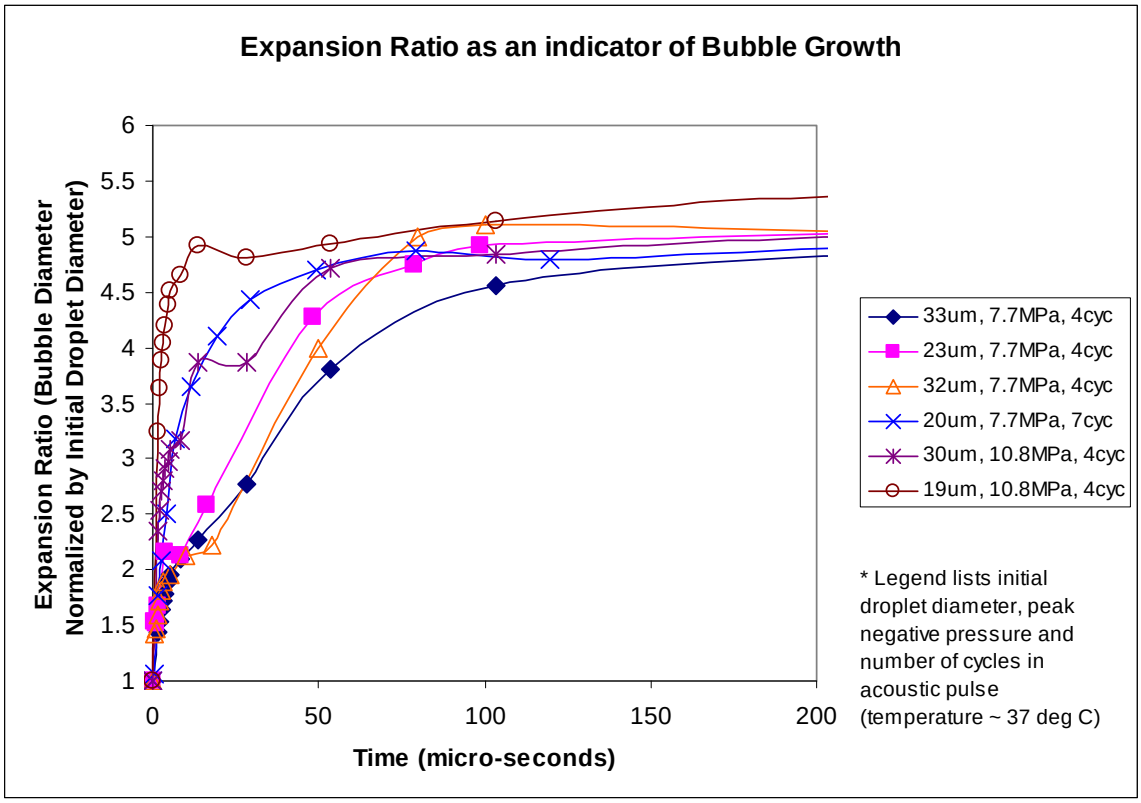

Figure 2.8: Time evolution in terms of expansion ratios. (note the zoomed-in timeline)

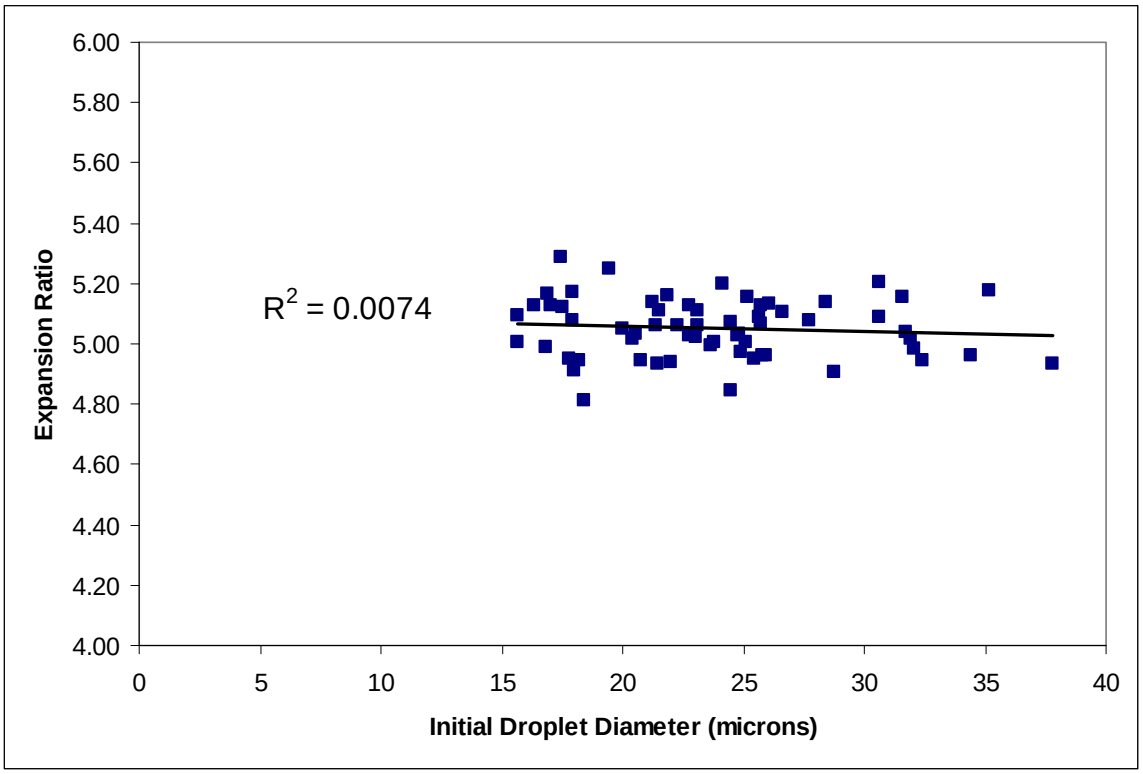

Figure 2.9: Effect of initial droplet size on the expansion ratio

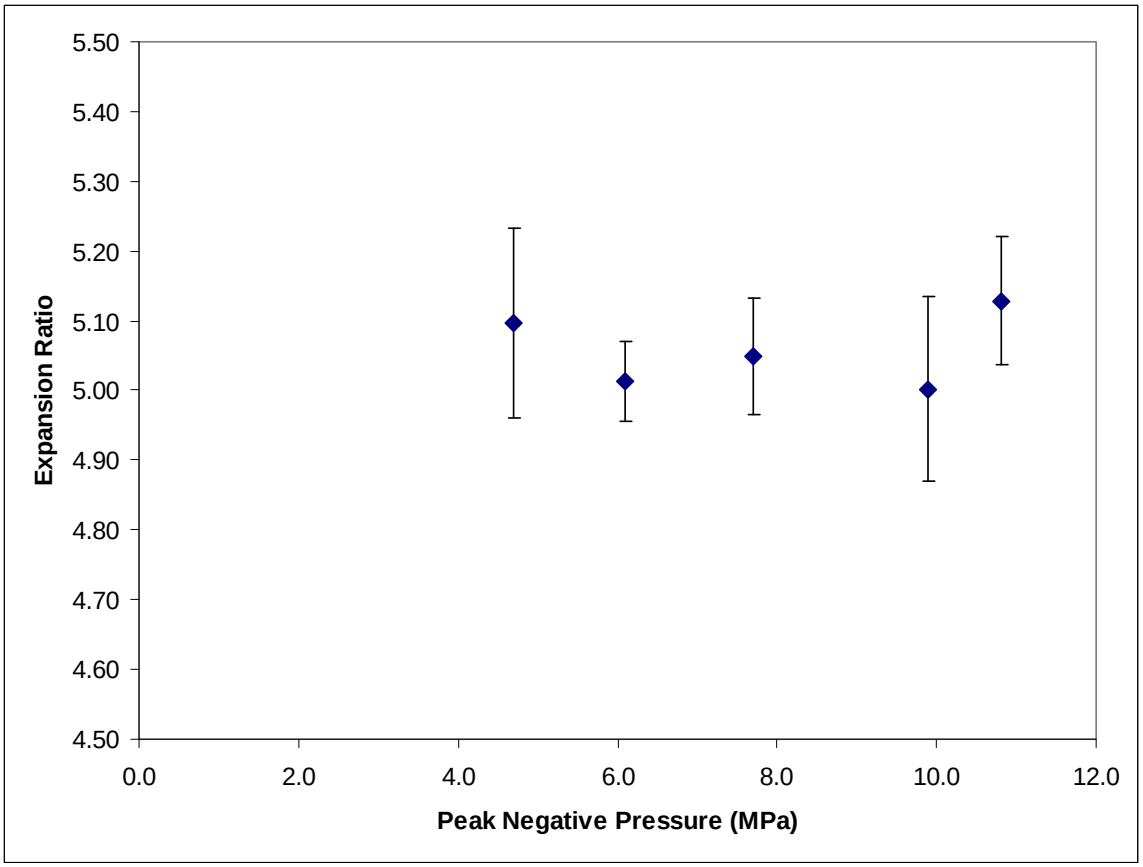

Figure 2.10: Effect of Acoustic Pressure on Expansion Ratio. (see Appendix C for T-test results)

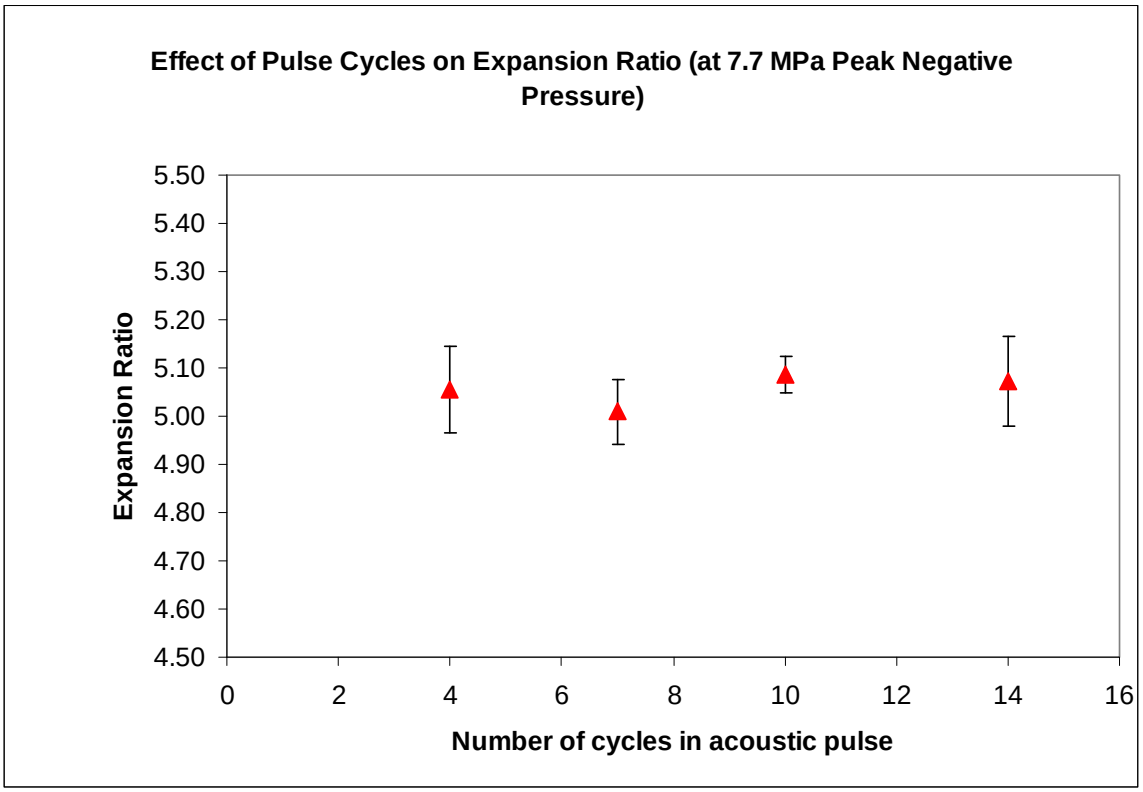

Figure 2.11: Effect of pulse cycles on expansion ratio for 7.7MPa

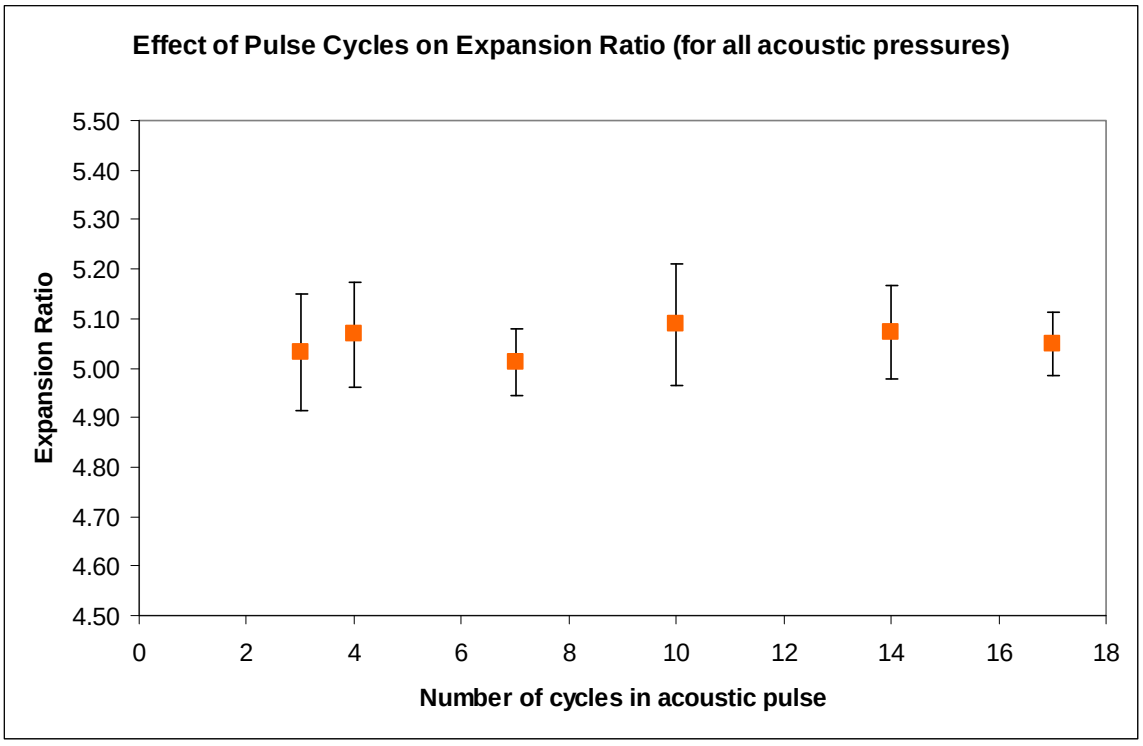

Figure 2.12: Effect of pulse cycles on expansion ratio for all acoustic pressures

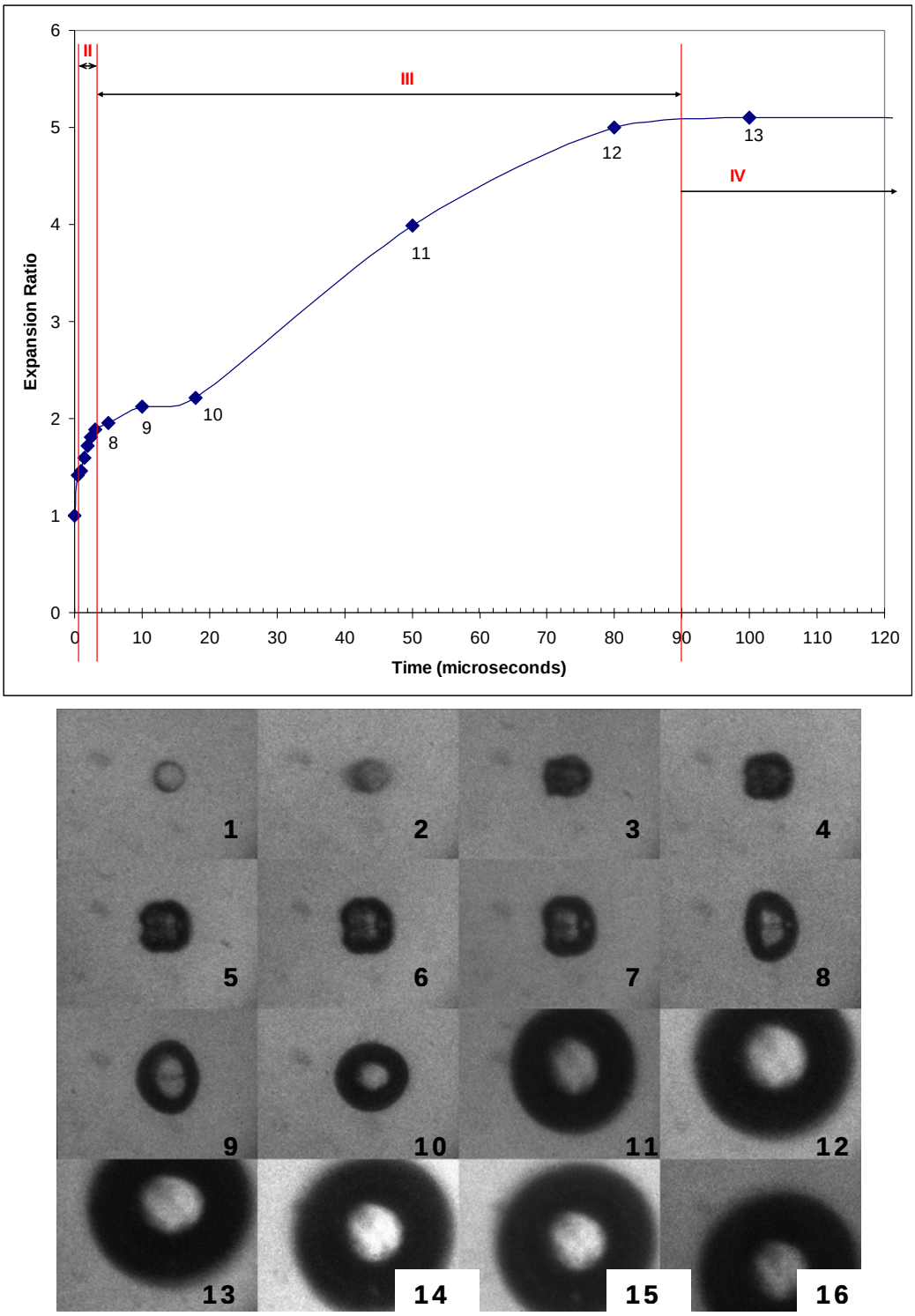

Figure 2.13: A typical set of experimental data corresponding to the experimental law of four-stage bubble growth for ADV in a rigid tube. Timeline of ADV process in microseconds: 0, 0.5, 1, 1.5, 2, 2.5, 3, 5, 10, 18, 50, 80, 100, 250, 400, 750. Initial droplet diameter = 32 microns.

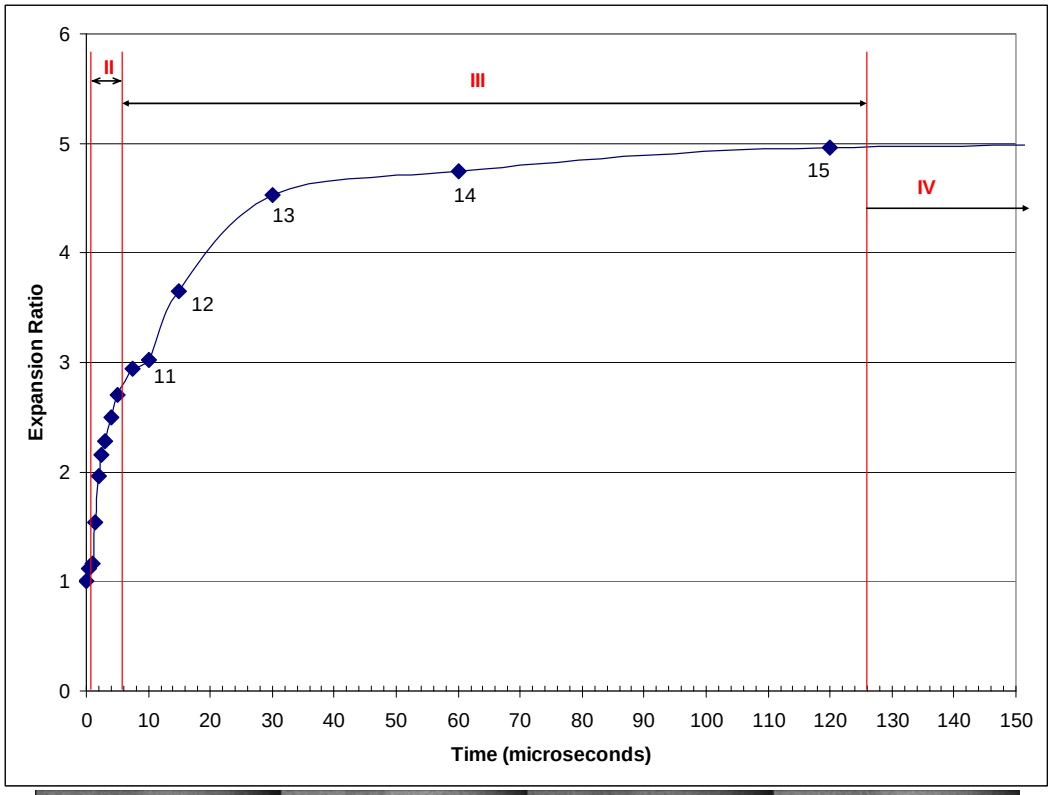

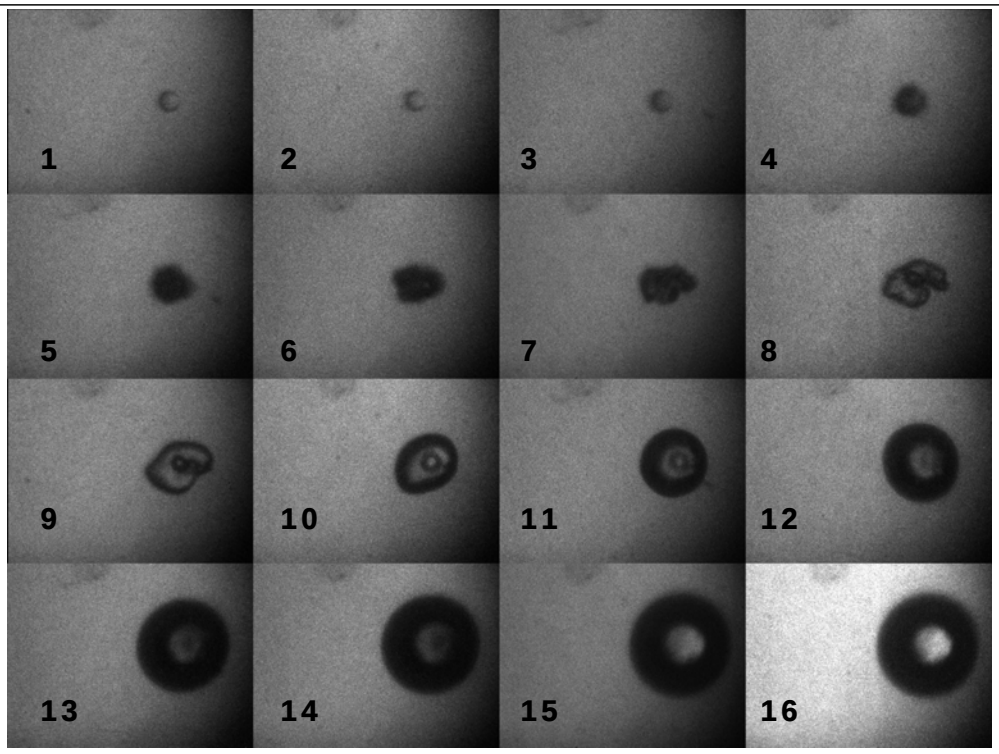

Figure 2.14: Another typical set of experimental data corresponding to the experimental law of four-stage bubble growth. Timeline of ADV process in microseconds: 0, 0.5, 1, 1.5, 2, 2.5, 3, 4, 5, 7.5, 10, 15, 30, 60, 120, 300. Initial droplet diameter = 17 microns.

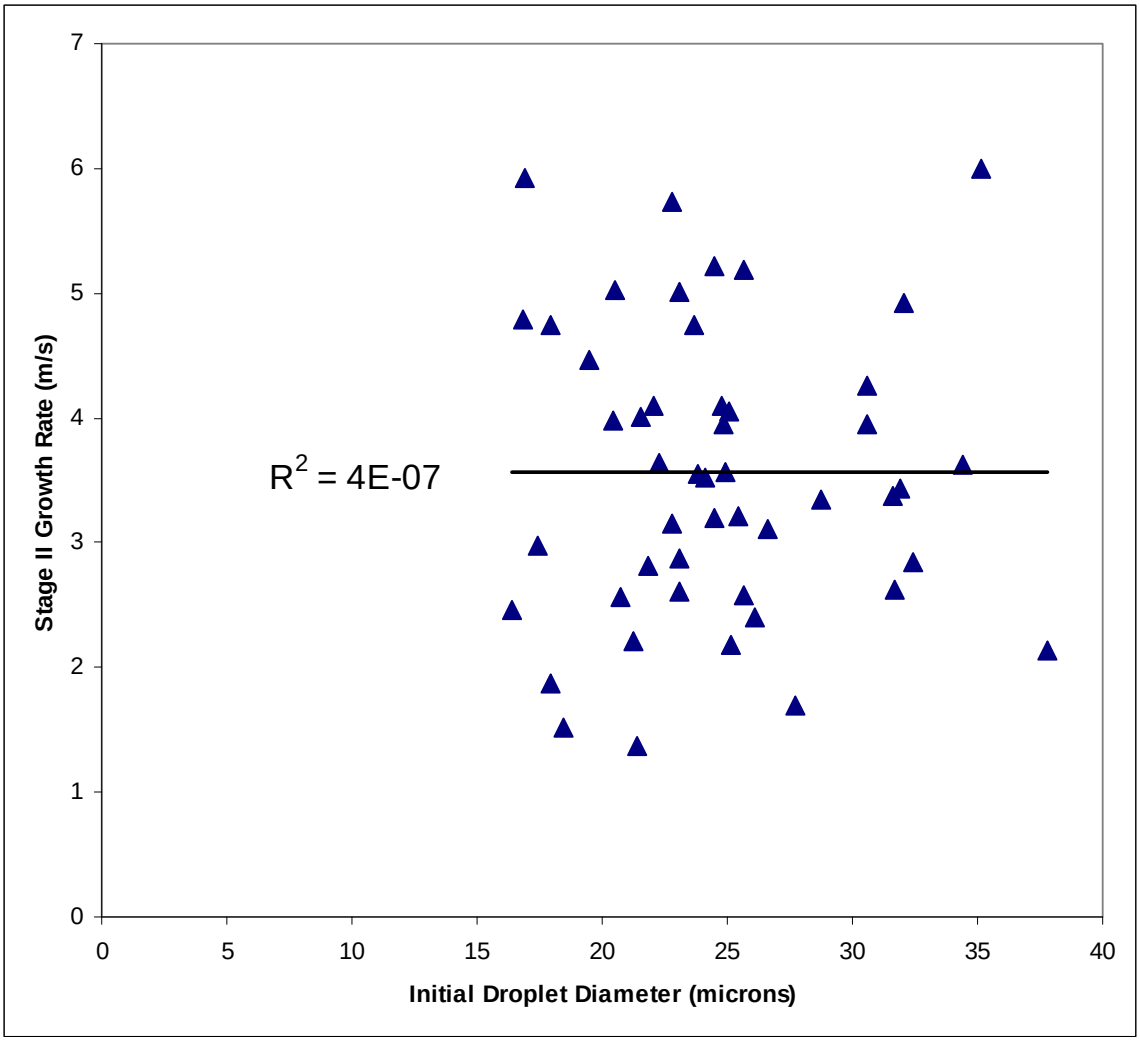

Figure 2.15: Effect of initial droplet size on the Stage II linear growth rate

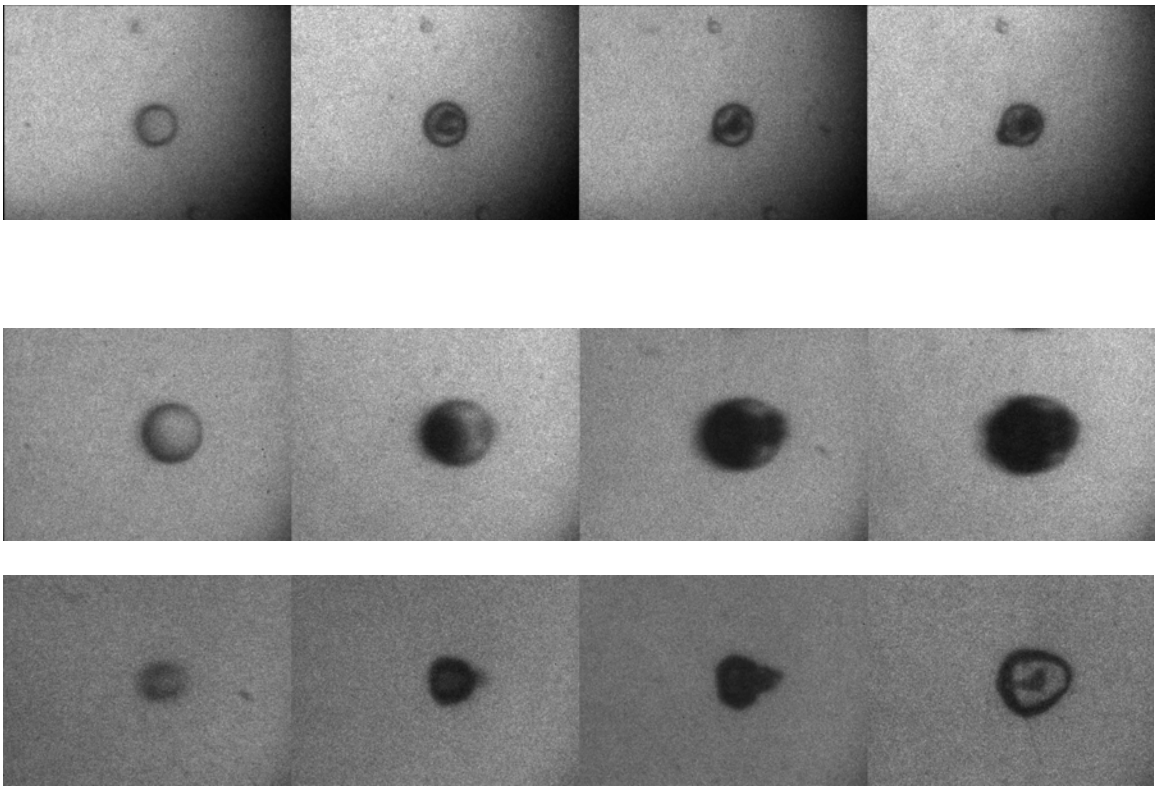

Figure 2.16: Initiation of ADV by ultrasound for three different droplets. Nucleation sites were observed in the interior of the droplet, albeit the limited resolution of details. Initial droplet diameter was 27 microns (first row), 40 microns (second row) and 23 microns (third row) respectively; frame-by-frame timelines for all 3 image sets were 0, 0.5, 1, 1.5 microseconds.

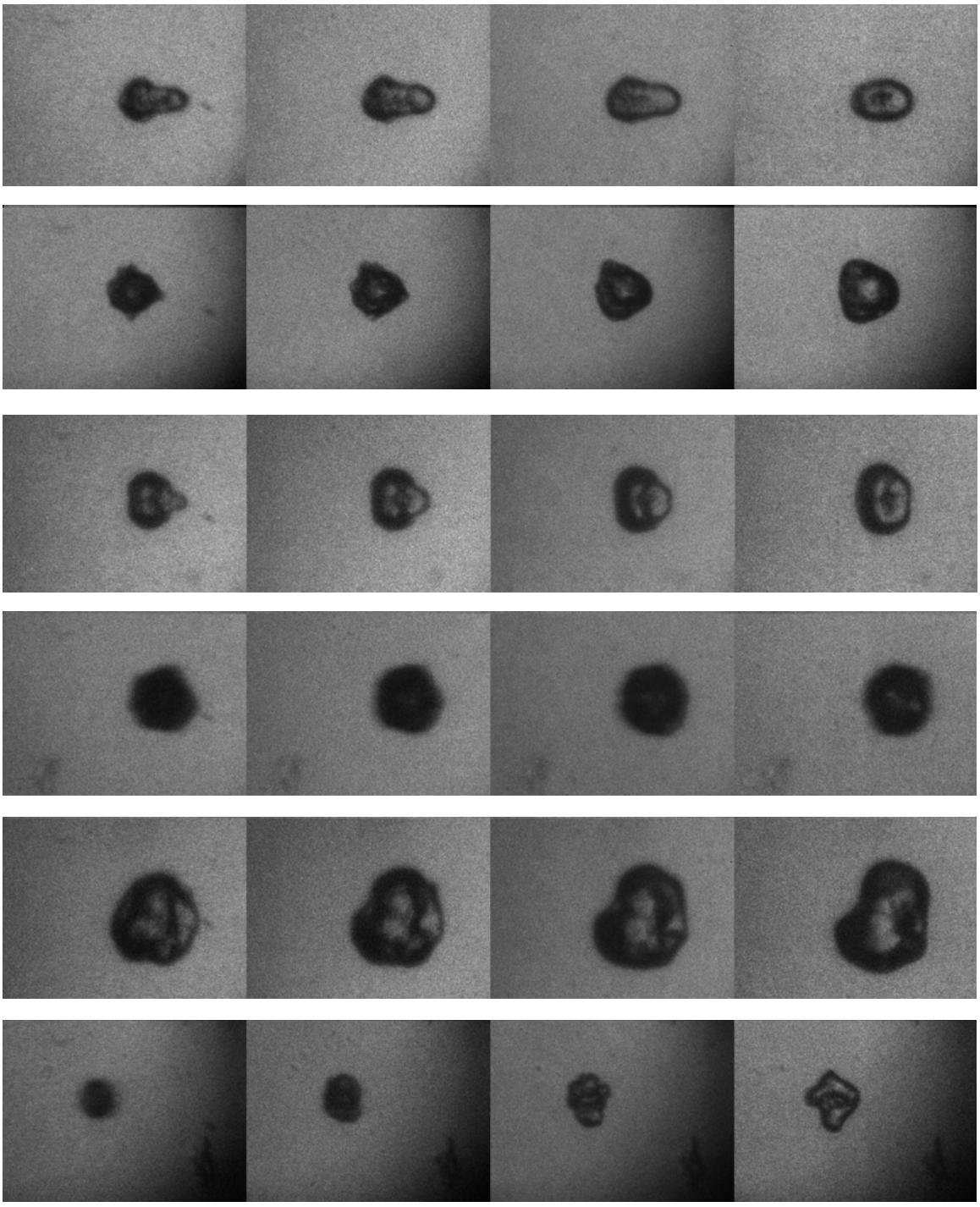

Figure 2.17: Growth in Stage II for different bubbles. The bubble boundaries were distorted and had irregularities that did not seem to follow any predictable patterns. Timelines (in microseconds) for the rows of images: (i) 2, 2.5, 3, 5 (ii through vi) 2, 2.5, 3, 4.

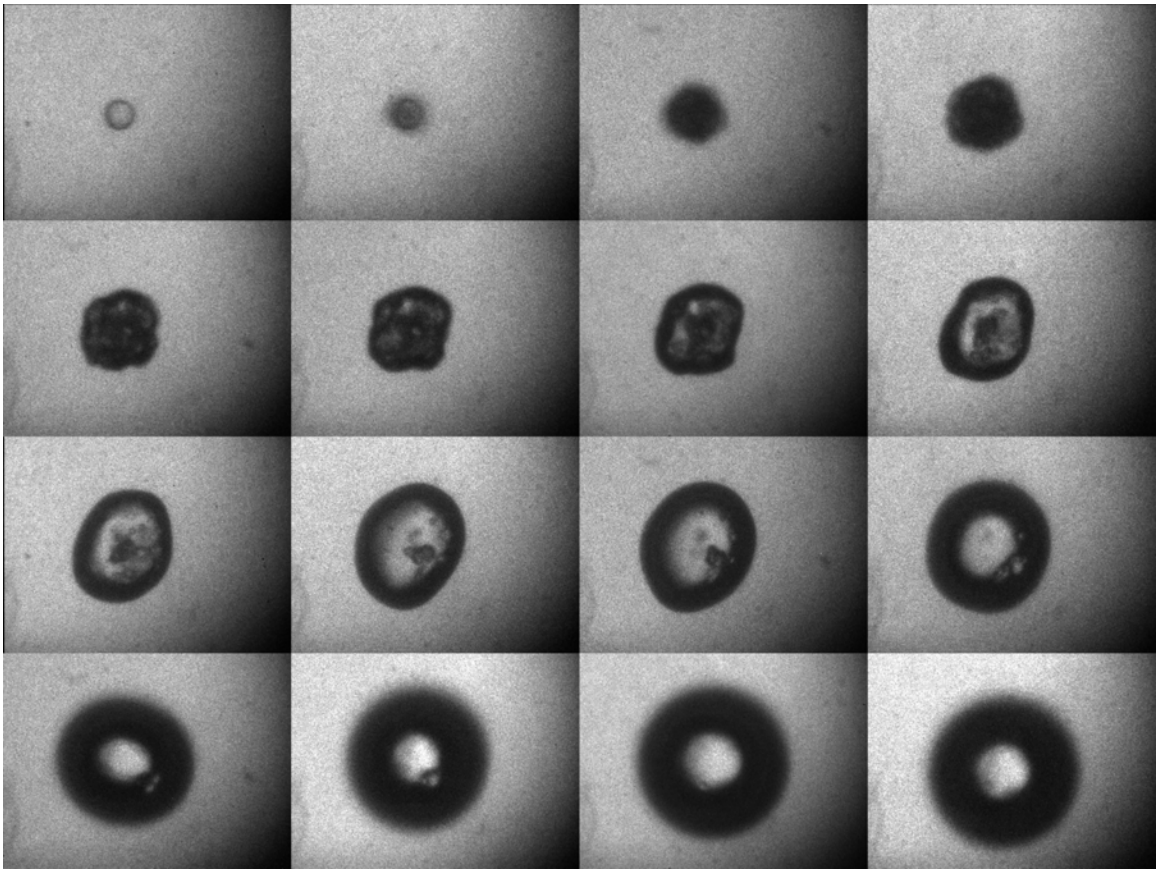

Figure 2.18: Small “bubbles” clearly visible within the bubble. Timeline in microseconds: 0, 0.5, 1, 1.5, 2, 2.5, 3, 4, 5, 7.5, 10, 15, 30, 60, 120, 300.

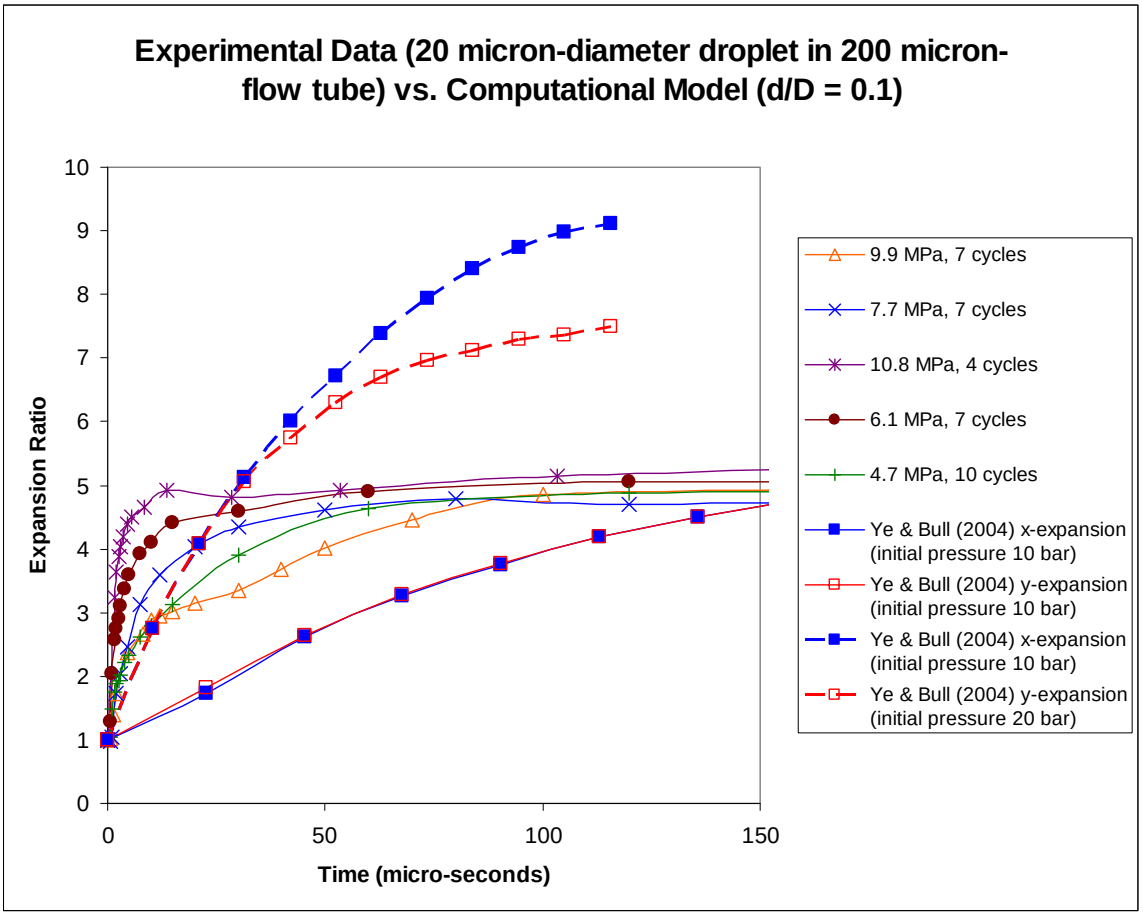

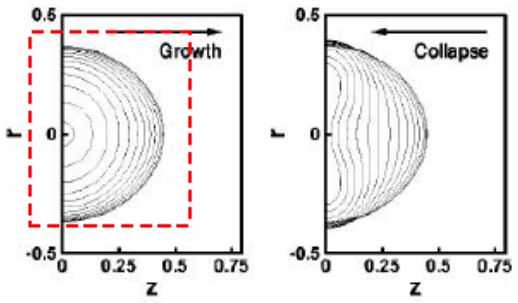

Fig. 10 Bubble shapes at different times during growth (left graph) and collapse (right graph) for case 2 in Table 1, Re =106.90, We=6.93, St=10.47, P_n=176.39 (P_h^+=20 bar), d_i=0.1. Only half of the bubble is shown because of symmetry. Time interval between successive shapes is 1 dimensionless unit (10.5×10^{-6} s/unit). The computational domain extends to 16 in both directions on the z axis.

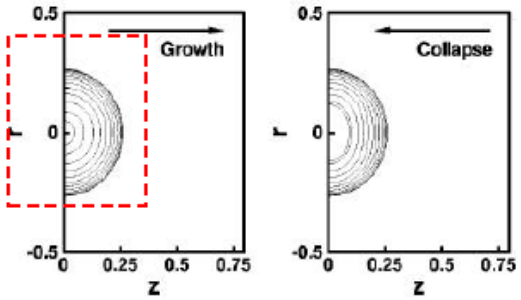

Fig. 14 Bubble shapes at different times during growth (left graph) and collapse (right graph) for case 4 in Table 1, Re =202.39, We=1.55, St=22.11, P_n=393.66 (P_h^+=10 bar), d_i=0.1. Only half of the bubble is shown because of symmetry. Time interval between successive shapes is 0.6 dimensionless unit (22.1×10^{-6} s/unit). The computational domain extends to 16 in both directions on the z axis.

Figure 2.19: Comparison of experimental results with a computational model. The evolution curves of the computational results (for initial pressure of 20 and 10 bar) correspond to the bubble shapes highlighted in dotted-line boxes respectively.

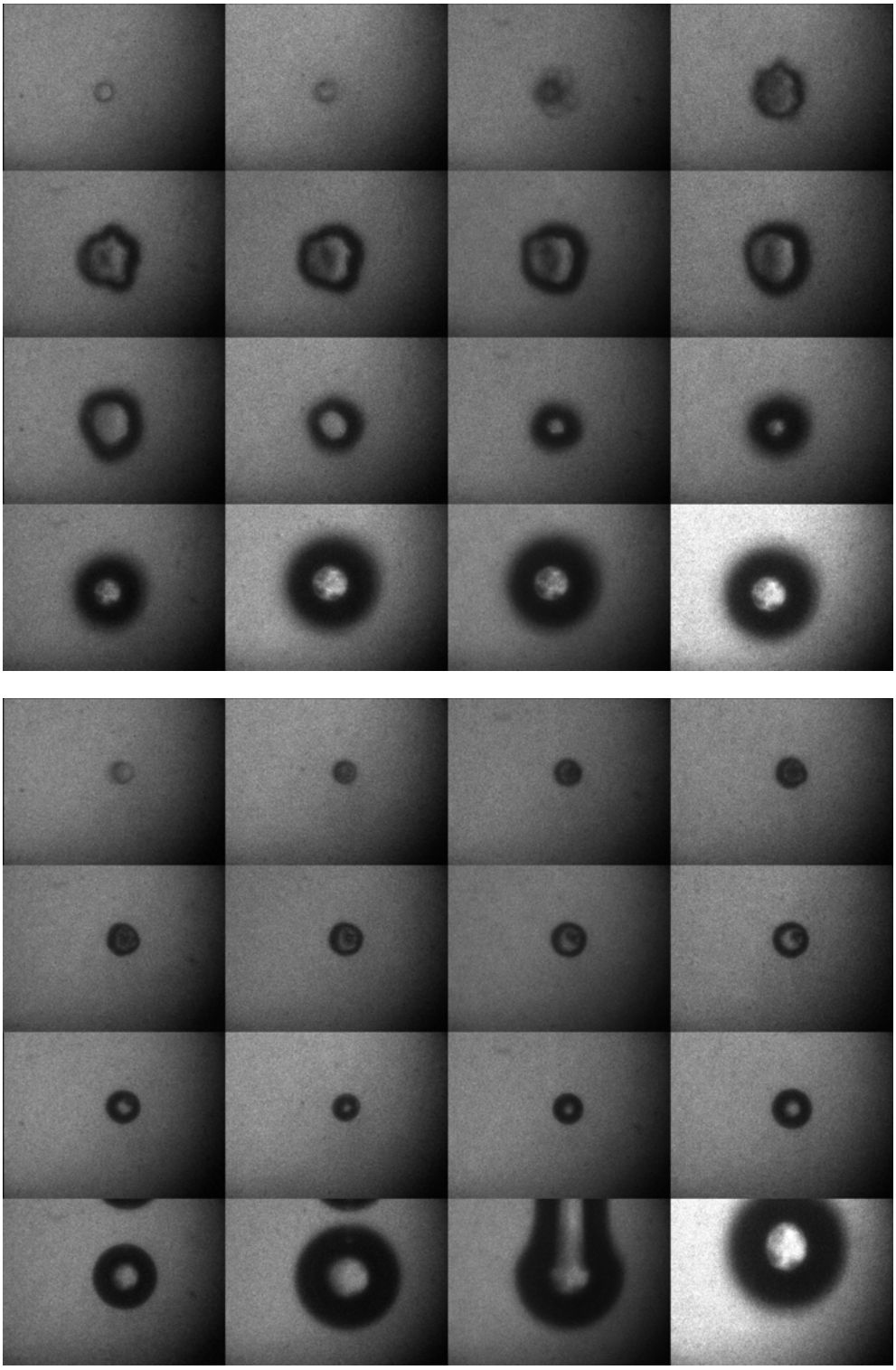

Figure 2.20: Bubble collapse was observed in these 2 image sets. (frames 9 and 10 for top image set; frames 9 to 11 for bottom image set). Timelines for both sets, in microseconds: 0, 0.5, 1, 1.5, 2, 2.5, 3, 4, 5, 7.5, 10, 15, 30, 60, 120, 300.

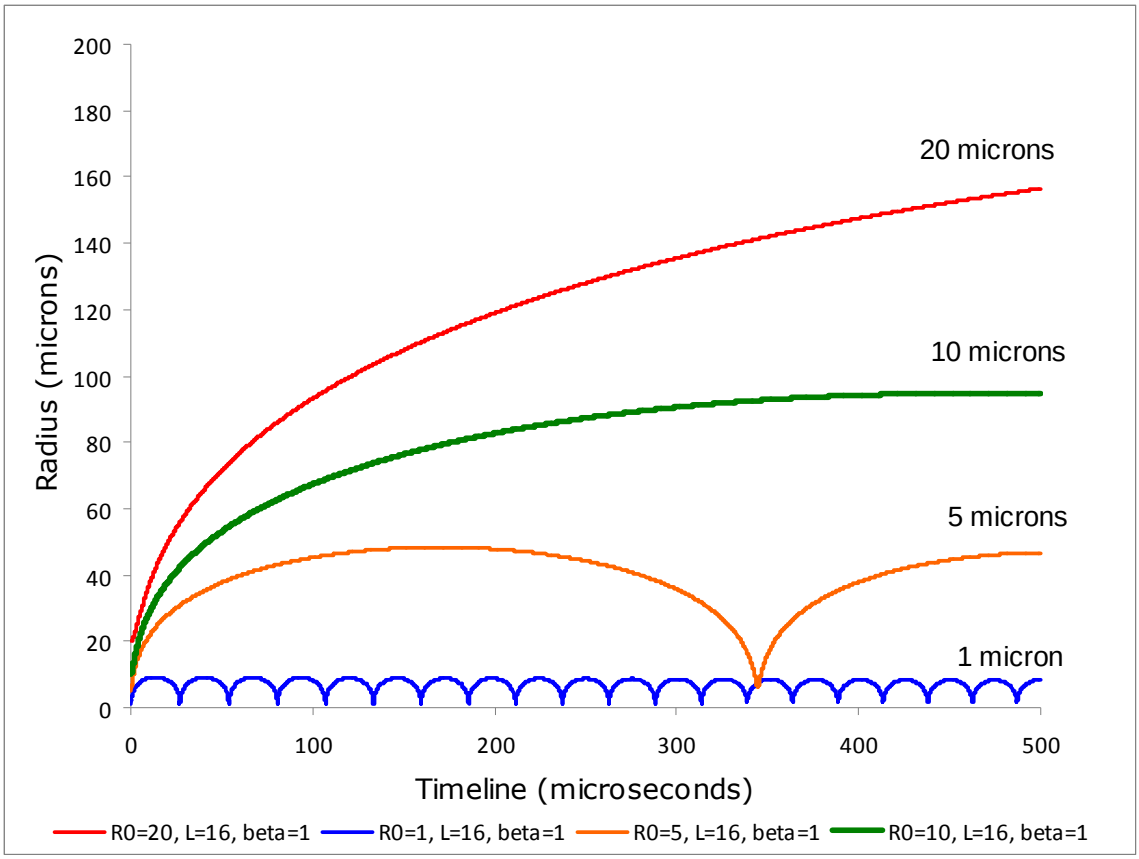

Figure 2.21: Solutions of theoretical model for different initial droplet sizes.

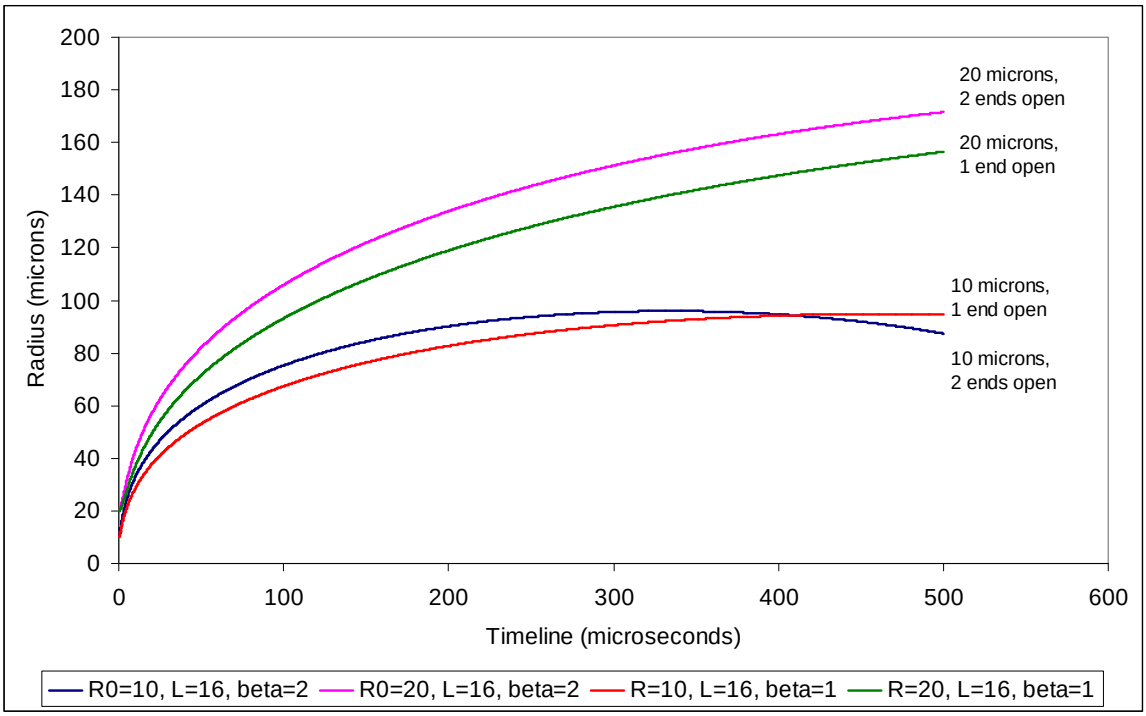

Figure 2.22: Solutions of theoretical model for the two scenarios of only one tube end being open and both ends being open.

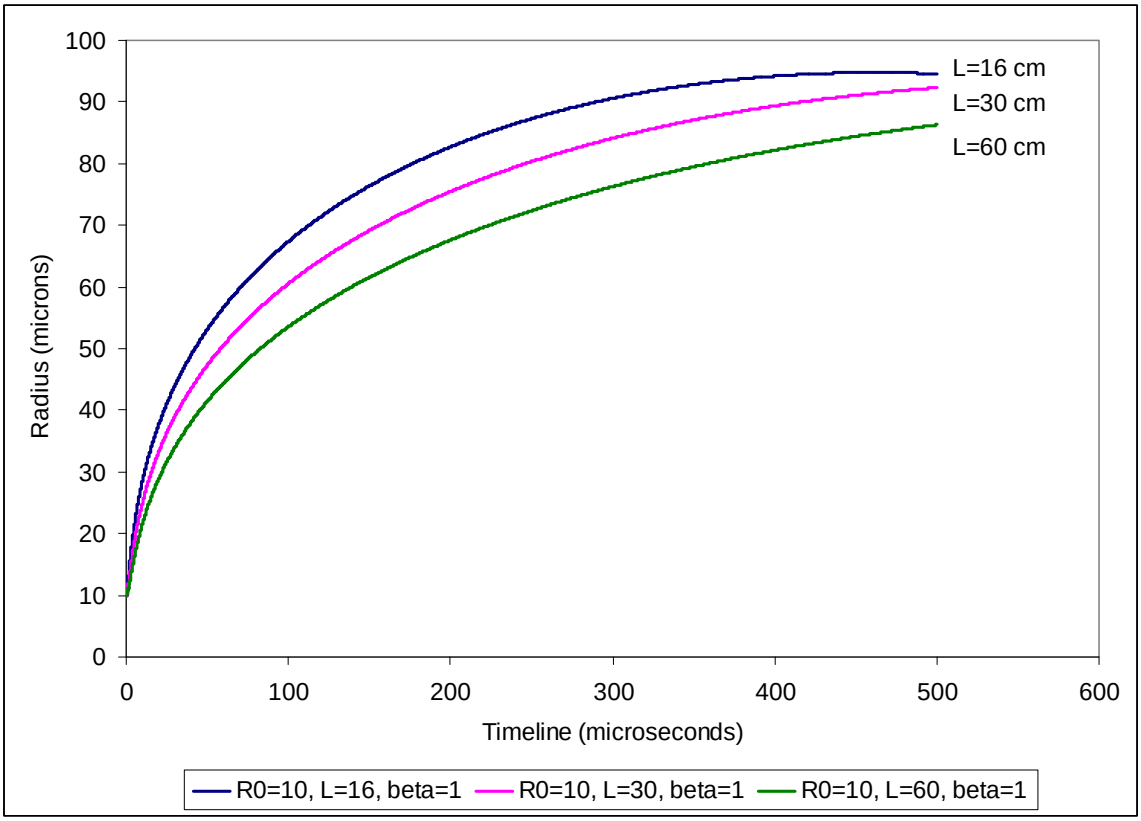

Figure 2.23: Solutions of theoretical model for different tube lengths.

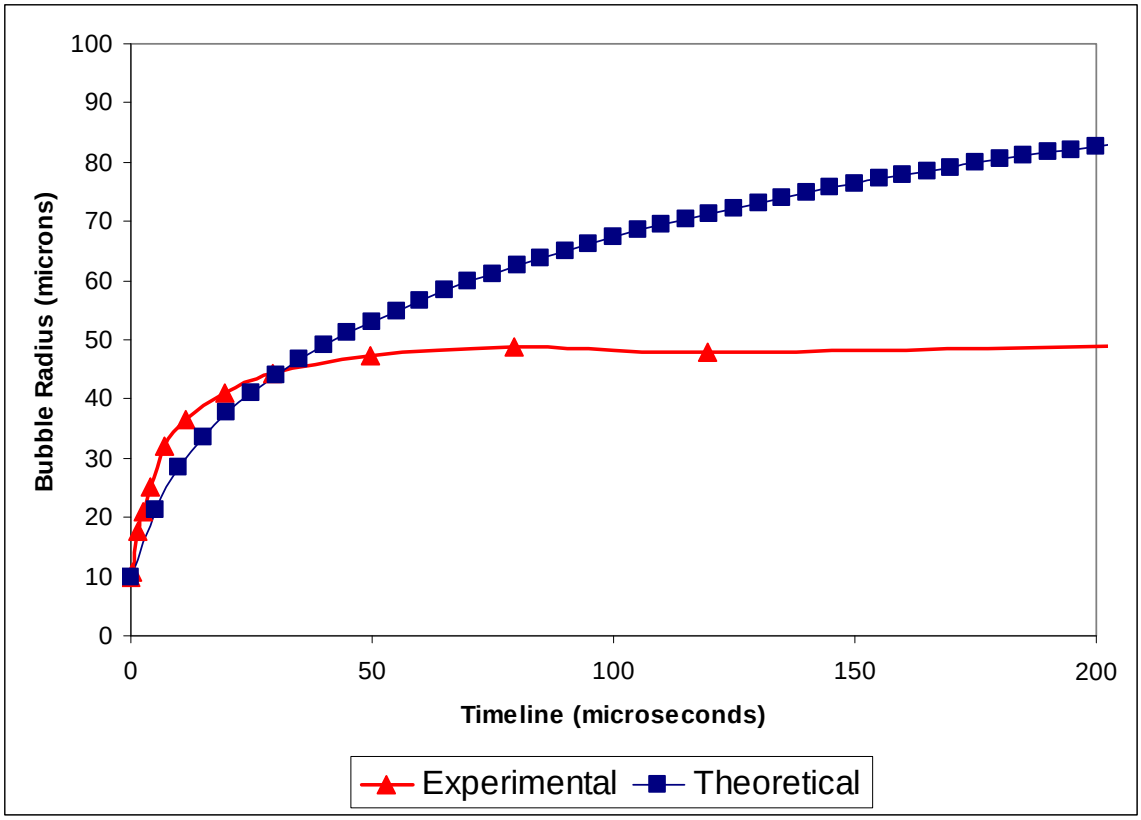

Figure 2.24: Comparison of the theoretical model with experimental results. (the experimental data corresponds to the droplet of initial 10-micron radius in Figure 2.7)

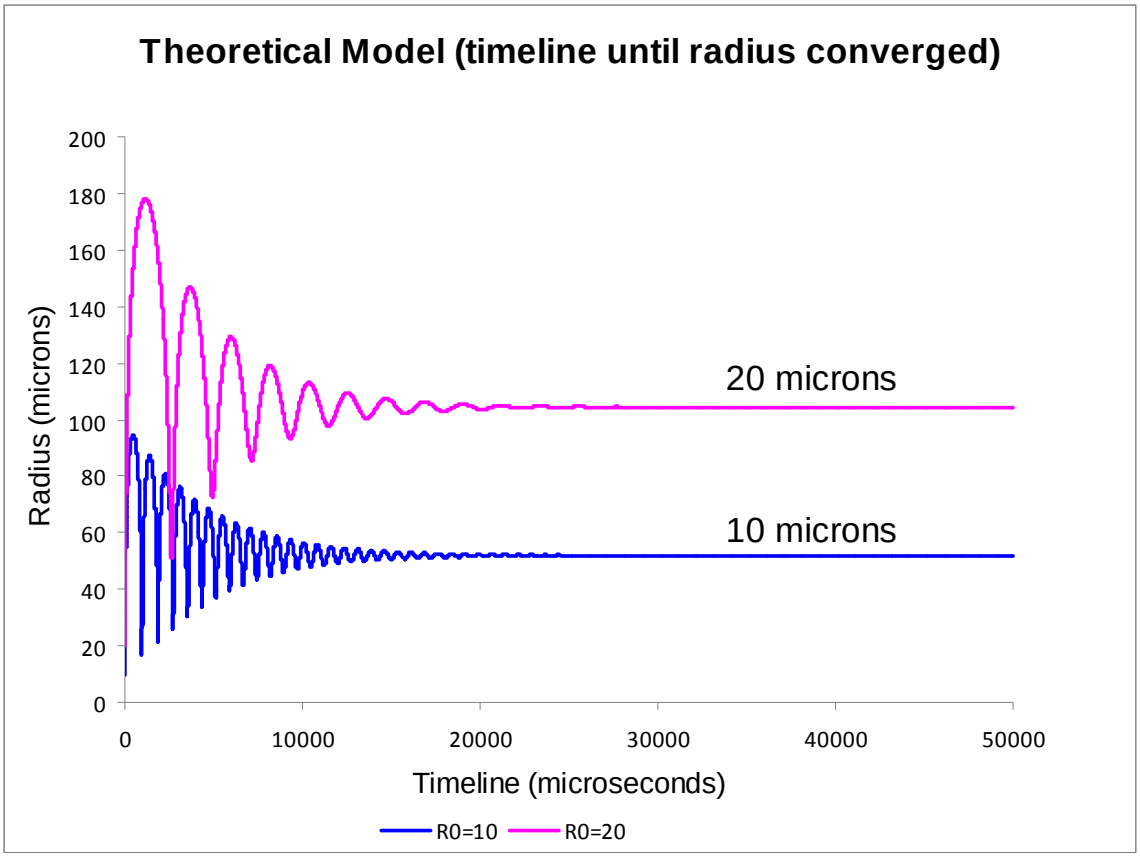

Figure 2.25: Theoretical results for initial radii of 10 and 20 microns, on a much longer timeline.

		Computational	Theoretical
1	**Oscillations predicted**	Yes	Yes
2	**Expansion Ratio**	First maximum of about 5 to 9.2 (depending on initial pressure of 10 or 20 bar); final value unknown but expected to be near 5	First maximum of about 6.5 to 9.5 (depending on initial pressure of 10 or 20 bar); final value of 5.2
3	**Initial Growth Rate**	Comparable to experimental values (Figure 2.19)	Comparable to experimental values (Figure 2.24)
4	**Assumption of phase change being complete before bubble expansion**	Yes	Yes
5	**Assumption of spherical shape being maintained**	No	Yes
6	**Prediction of bubble shape**	Reasonably good, especially when bubble nearly contacts the wall (see Chapter 3)	Not applicable
7	**Agreement with experimental time scale**	Room for improvement	Room for improvement
8	**Assumption of Initial Pressure**	Needs calibration, which was originally planned for when the model was devised	High pressure calculated from assumption in (4) and ideal gas law.

Table 2E: Comparison of computational and theoretical models

References

1. *Personal communications, on the suitability of polyacrylamide gel and other similar gels for microchannel fabrication, with Andrea Lo, Kevin Haworth and Stanley Samuel.*

2. Abbasi, T. and S.A. Abbasi, *Accidental risk of superheated liquids and a framework for predicting the superheat limit.* Journal Of Loss Prevention In The Process Industries, 2007. **20**(2): p. 165-181.

3. Bongiovanni, C., A. Dominguez, and J.-P. Chevaillier, *Understanding images of bubbles.* European Journal of Physics, 2000(6): p. 561.

4. Brennen, C.E., *Fundamentals of Multiphase Flow*. 2005: Cambridge University Press.

5. Campbell, M. and L.D. Britt, *Endotoxin has an indirect vasodilatory effect on isolated human skeletal muscle arterioles.* Archives Of Surgery, 2004. **139**(6): p. 652-654.

6. Carey, V.P., *Liquid-Vapor Phase-Change Phenomena*. 2nd ed. 2008: Taylor & Francis.

7. Das, M., et al., *How high can the temperature of a liquid be raised without boiling?* Physical Review E, 2000. **62**(4): p. 5843-5846.

8. Fabiilli, M.L., et al. *The role of inertial cavitation in acoustic droplet vaporization*. in *Ultrasonics Symposium, 2008. IUS 2008. IEEE*. 2008.

9. Haworth, K.J. and O.D. Kripfgans. *Initial growth and coalescence of acoustically vaporized perfluorocarbon microdroplets*. in *Ultrasonics Symposium, 2008. IUS 2008. IEEE*. 2008.

10. Kripfgans, O.D., et al., *On the acoustic vaporization of micrometer-sized droplets.* Journal Of The Acoustical Society Of America, 2004. **116**(1): p. 272-281.

11. Kripfgans, O.D., et al., *Acoustic droplet vaporization for therapeutic and diagnostic applications.* Ultrasound In Medicine And Biology, 2000. **26**(7): p. 1177-1189.

12. Kripfgans, O.D., et al., *Acoustic droplet vaporization for temporal and spatial control of tissue occlusion: A kidney study.* Ieee Transactions On Ultrasonics Ferroelectrics And Frequency Control, 2005. **52**(7): p. 1101-1110.

13. Parsons, J.E., C.A. Cain, and J.B. Fowlkes, *Cost-effective assembly of a basic fiber-optic hydrophone for measurement of high-amplitude*

therapeutic ultrasound fields. Journal Of The Acoustical Society Of America, 2006. **119**(3): p. 1432-1440.

14. Parsons, J.E. and K.J. Haworth, *Fiber Optic Probe Hydrophone Operator's Manual (Version 2.2).* Basic Radiological Sciences Division, Department of Radiology, University of Michigan, 2009.

15. Poepping, T.L., et al., *A thin-walled carotid vessel phantom for doppler ultrasound flow studies.* Ultrasound In Medicine And Biology, 2004. **30**(8): p. 1067-1078.

16. Shepherd, J.E. and B. Sturtevant, *Rapid Evaporation At The Superheat Limit.* Journal Of Fluid Mechanics, 1982. **121**(AUG): p. 379-402.

17. Shusser, M. and D. Weihs, *Explosive boiling of a liquid droplet.* International Journal Of Multiphase Flow, 1999. **25**(8): p. 1561-1573.

18. Wustneck, N., et al., *On the dissolution of vapors and gases.* Langmuir, 2007. **23**(4): p. 1815-1823.

19. Ye, T. and J.L. Bull, *Direct numerical simulations of micro-bubble expansion in gas embolotherapy.* Journal Of Biomechanical Engineering-Transactions Of The Asme, 2004. **126**(6): p. 745-759.

Chapter 3

Bubble Evolution in a Rigid Tube at Room Temperature and Some Interesting Phenomena at Both Temperatures

3.1 Synopsis

The previous chapter discussed the bubble evolution in a rigid tube at physiological temperature.

The present chapter will discuss the experimental results for bubble evolution at room temperature, which will be shown to be significantly different from the bubble evolution at physiological temperature. Possible reasons for the differences between the two types of bubble evolution will be expounded.

While the experimental law of 4-stage growth proposed for physiological-temperature bubble evolution might not apply to the scenario at room temperature, a comparison of the initial growth rate can still be made. Although a systematic study of bubble evolution at different temperatures was not conducted, several sets of experimental data collected at different temperatures will be compared and discussed.

The latter part of this chapter will present two phenomena, namely, coalescence and contact of the bubble with the tube walls, observed during the experiments at both physiological and room temperatures. Where available, quantitative information will be discussed but the bulk of the discussion will be done qualitatively through the presentation of interesting images.

3.2 Materials, Methods and Experiments

Except for the absence of the temperature-control setup, all descriptions of experimental-related setup and procedures in Section 2.2 are applicable to the room-temperature experiments.

At room temperature, the water in the tank was measured to be at 67°F (or about 20°C). Nearly 100 experiments were run at room temperature, of which 25 image sets were chosen for detailed analysis.

3.3 Results and Discussions

3.3.1 Examples of Images

Two examples, with their respective evolution plots, are shown in Figures 3.1 and 3.2, with one showing a longer timeline of nearly 600 μs and the other with a timeline of about 150 μs.

The images showed the arrival of ultrasound (Frame 2, Figure 3.2), nucleation (Frame 4, Figure 3.1), progress in vaporization (Frames 4 to 8, Figure 3.2), and possibly partial condensation (Frames 9 to 10 of both figures). These will be discussed in detail below.

3.3.2 Expansion Ratio and Growth Rate

The developmental details of nucleation, which lasted a total of about 0.6 μs, are shown in Figure 3.3. Consistent with the findings in [2], the nucleation occurred on the central axis of the droplet. Interestingly, the images revealed that the nucleation started at two opposite points and eventually merged into each other. The droplet remained at about the same size and spherical shape during the nucleation process before increasing in size and distorting its spherical shape at around 0.6μs.

The average **final** expansion ratio (i.e. final bubble diameter divided by initial droplet diameter) for the room-temperature experiments was **1.13** (standard deviation 0.061). However, the final expansion ratio was lower than the maximum ratio attained during the evolution. As seen from Figures 3.1 and 3.2, the bubble attained its maximum size at around 2 to 3 μs on the timeline. The average **maximum** expansion ratio attained during all the bubble evolutions was **1.43** (standard deviation 0.257).

It was not obvious what the composition of the final product (i.e. shown in the 16th frame) was. Could it be a DDFP gas bubble suspended in unconsumed or condensed liquid DDFP? Or could it be made entirely of liquid

DDFP that underwent a flip-flop phase change back into a supercooled state? The evolution curve of Figure 3.5 showed that the bubble expanded in an oscillatory fashion, with collapses or near-collapses interspersing the growth (note: (i) the maximum expansion was not captured because the second point in the timeline was at 65 μs, already well past the point of 2 to 3 μs; (ii) the curves in Figures 3.1 and 3.2 did not show the oscillatory behavior in latter times because of an aliasing effect, i.e. the limitation of having only 16 frames resulted in undersampling at latter times). The presence of the oscillatory behavior suggested that the bubble contained gas (compressible) rather than liquid (incompressible). A closer examination of the image frames (Figure 3.4) confirmed that the inner bubble had also grown within the expanded boundary.

In Figure 3.6, after the chaotic phase change shown in Frames 5 to 8, the inner bubble evolved into a dumbbell-like shape (Frame 10), split into two smaller bubbles (Frame 11 and 12) before coalescing back into one inner bubble (Frame 13 and 14). Comparatively, at physiological temperature (Figure 3.7), the interior showed a dumbbell-like structure (Frame 5 and 6) that never separated fully but instead merged into one contiguous area (Frame 9). Another key difference between the room-temperature evolution and physiological-temperature evolution was that the former saw a shrinkage of the inner bubble (Frame 14 and 15 of Figure 3.6), vis-à-vis the continued expansion in the latter (Frame 10 onwards in Figure 3.7). Despite our images showing clearly the reduction in volume of the inner bubble, the

question on whether it was due to a pure decrease in gas volume, or a partial condensation of the gas, or a combination of both, remains unanswered.

Since the mechanisms at work in a room-temperature bubble evolution could be different from those in a physiological-temperature bubble evolution, the 4-stage growth proposed in Chapter 2 would not apply to room-temperature cases. To characterize the evolution at room-temperature, the initial linear growth rates during the first few microseconds were measured, and their average value was determined as **2.70 m/s** (with standard deviation of 1.20 m/s and a R^2 correlation factor for linearity of 0.883). Therefore, compared to the Stage II growth rate of 3.56 m/s for physiological-temperature evolution, the initial bubble growth at room temperature was slower (unpaired T-test, assuming unequal variances, gave a p-value = 0.0134 < 0.05). One could argue that basing the comparison on the Stage II growth rate was not an exact apples-to-apples comparison in terms of the timelines. Qualitatively, the same conclusion would still be reached if the comparison were based on the Stage I growth rate, because Stage I growth was more explosive and hence faster than Stage II growth.

3.3.3 Effect of Initial Droplet Size and Temperature

As shown in Figure 3.8, the expansion ratio (final and maximum) for room-temperature was independent of the initial size of the droplet, just as for physiological-temperature.

Comparison between the results at the two different temperatures was made in the aforementioned discussions. Although there was no systematic study of how varying temperatures would affect the bubble evolution, a few cases of bubble evolution at temperatures between the room and physiological values were available. These were side benefits obtained from the process of fine-tuning the lighting and SIM software parameters while waiting for the water to heat up. These results will be presented qualitatively as follows.

Figures 3.9 to 3.11 show bubble evolution at temperatures of 73°F (23°C), 82°F (28°C) and 88°F (31°C) respectively. The results were surprisingly consistent with what one would expect from knowing that the boiling point of DDFP at atmospheric pressure is 84°F (29°C). At an ambient temperature above the boiling point of DDFP (Figure 3.11), the bubble evolution proceeded just like for the cases at physiological temperature. On the other hand, at an ambient temperature below the boiling point of DDFP (Figure 3.9), the bubble evolution was similar to that of the room-temperature experiments. At an ambient temperature very close to the boiling point of DDFP but still below it (Figure 3.10), it appeared that the liquid DDFP was not fully consumed and/or there was partial condensation, resulting in an evolution more similar to the room-temperature case than the physiological-temperature case.

In all, from the experiments shown in Figures 3.9 to 3.11, plus the aforementioned findings of a slower initial growth rate and the early

attainment of the maximum expansion ratio (at about 2 to 3 μs), it can be concluded that an ambient temperature below the boiling point of DDFP is thermodynamically unfavorable for the bubble evolution.

3.3.4 Coalescence

Coalescence between two or more droplets vaporizing near each other was observed in [1], as a result of Bjerknes forces moving the centers of mass of the droplets towards each other at an average droplet-droplet impact velocity of 9 m/s. It should be noted that this coalescence between droplets occurred early in the timeline, within the first few microseconds.

In our experiments, coalescence was also observed in some experiments, both physiological-temperature and room-temperature included. However, due to the relatively larger droplets used in our experiments, the same kind of droplet-droplet coalescence reported in [1] was not observed. Instead, coalescence due to expanding bubbles growing towards each other was observed. Figures 3.12 to 3.14 show coalescence of bubbles under physiological temperature conditions (Frame 15 of Figure 3.14 captured the moment of fusion between the two bubble boundaries). The average approach speed during coalescence, based on data from six experiments, was determined as **0.31 m/s** (with standard deviation of 0.099 m/s).

Coalescence of bubbles under room temperature conditions produced some fascinating images, as shown in Figures 3.15 to 3.18.

Figure 3.15 shows the initiation of vaporization (Frame 5), followed by the coalescence (Frames 6 to 9), of four droplets of unequal initial sizes. Surprisingly, these four bubbles coalesced into a single bubble far smaller than what one would expect from four droplets. However, the interior of the final bubble showed a dark intensity, suggesting that it contained a high amount of gas, perhaps compressed within the bubble boundary of a rather small diameter.

In Figure 3.16, two droplets in close proximity coalesced while a tiny, third droplet just to the right of and touching these two droplets did not coalesce into them (note: all three droplets vaporized). Another interesting observation was the presence of a tiny inner bubble above the main inner bubble (see Frames 9 to 14). Its disappearance in Frame 15 suggests that it coalesced with the main inner bubble.

The presence of more than one inner bubble was also observed in Figures 3.17 and 3.18. Figure 3.17 shows clearly the distinct and separate vaporization of the two droplets (Frame 4 to 6), followed by coalescence (Frame 7 to 9). Surprisingly, the subsequent frames 10 to 16 revealed the existence of three separate inner bubbles which reduced to two, then finally to one, via further coalescence. During these occurrences of coalescence of the outer as well as inner bubbles, the dumbbell shape of the outermost boundary was maintained. In Figure 3.18, the same events seemed to take place (note: the third adjoining droplet remained unvaporized throughout the experiment), except that, upon close scrutiny, the two bubbles never really coalesced.

When a single droplet underwent ADV at room temperature, the interior sometimes showed two inner bubbles (Figure 3.6, for example). It would be reasonable to expect the formation of up to 4 inner bubbles when two droplets vaporized and coalesced. These inner bubbles would eventually coalesce too, and form a single inner bubble.

3.3.5 Contact with Walls

Several image sets of bubble evolution under physiological temperature conditions exhibited contact of the bubble with the tube walls. In all these image sets, the tube walls did not exhibit any movement or deformation, as expected for a rigid tube.

Figures 3.19 to 3.21 show the expanding bubble growing towards one wall and making contact with the wall. (note: in all such cases, the bubble first contacted the wall on the right-hand side in the image, probably due to the remnant momentum from the ultrasound which came in from the left)

By judging the shape of the bright central region of the bubble, it was observed that the bubble rebounded after contacting the wall (convex half-moon shape of central bubble region in Frame 14 and 15 of Figure 3.19). In Figure 3.19, the bubble was clearly still expanding throughout the process of contacting the wall, as Frame 16 showed the bubble had expanded to contact both walls. In Figure 3.20, the bubble shape went from being elongated in the longitudinal (wall) direction (Frame 12) before the contact, to being

slightly elongated in the transverse direction (Frame 15), before equilibrating into a spherical form (Frame 16).

Figure 3.21 was used to determine the approach speed of the bubble before the contact with the wall. By measuring the gap between bubble and wall in Frame 11 to 15, and knowing the corresponding timeline, the approach speed was estimated to be **0.32 m/s**. On one hand, the similarity between this value and the approach speed during coalescence did not seem surprising, since both events (contact with wall and coalescence) were observed to occur at around the same time in the timeline. But, on the other hand, despite having a similar magnitude, the velocity during coalescence was in the longitudinal direction while the contact velocity was in the transverse direction. Further experiments will be needed to confirm these preliminary findings.

3.4 Concluding Remarks

Depending on whether the ambient temperature is below or above the boiling point of the DDFP inside the droplet, bubble evolution in a rigid tube proceeds differently. The differences are both visible in the images, and also in the expansion ratios, initial growth rates and presence or absence of oscillations.

The phenomenon of coalescence due to expanding bubbles growing towards each other was observed at both physiological and room temperatures. The images of coalescence at room temperature revealed the

presence of inner bubbles that could coalesce within the boundary of the outer bubble.

Several image sets of the expanding bubble coming into contact with the wall revealed that the bubble tended to elongate in the longitudinal tube direction before the contact, and re-assumed a spherical shape after rebounding from the contact.

Further work by means of experimental, theoretical and computational methods might shed more light on the details of ADV and bubble evolution. Many aspects of bubble evolution in a rigid tube remain to be investigated. In addition, bubble evolution in a flexible tube present an unexplored and possibly very fertile territory for future research.

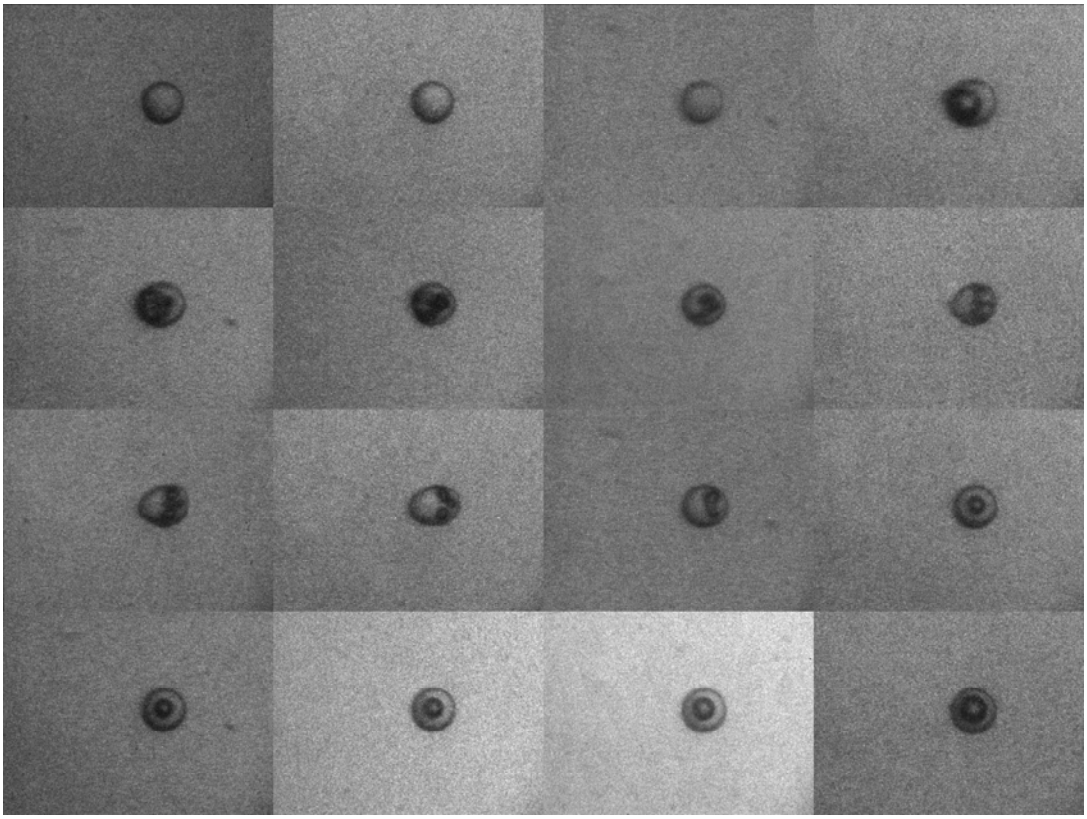

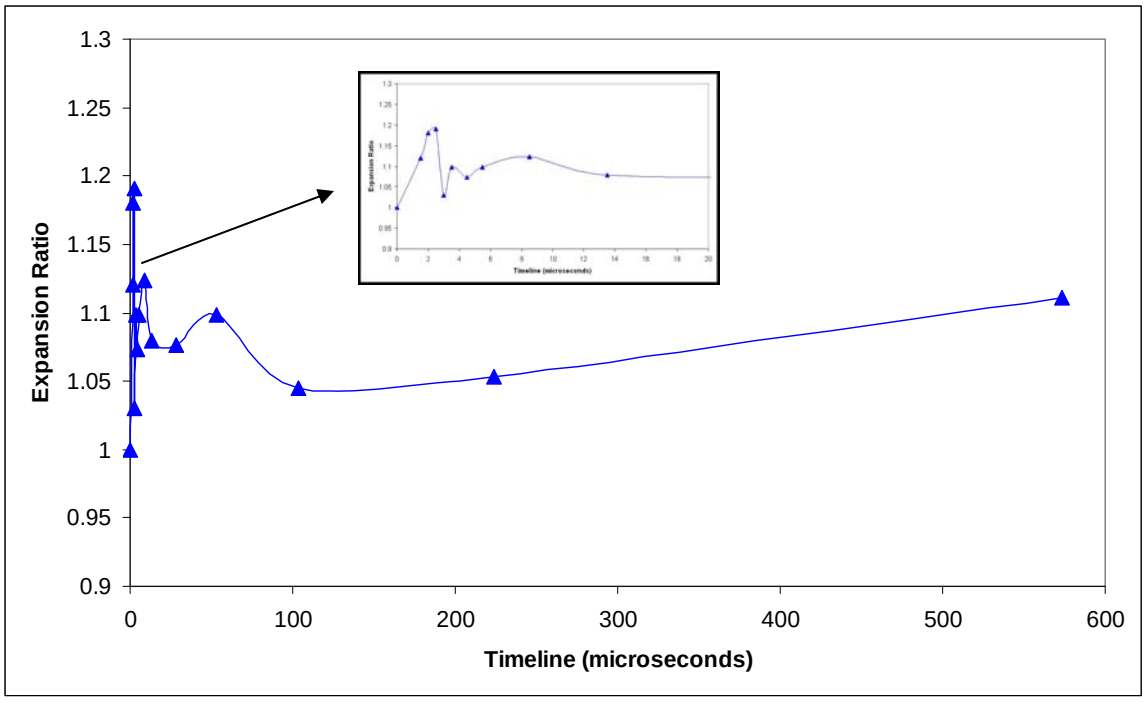

Figure 3.1: Evolution of a droplet of initial diameter 32 microns. Timeline in microseconds, starting from Frame 2: 0, 1.5, 2, 2.5, 3, 3.5, 4.5, 5.5, 8.5, 13.5, 28.5, 53.5, 103.5, 223.5, 573.5. (the inset picture shows a zoomed-in view of the evolution for the first 20 microseconds)

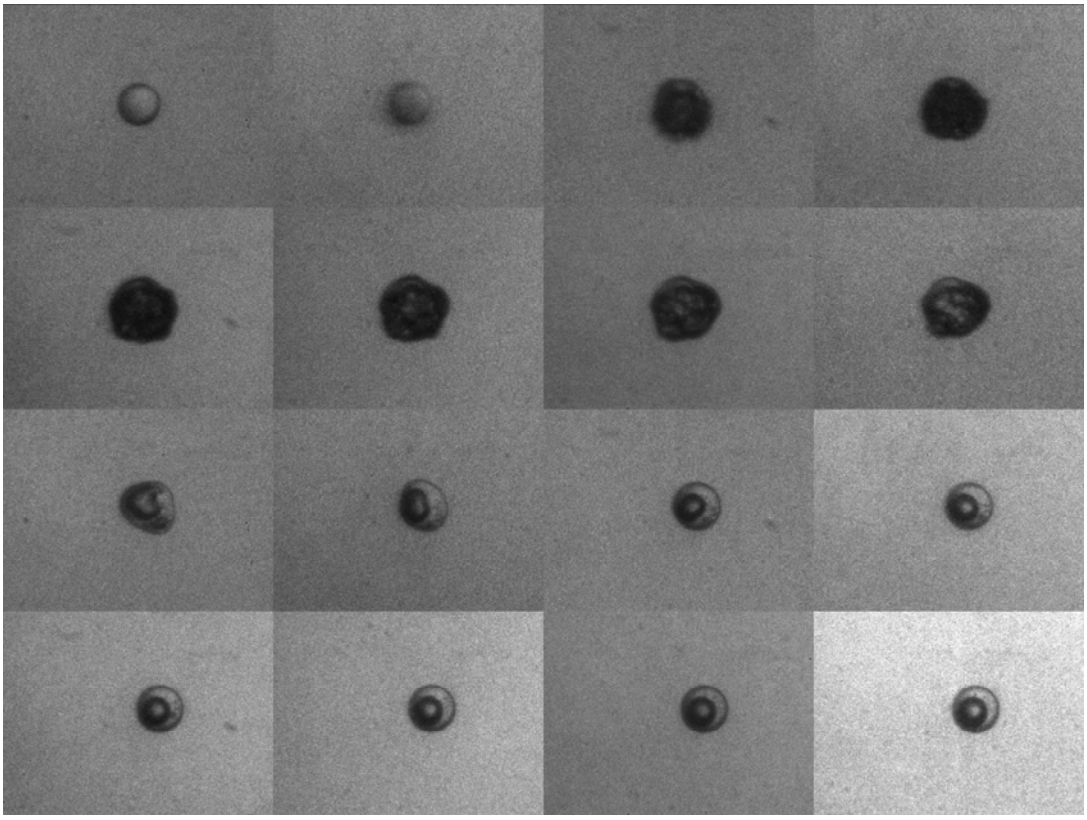

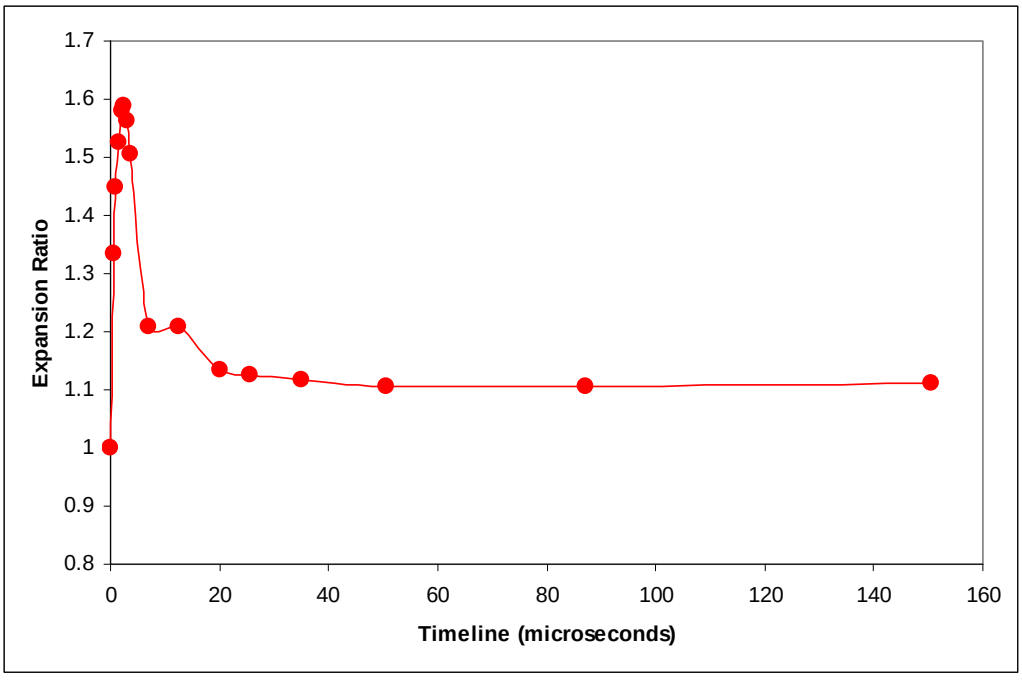

Figure 3.2: Evolution of a droplet of initial diameter 31 microns. Timeline in microseconds: 0, 0.505, 1.01, 1.515, 2.02, 2.525, 3.03, 3.535, 7.04, 12.545, 20.05, 25.555, 35.06, 50.565, 87.07, 150.575.

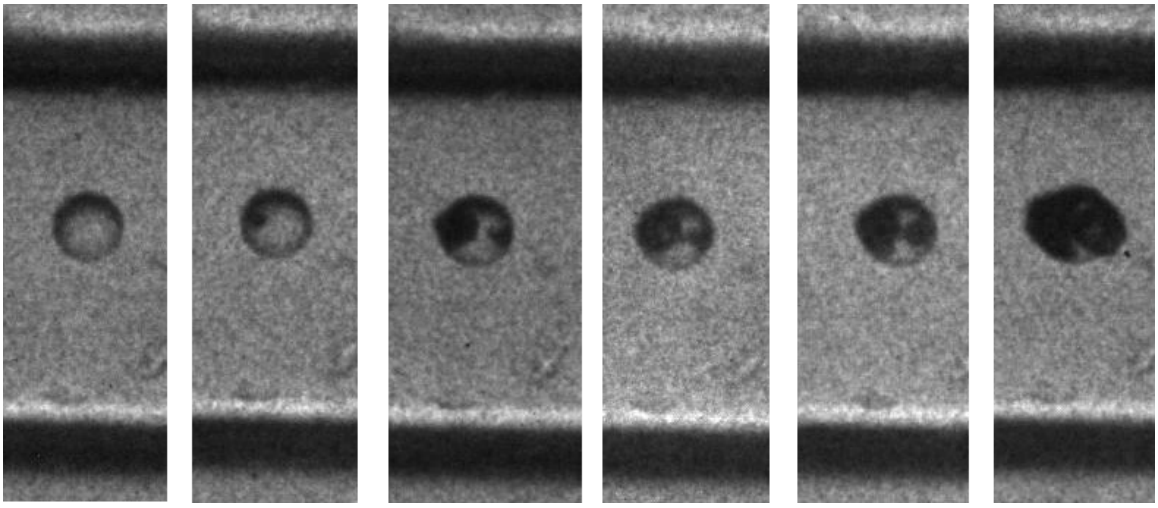

Figure 3.3: Images showing progression of nucleation in a droplet of initial diameter 40 microns. Timeline in microseconds: 0, 0.12, 0.24, 0.36, 0.48, 0.6.

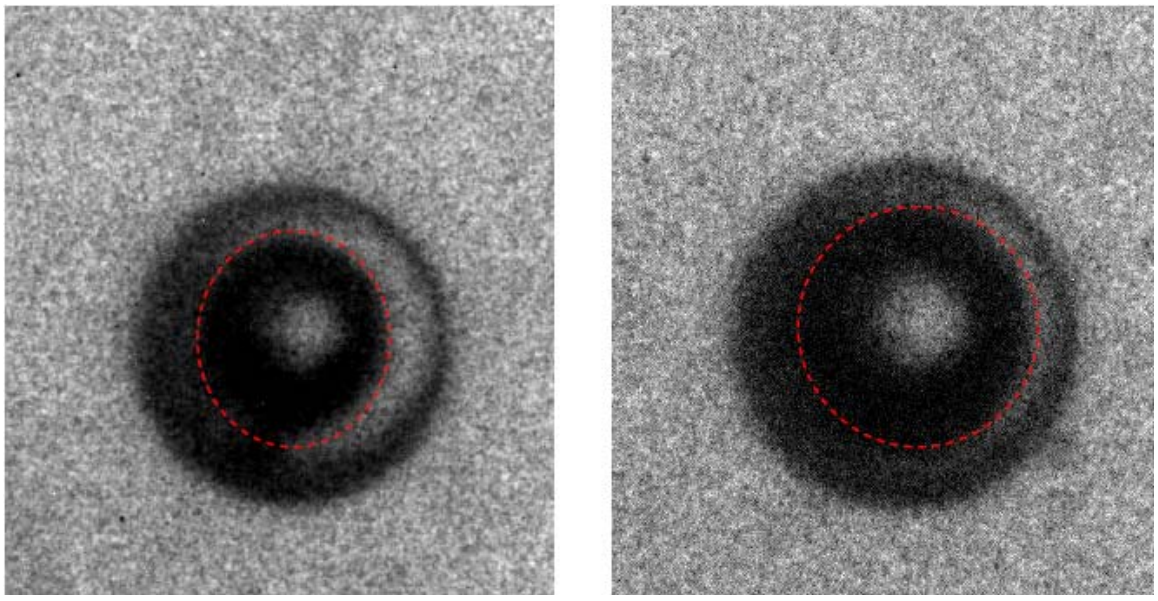

Figure 3.4: Snapshots of bubble evolution at 195 μs (left) and 975 μs (right). These snapshots were extracted from the 16-frame image set in Figure 3.5. Red dotted outline indicates the inner bubble.

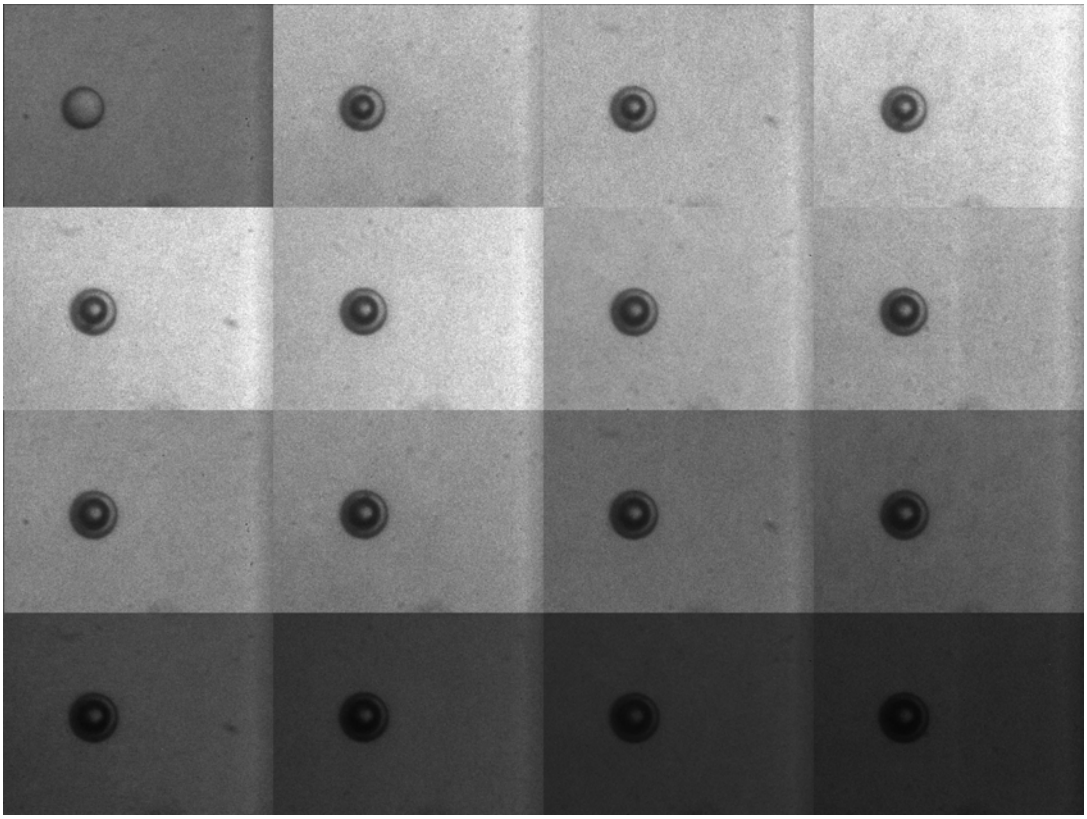

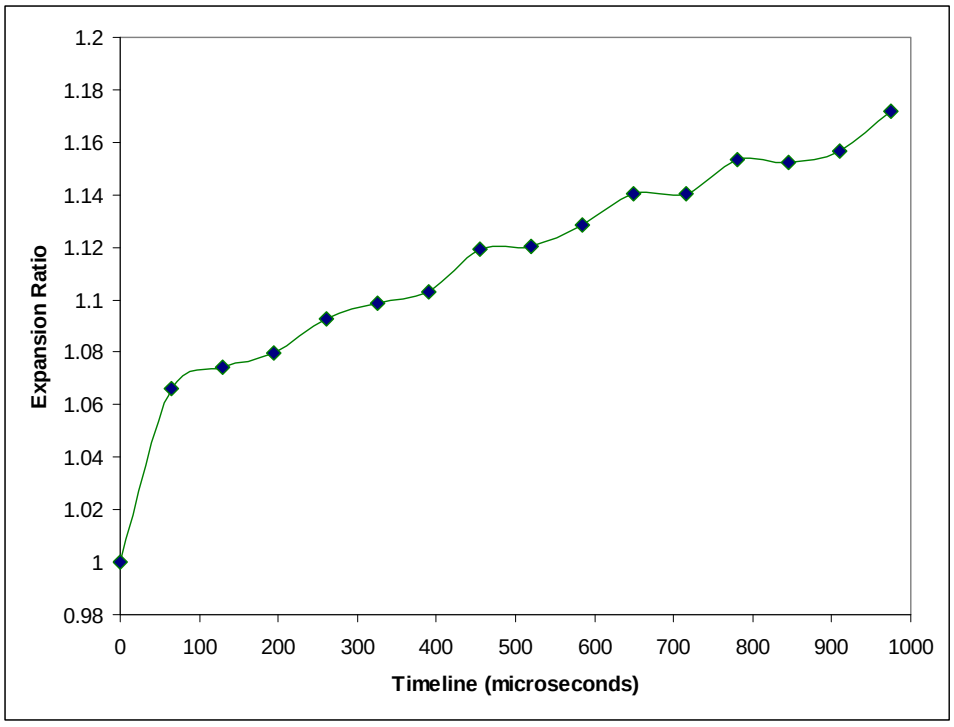

Figure 3.5: Evolution plot for a droplet of initial diameter 32 microns. Time line in microseconds: 0, 65, 130, 195, 260, 325, 390, 455, 520, 585, 650, 715, 780, 845, 910, 975.

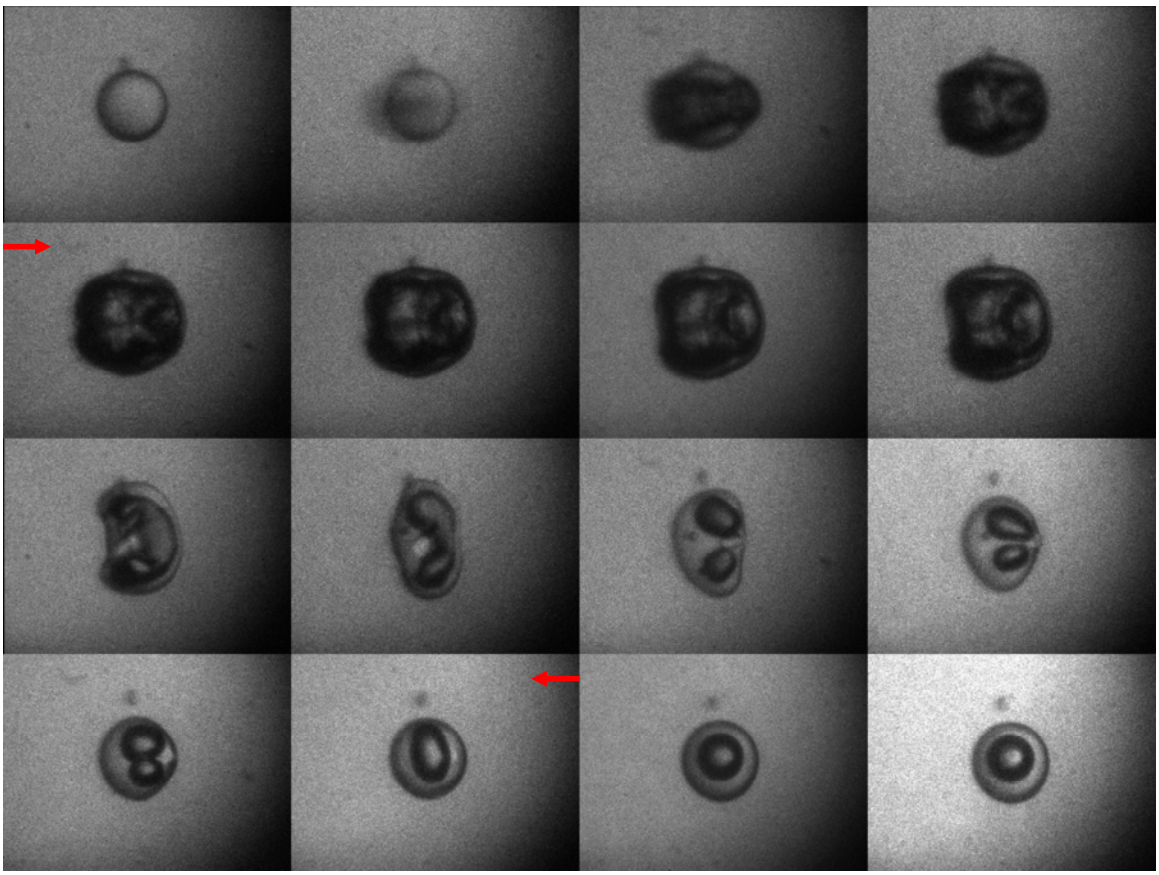

Figure 3.6: Internal details in an evolving bubble (initial diameter 49 μm) are shown clearly in frames 9 to 14. Timeline in microseconds: 0, 0.505, 1.01, 1.515, 2.02, 2.525, 3.03, 3.535, 7.04, 12.545, 20.05, 25.555, 35.06, 50.565, 87.07, 150.575. (red arrows are for comparison with Figure 3.7)

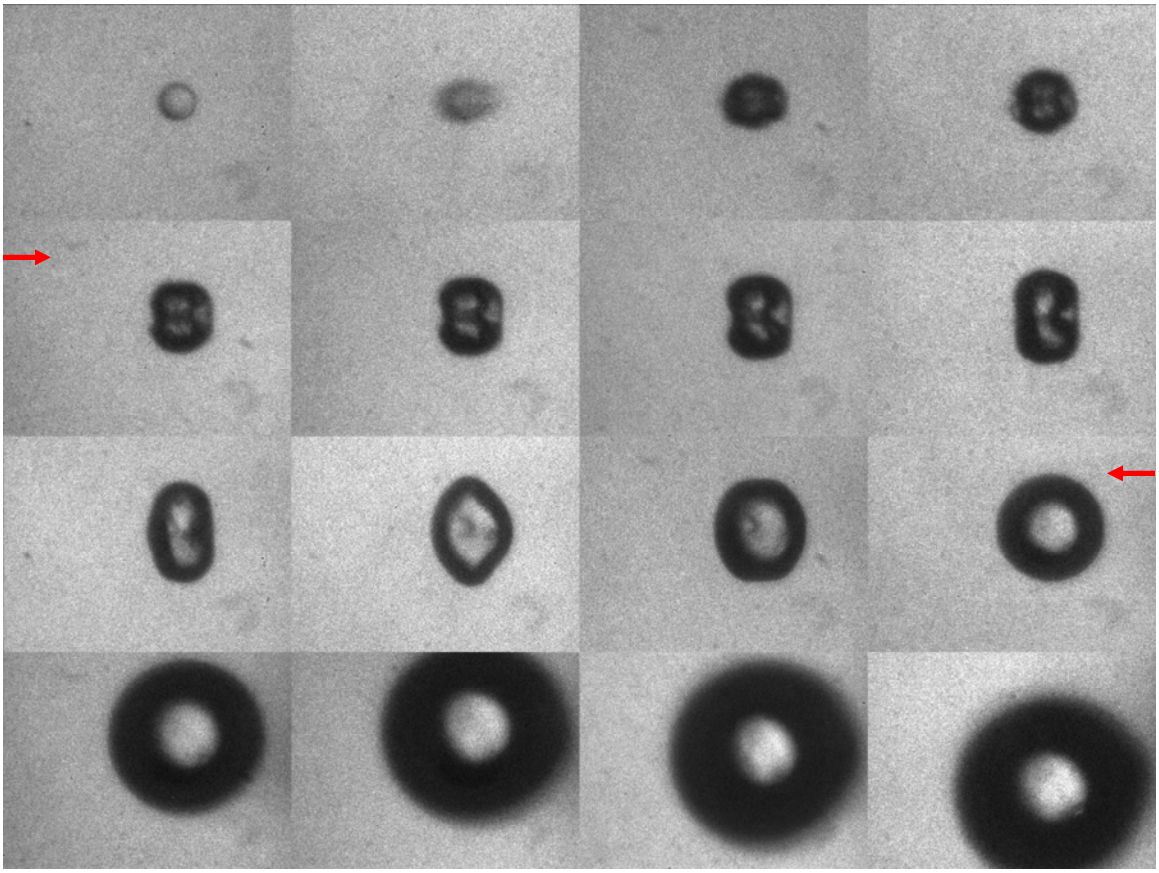

Figure 3.7: A physiological-temperature image set (initial droplet diameter of 27 μm) for comparison with Figure 3.6. Timeline in microseconds: 0, 0.5, 1, 1.5, 2, 2.5, 3, 4, 5, 7.5, 10, 15, 30, 60, 120, 300. (red arrows indicate time range roughly similar to the range in Figure 3.6)

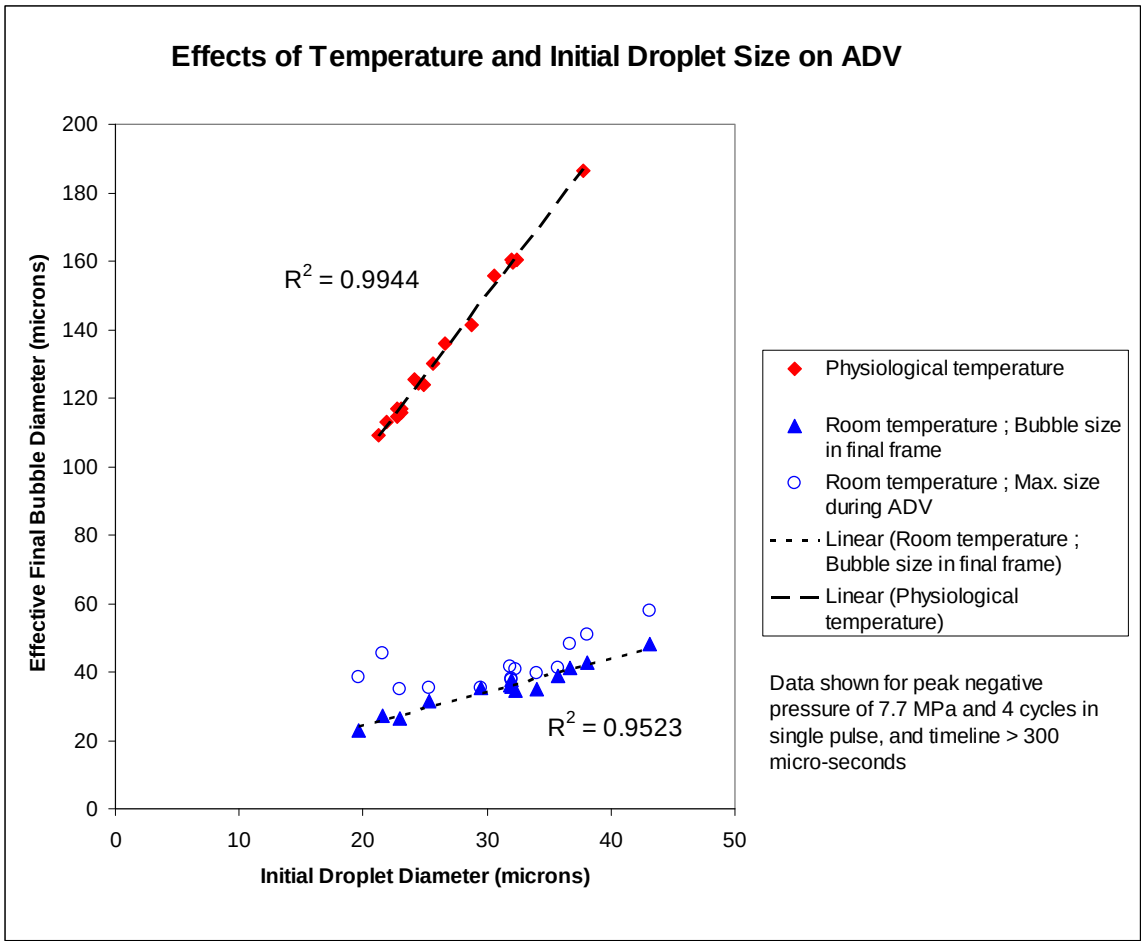

Figure 3.8: Comparison between room-temperature and physiological-temperature bubble evolution.

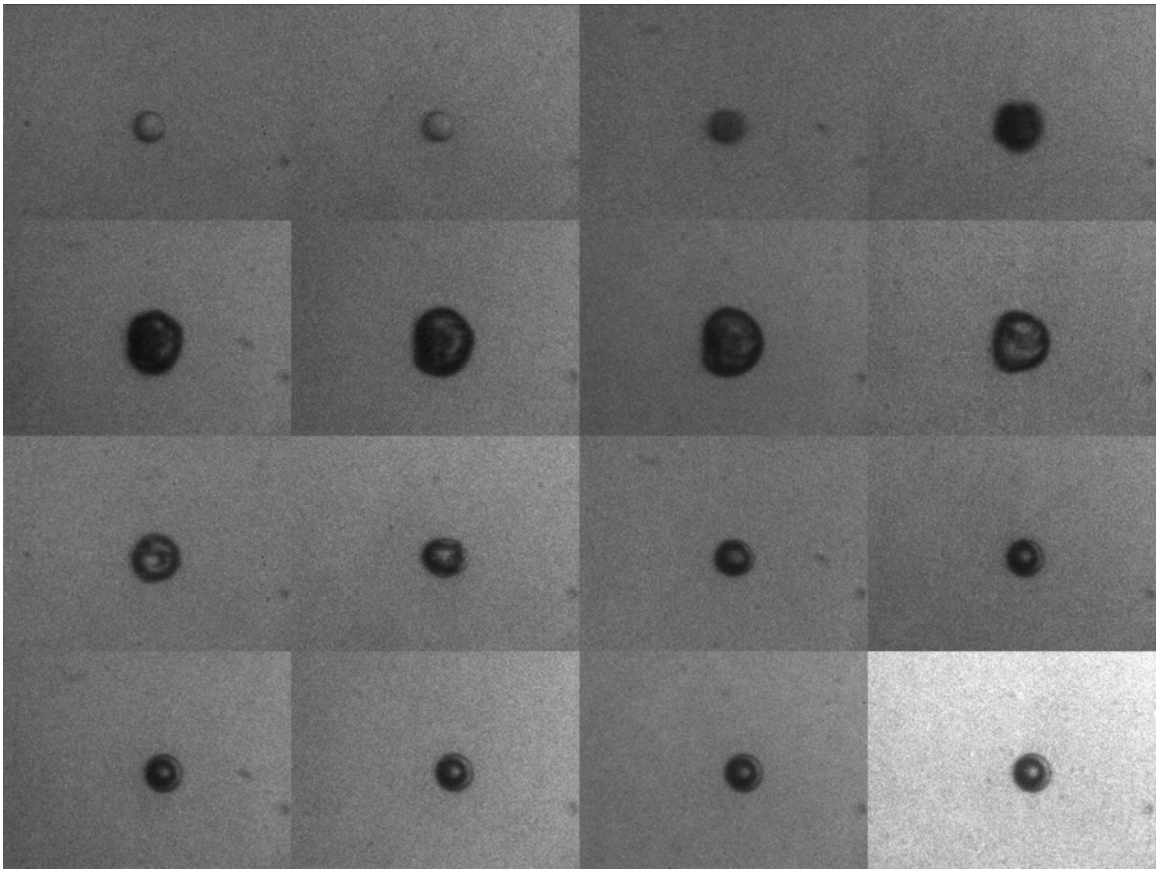

Figure 3.9: Bubble evolution of a droplet of initial diameter 22 μm at 73°F (23°C). Timeline in microseconds: 0, 0.5, 1, 1.5, 2, 2.5, 3, 4, 5, 7.5, 10, 15, 30, 60, 120, 300.

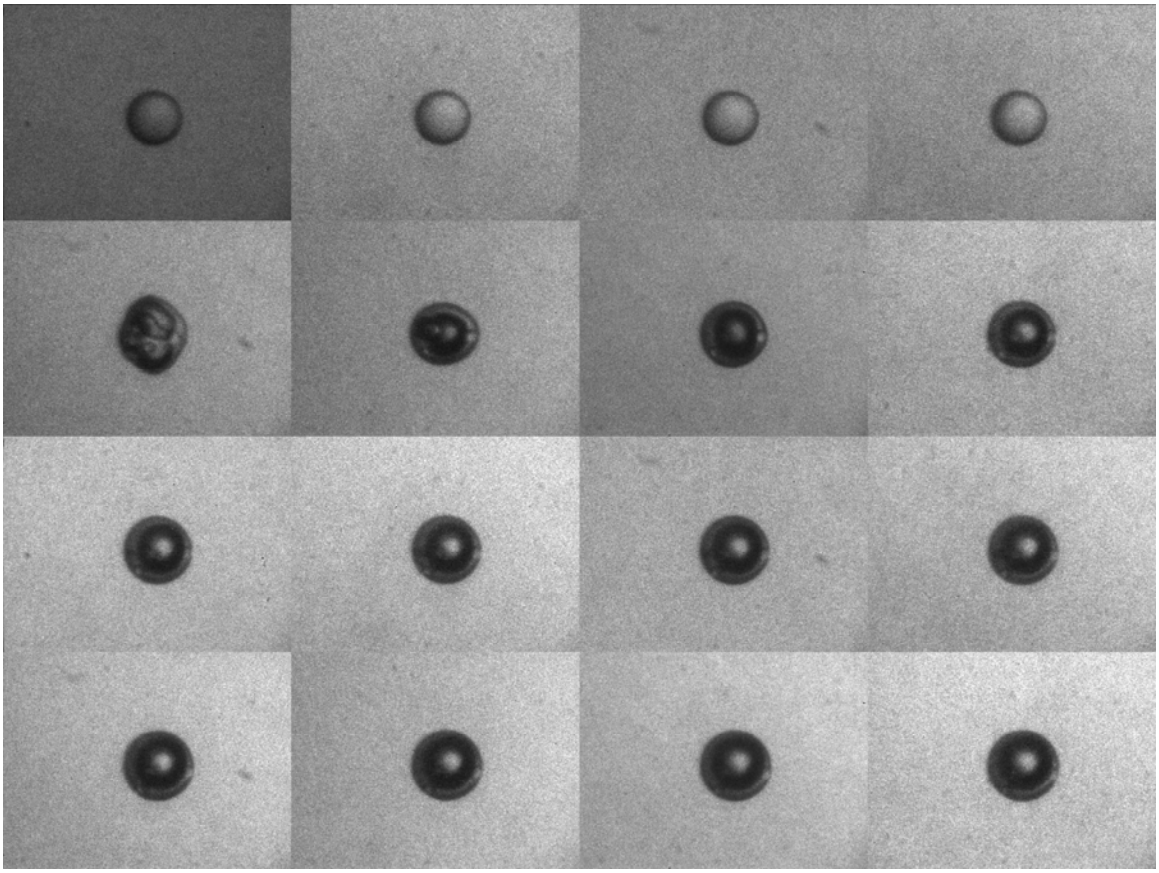

Figure 3.10: Bubble evolution of a droplet of initial diameter 37 μm at 82°F (28°C). Timeline in microseconds, starting from Frame 4: 0, 10.5, 21, 31.5, 42, 52.5, 63, 73.5, 84, 94.5, 105, 115.5, 126.

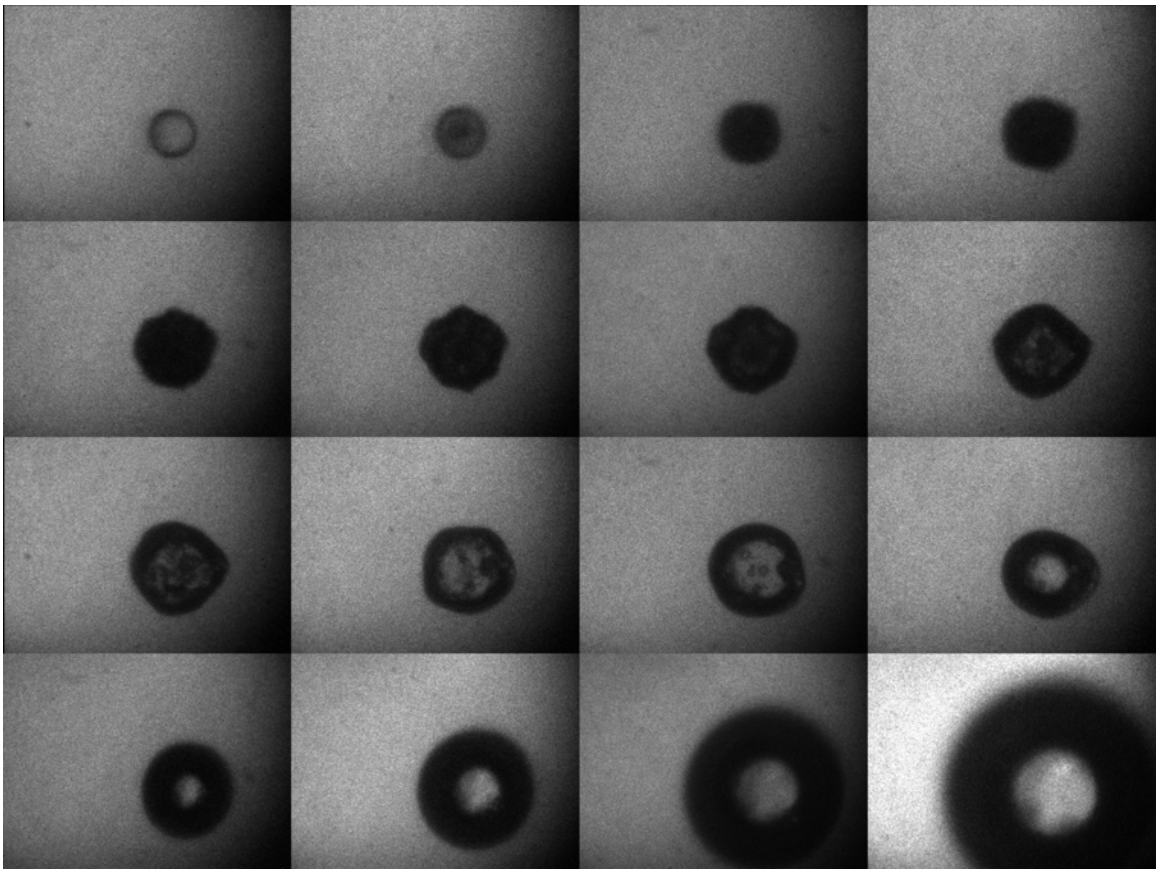

Figure 3.11: Bubble evolution of a droplet of initial diameter 33 μm at 88°F (31°C). Timeline in microseconds: 0, 0.5, 1, 1.5, 2, 2.5, 3, 4, 5, 7.5, 10, 15, 30, 60, 120, 300.

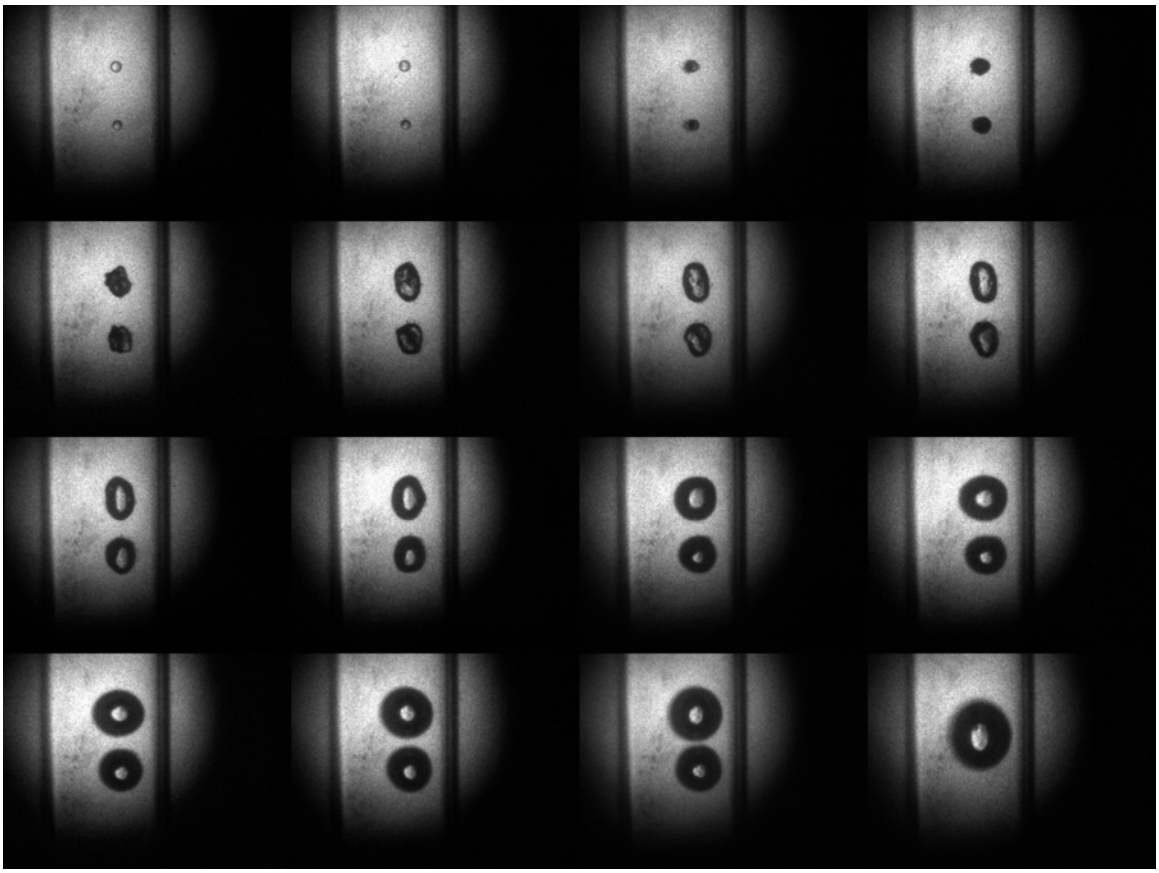

Figure 3.12: Coalescence of two bubbles under physiological temperature conditions. Timeline in microseconds: 0, 0.8, 1.2, 2, 4.5, 8, 10, 12, 15, 20, 30, 40, 50, 70, 100, 300.

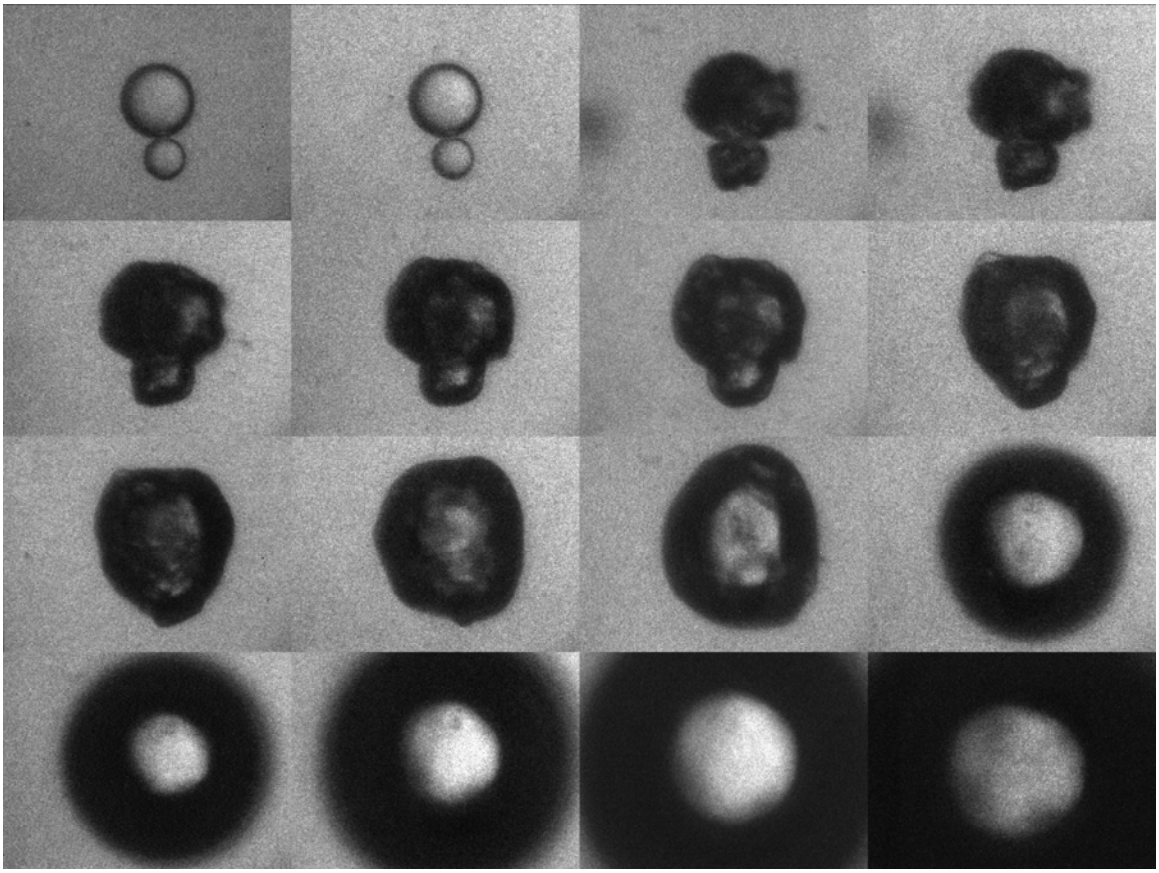

Figure 3.13: Coalescence of two droplets vaporizing in close proximity under physiological temperature conditions. Timeline in microseconds, starting from Frame 2: 0, 1.5, 2, 2.5, 3, 3.5, 4.5, 5.5, 8.5, 13.5, 28.5, 53.5, 103.5, 223.5, 573.5.

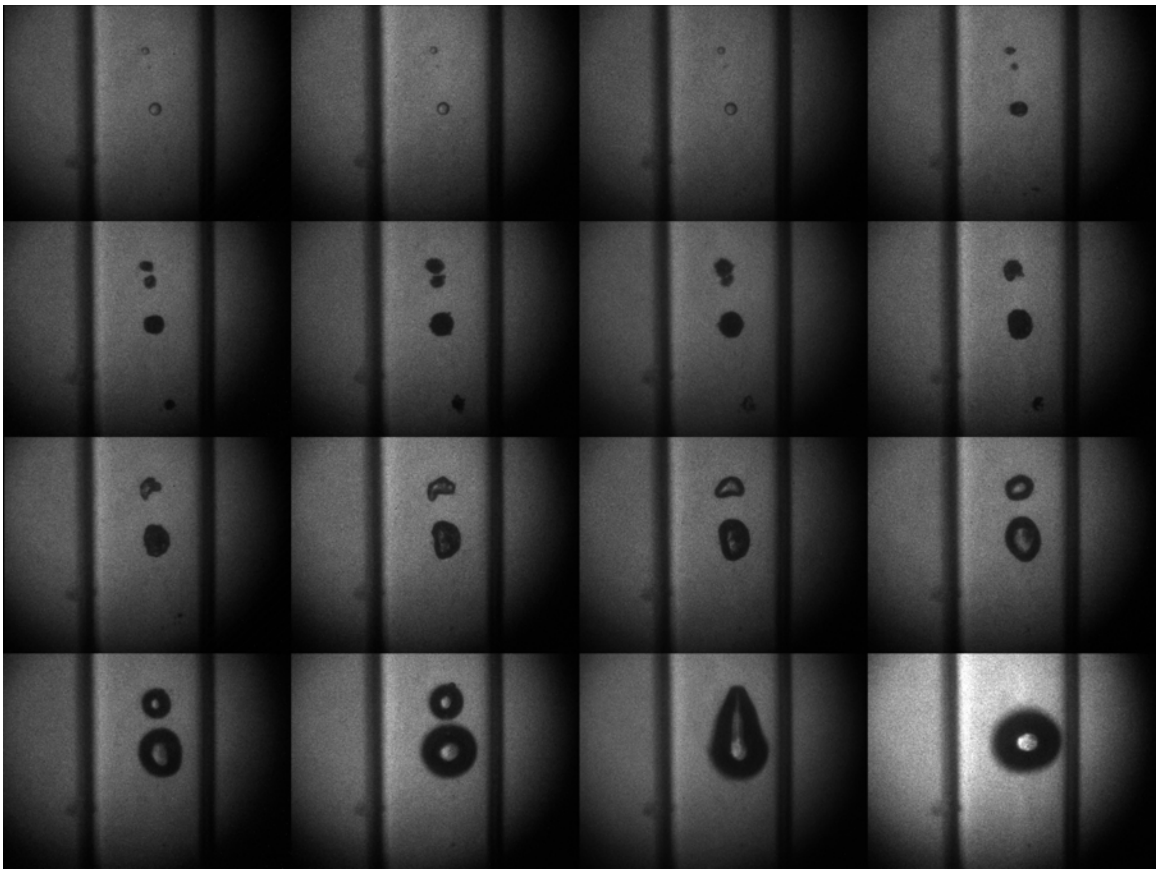

Figure 3.14: Coalescence of bubbles under physiological temperature conditions. Timeline in microseconds, starting from Frame 3: 0, 0.5, 1, 1.5, 2, 3, 4, 6.5, 9, 14, 29, 59, 119, 299.

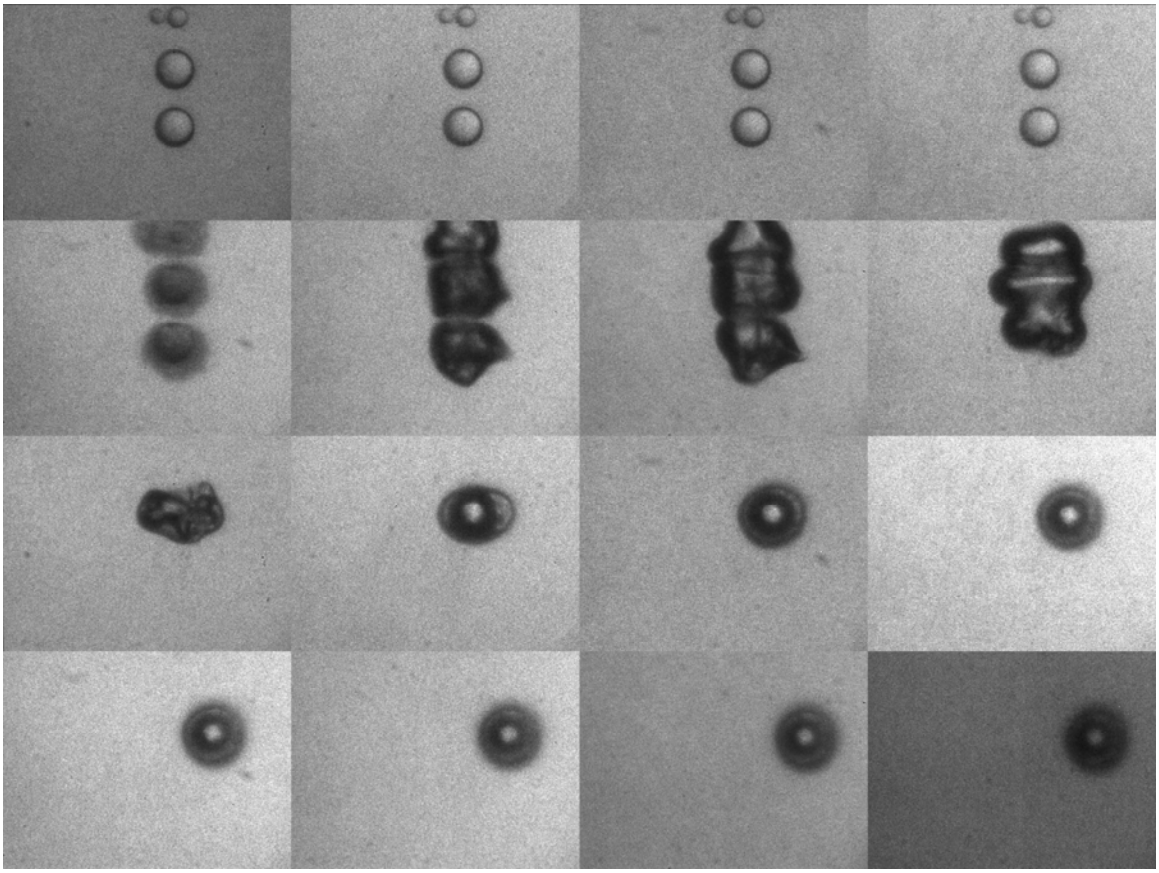

Figure 3.15: Coalescence of four vaporizing droplets under room temperature conditions. Timeline in microseconds, starting from Frame 4: 0, 1, 2, 3, 6, 11, 23, 43, 73, 123, 203, 403, 623.

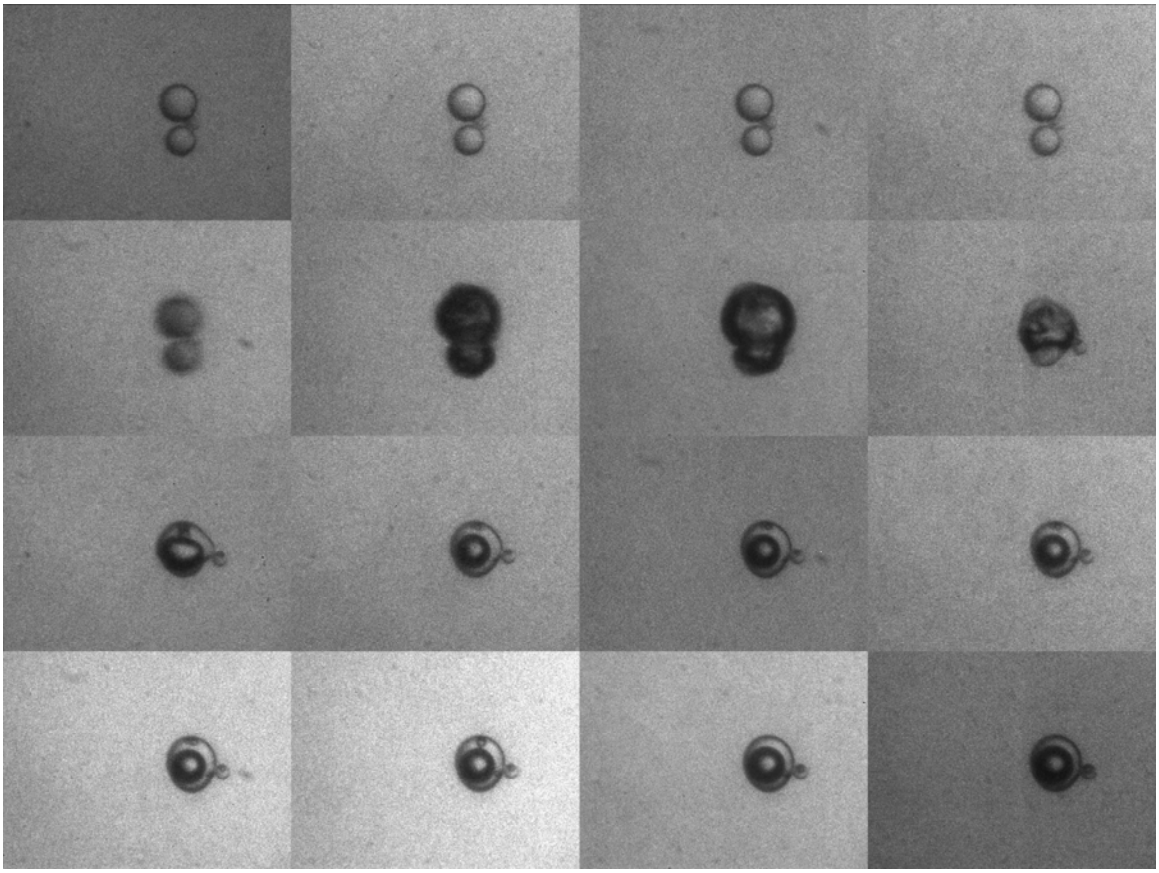

Figure 3.16: Coalescence of two droplets vaporizing in close proximity under room temperature conditions (note: the third and tiny droplet, barely visible, vaporized but did not coalesce). Timeline in microseconds, starting from Frame 4: 0, 1, 2, 3, 6, 11, 23, 43, 73, 123, 203, 403, 623.

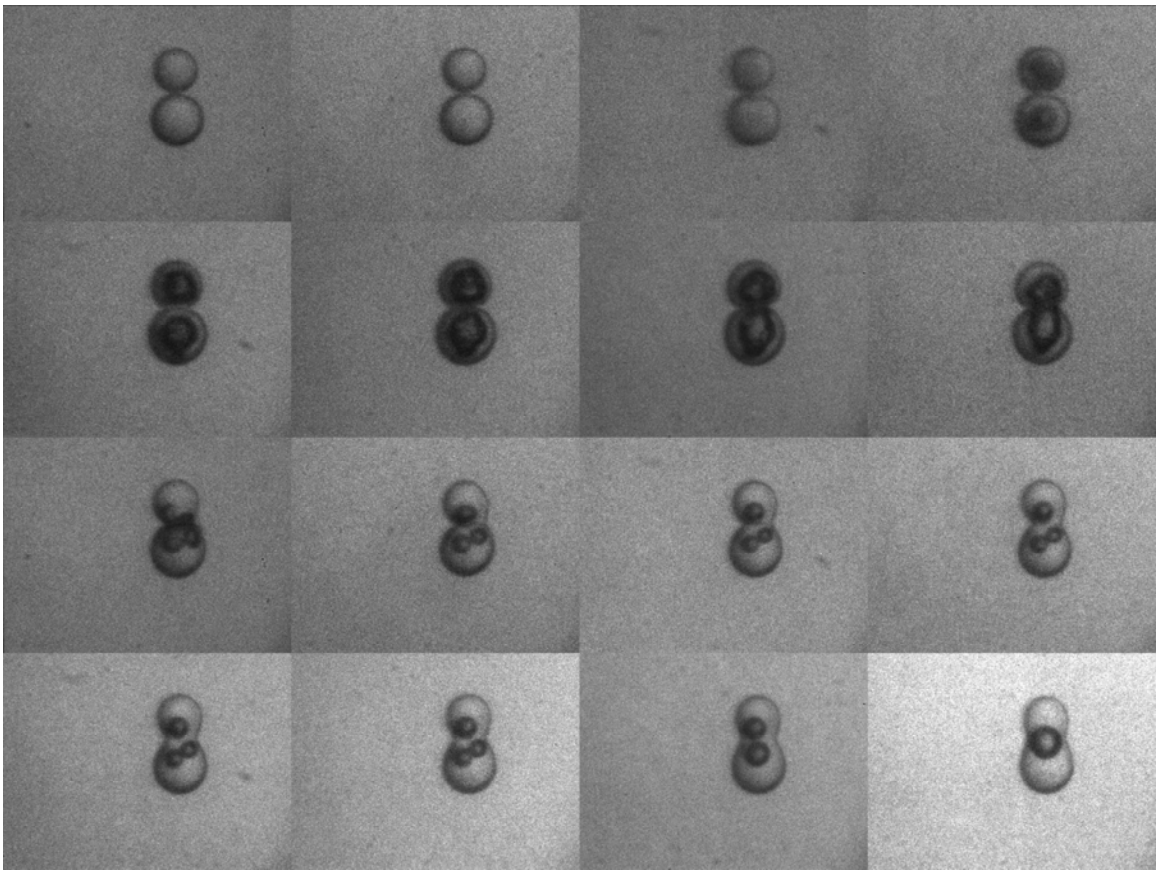

Figure 3.17: Coalescence of two droplets vaporizing in close proximity under room temperature conditions. Formation and subsequent coalescence of inner bubbles were also observed. Timeline in microseconds, starting from Frame 2: 0, 0.505, 1.01, 1.515, 2.02, 2.525, 3.03, 6.535, 12.04, 19.545, 25.05, 34.555, 50.06, 86.565, 150.07.

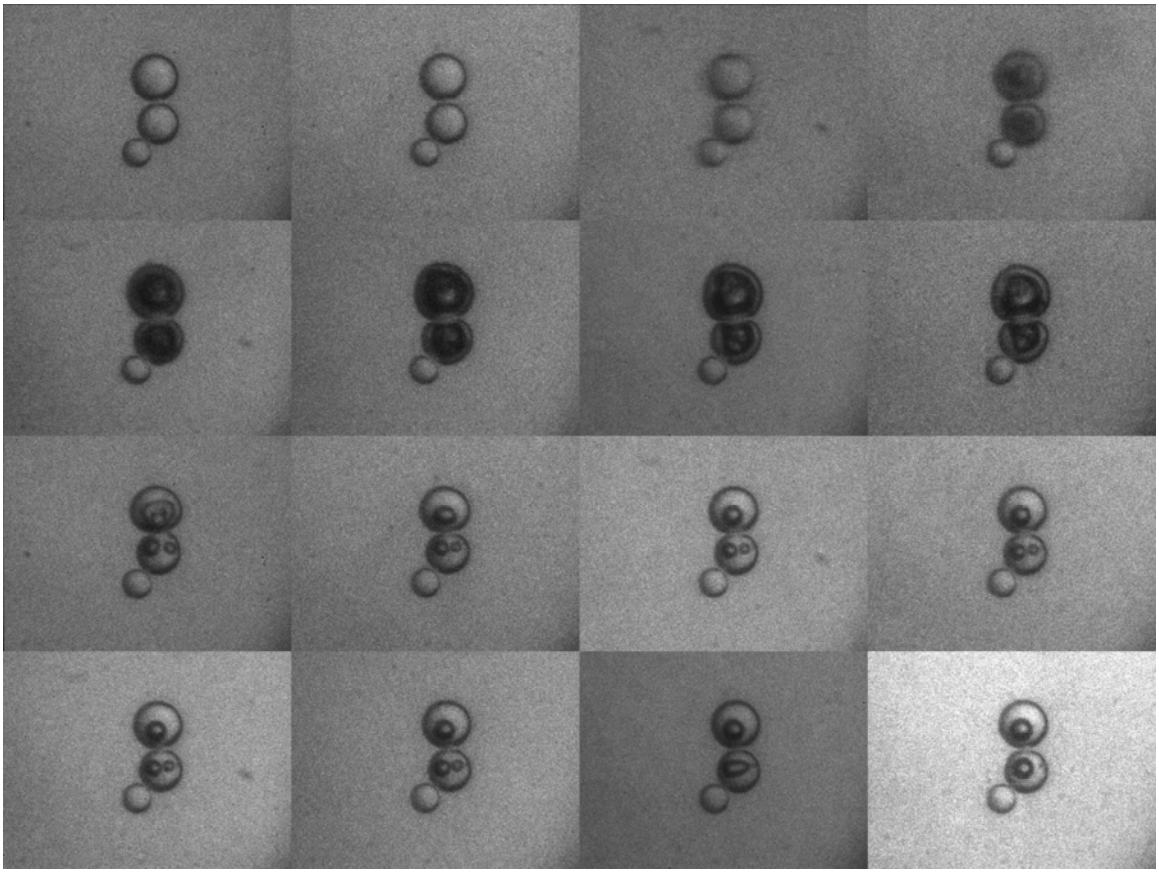

Figure 3.18: Coalescence of two vaporizing droplets in close proximity under room temperature conditions (note: the third and smaller droplet did not vaporize). Formation and subsequent coalescence of inner bubbles were also observed. Timeline in microseconds, starting from Frame 2: 0, 0.505, 1.01, 1.515, 2.02, 2.525, 3.03, 6.535, 12.04, 19.545, 25.05, 34.555, 50.06, 86.565, 150.07.

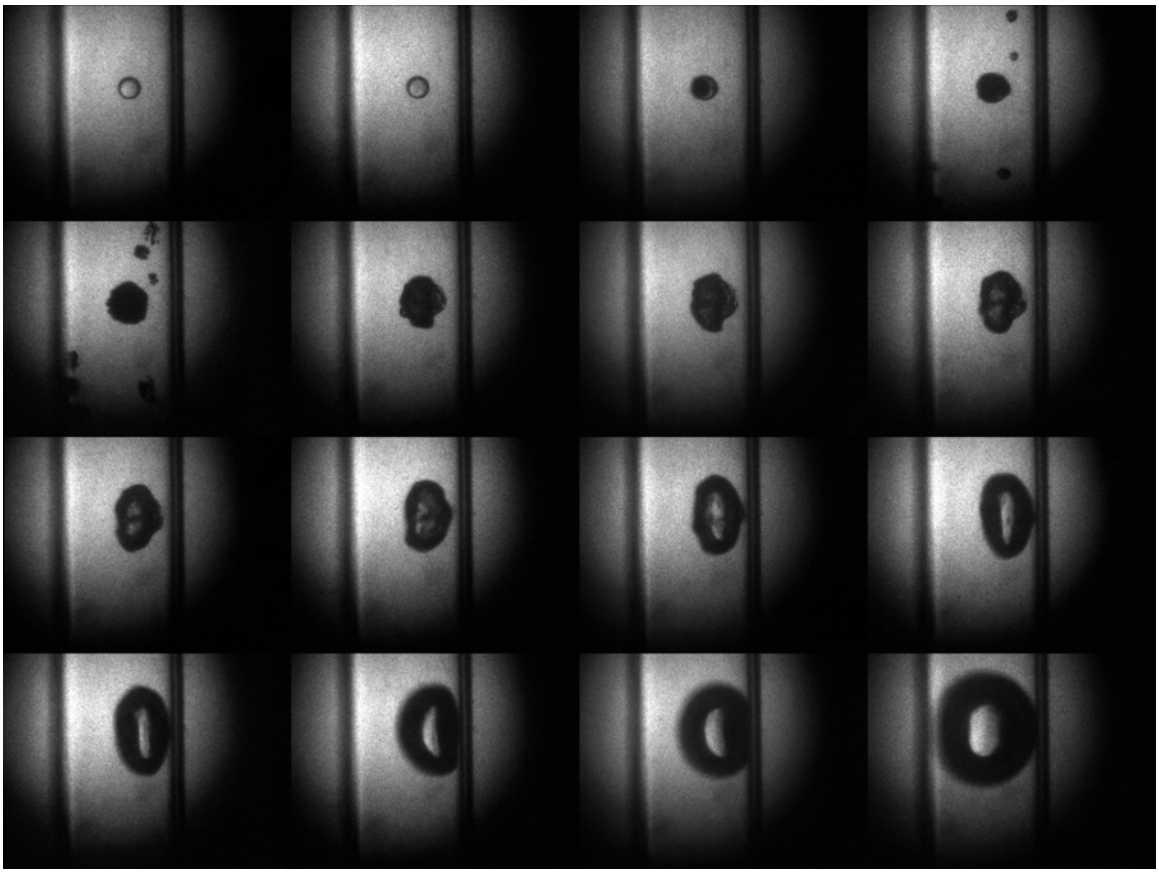

Figure 3.19: Expanding bubble made contact with one wall and eventually grew to contact both walls (physiological temperature experiment). Timeline in microseconds: 0, 0.8, 1.2, 2, 4.5, 8, 10, 12, 15, 20, 30, 40, 50, 70, 100, 300.

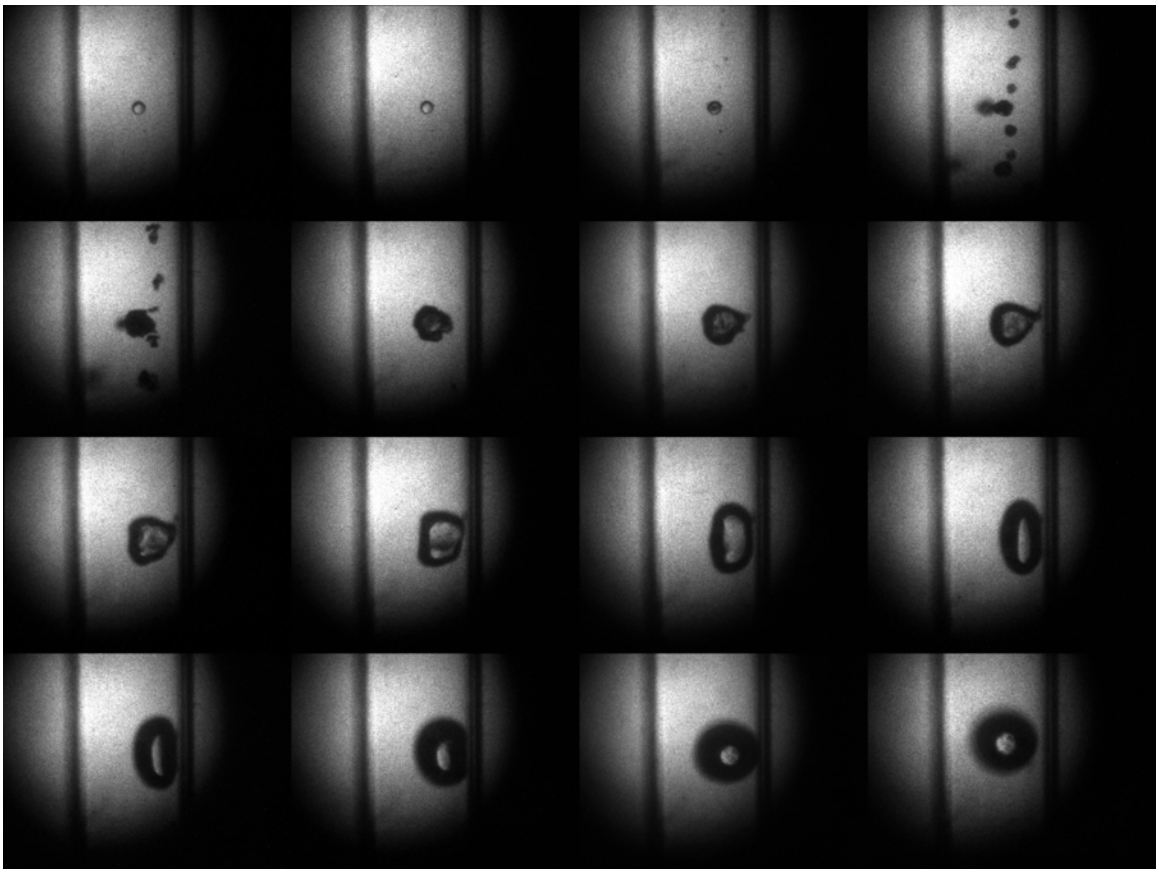

Figure 3.20: Expanding bubble made contact with wall, and rebounded off the wall (physiological temperature experiment). Timeline in microseconds: 0, 0.8, 1.2, 2, 4.5, 8, 10, 12, 15, 20, 30, 40, 50, 70, 100, 300.

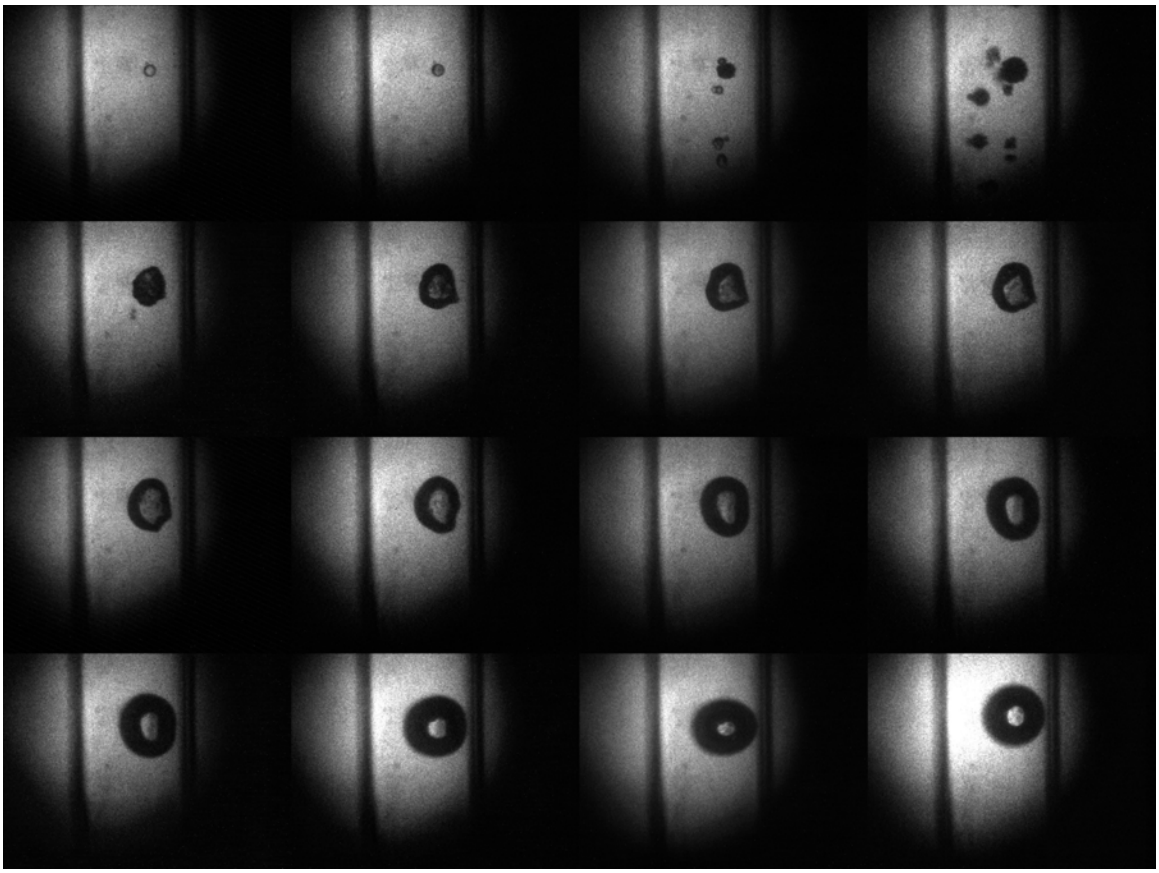

Figure 3.21: Similar to Figure 3.20, expanding bubble made contact with wall, and rebounded off the wall (physiological temperature experiment). Timeline in microseconds: 0, 0.8, 1.2, 2, 4.5, 8, 10, 12, 15, 20, 30, 40, 50, 70, 100, 300.

References

1. Haworth, K.J. and O.D. Kripfgans. *Initial growth and coalescence of acoustically vaporized perfluorocarbon microdroplets*. in *Ultrasonics Symposium, 2008. IUS 2008. IEEE*. 2008.

2. Kripfgans, O.D., et al., *On the acoustic vaporization of micrometer-sized droplets.* Journal Of The Acoustical Society Of America, 2004. **116**(1): p. 272-281.

Chapter 4

Benchtop Model of a Microvessel

4.1 Synopsis

This chapter will discuss the design of a circular-lumen microchannel fabricated via a non-lithographic method and the endothelialization of the microchannel for use as a benchtop microvascular model. The advantages and disadvantages of previous benchtop microvascular models will be discussed. The rationale behind the present design will be explained. The feasibility of this benchtop model will be demonstrated through a simple set of experiments. Potential applications for the benchtop model will be explored.

4.2 Previous Benchtop Microvascular Models

Previous microvessel models were often larger than micro-scale [20, 31] and lacked a physiologically representative circular lumen. Microvessel models using prefabricated glass capillary tubes [11] or polydimethylsiloxane (PDMS) microchannels fabricated via soft lithography [23, 24, 37] exhibited a

major geometrical difference from native vessels --- the lumen geometry. They had rectangular or trapezoidal cross-sections whereas the lumens of native vessels are circular. For bubble adhesion studies, a realistic channel cross-section is important because bubbles tend to stick in corners.

Other earlier microvessel models fabricated by coupling mirror halves of photoetched channels in flat glass surfaces had roughly circular lumens [10, 17]. However, coupling the mirror halves exactly to form a circle was rather tedious, and glass, being non-permeable to gases, was not the ideal material to facilitate gas exchange for cell culture. On the other hand, with PDMS being permeable to gases especially oxygen, non-permeable to water, non-toxic to cells and optically transparent, models fabricated from PDMS are better suited for endothelialization.

4.3 Materials and Methods

4.3.1 Method of Microchannel Fabrication

The key concept of our method is to utilize a wire of circular cross-section as a positive mold for the PDMS microchannel. If the wire is kept taut and straight while positioned in liquid PDMS during the curing of the PDMS, extracting the wire longitudinally from the cured PDMS leaves a straight microchannel in the material. The microchannel will have a circular lumen with a diameter equal to the external diameter of the wire.

A fabrication device consisting of two binding posts positioned at the same vertical level and facing each other on a platform was designed and machined (Figure 4.1). Each binding post contained a small hole through which a wire can be threaded. Turning the knobs of the binding posts with the wire threaded through the small holes pulled the wire taut and tightened it into a straight line. The overall footprint area of the platform was 22.5cm x 10cm, with the small holes of the binding posts positioned 20.5cm horizontally from each other and at a height of 3.75cm from the base of the platform.

Several cuboidal molds of varying dimensions (e.g. external 9cm x 2.5cm x 1.6cm, internal cavity 7cm x 1.3cm x 0.7cm) were machined from polyethylene and aluminium. The mold had a small hole drilled through each of its left and right walls, which allowed a suitably sized syringe needle to be inserted as a template for the inlet or outlet of the microchannel. The aluminium molds were polished with a super-fine grit polishing paste using a Dremel tool, so as to provide the smoothest surface and facilitate easy removal of the cured microchannel as well as improve optical transparency in the cured PDMS material.

Figure 4.1 shows the setup during fabrication of the microchannel, with the wire threaded and tightened between the binding post holes, syringe needles and the mold's wall holes before liquid PDMS was poured into the mold. Prior to threading the wire, if using the polyethylene mold, the mold's interior was covered with transparent tape (Scotch®, 3M, St. Paul, MN) which facilitated removal of the cured PDMS from the mold and maintained

optical transparency of the cured PDMS material (note: direct contact of the PDMS with the polyethylene would result in reduced optical transparency in the cured PDMS due to surface roughness of the mold). Using the polished aluminium mold might not require the usage of the transparent tape, provided that the aluminium surface was cleaned thoroughly with alcohol and allowed to dry beforehand.

The PDMS material was prepared from a Sylgard® 184 Elastomer two-part kit (Dow Corning, Midland, MI) using a base-to-curing-agent weight ratio of 10:1 and cured in a laboratory oven at 65°C for 4 hours. After the PDMS had cured completely, the wire outside of the mold was cut and extracted longitudinally, leaving a straight microchannel in the material. Provided that the extraction was performed slowly and with caution, the wire did not break during the process. The PDMS slab containing the microchannel was then removed from the mold, stripped of its transparent tape and ready to be used for microfluidics experiments or endothelialization.

To date, microchannels of diameter 80μm, 140μm and 330μm had been fabricated successfully via the above-mentioned method by using commercially available stainless steel wires (e.g. Malin Co., Brookpark, OH and Arcor Electronics, Northbrooko, IL) of the corresponding diameter. The smallest diameter available in the market is about 30 μm. Attempts to use the wire of 30 μm diameter for making the microchannel were unsuccessful, mainly because the friction between the wire and the cured PDMS was high enough to break the thin wire easily during its extraction.

4.3.2 Method of Endothelialization of Microchannel

The microchannels were endothelialized with human dermal microvascular endothelial cells (Cambrex, Walkersville, MD). In preparation for endothelialization, a leak-proof microfluidic system was set up by connecting suitably sized inlet and outlet syringe needles (between Gauge 20 and 26, McMaster-Carr, Santa Fe Springs, CA, USA) and Tygon PVC tubings to the PDMS microchannel.

Fibronectin (Sigma Aldrich, St Louis, MO) at a concentration of 50μg/mL was used to pre-coat the microchannel overnight in a 37°C, 5% CO_2 incubator. The surface of the microchannel could be plasma-oxidized with oxygen plasma for 20 minutes to reduce its hydrophobicity but no significant difference in cell adhesion was observed between oxidized and non-oxidized microchannels, as long as fibronectin was used.

Prior to seeding of the cells, the fibronectin was replaced by EGM-MV cell medium (Cambrex, Walkersville, MD). Endothelial cells between passage 3 and 11 were used to seed the microchannel at a density greater than 10^5 /cm^2. The seeded microchannel was left stationary in a level position for 3-6 hours in the incubator. When the cells had attached to the microchannel walls, their morphology as observed under a microscope (Nikon TE2000-S, Japan) changed from round to elongated. The endothelialized microchannel was sustained within a 37°C, 5% CO_2 incubator by infusion with cell medium via a syringe pump (KD Scientific, Holliston, MA) at a rate of 0.1 to 0.15 mL/h.

4.3.3 Cell-Viability Assay

Viability of the endothelialized microchannel was assessed with a LIVE/DEAD® Viability / Cytotoxicity Assay Kit (Invitrogen Molecular Probes, Carlsbad, CA). Dye concentrations of 4 μM for both calcein AM and ethidium homodimer-1 (EthD-1), and a dye-incubation time of 20 minutes were used for the assay. An inverted microscope (TE2000-S, Nikon, Tokyo, Japan) with a CCD camera (CoolSNAP ES, Photometrics, AZ) and imaging software (MetaMorph, Molecular Devices, Sunnyvale, CA) were used for the imaging.

Calcein AM (non-fluorescent and membrane-permeant) was actively taken up by viable cells and converted into calcein (a fluorophore and relatively membrane-impermeant), which rendered viable cells green under fluorescence microscopy. On the other hand, EthD-1 only accumulated in dead cells which would appear red.

4.3.4 Bubble Motion Experiments in the Microvascular Model

To demonstrate the feasibility of our microvascular model, an experiment to investigate the effect of bubble motion on cell viability was conducted.

Two endothelialized 80-μm diameter microchannels were prepared and maintained for two days in the incubator before the experiment. Before the experiment, the microchannels were examined quickly under brightfield

microscopy to confirm that most of the microchannel length was confluent with endothelial cells.

As sketched in Figure 4.2, the flow system consisted of the microchannel inlet linked to a T-connector whose two ports were connected respectively to a syringe pump (for moving cell culture medium or bubble into microchannel) and an empty, 10μL micro-bore glass syringe (Hamilton Gastight, Reno, USA) (for creating small gas bubbles), and the microchannel outlet connected to a waste container.

The endothelialized microchannel was kept in the incubator until right before the experiment. The experiment was conducted at room temperature within the tissue culture room which tended to be warmer than the regular laboratory space. Given that the experiments did not take long, the room temperature should not have affected the endothelial cells' viability.

A small bubble of about 10 μL was injected into the T-connector and moved along the tubing into the microchannel by operating the syringe pump. One of the endothelialized microchannel had a bubble moving through it at a volumetric infusion rate of 0.2 mL/h while the other had a bubble moving at 2 mL/h. The viability of the cells in the microchannels was assessed immediately after each experiment.

The shear stress at the wall due to the bubble motion was estimated by using a liquid film thickness predicted by Bretherton [5] and assuming a linear velocity profile from the bubble surface to the wall. Bretherton's analysis showed that $W = \frac{b}{r} = 1.29\left(3\frac{\mu U}{\sigma}\right)^{2/3}$ where b is the film thickness, r

the microchannel radius, μ the viscosity of water, σ the surface tension of water and air, and U the bubble speed. Assuming that the bubble speed U was equal to the average flow velocity, the shear stress was estimated from

$\tau_w = \mu \frac{U}{b} = \frac{(\mu U)^{1/3}}{1.29r} \cdot \left(\frac{\sigma}{3}\right)^{2/3}$, with μ=0.69 mPa.s, σ=72 mN/m, and r=40 μm.

For 0.2 mL/h infusion rate, the shear stress was estimated as 745 dynes/cm^2 and for 2 mL/h infusion rate, the shear stress was estimated as 1605 dynes/cm^2.

4.4 Results and Discussion

4.4.1 PDMS Microchannel

As shown in Figure 4.3, the microchannels were straight and clear, and had circular lumens. The 80μm microchannel (photos b and c in Figure 4.3) was at a scale comparable to that of a large arteriole. The smallest commercially available diameter of wire is around 30μm, which is comparable to the scale of a small arteriole.

Besides the advantage of producing a circular lumen, our fabrication method is elegantly simple, low in cost and enables fast and reproducible production of microchannels. For example, it does not require accurate coupling of two mirror halves of a microchannel as required by the lithographic methods. The lumen of our microchannel is integral with the

surrounding material, which eliminates any risk of leakage arising from incomplete sealing between two halves.

4.4.2 Endothelialized Microchannel

It was observed that the endothelial cells attached well to the microchannel wall after being seeded and left stationary for several hours, resulting in extensive endothelialization of the microchannel, as shown in Figure 4.4. The endothelialization was fairly homogeneous along the length of the microchannel, as shown in Figure 4.5.

Although the endothelialization was not apparent in the bright-field microscopic images (labeled "c" in Figure 4.4) of the microchannel two days after the initial seeding, the endothelialization was visualized and confirmed by utilizing fluorescent microscopy. At the end of the period of maintenance (ranging from two to four days), viability of the endothelialized microchannel was assessed.

As shown in Figure 4.6, the endothelialized microchannel exhibited a very high degree of viability, with more than 90% of the cells displaying green fluorescence. Figure 4.7 shows a different but less successful endothelialization attempt (note: the layers of red and green images were superimposed in Adobe Photoshop), in which the cell seeding density and syringe pump infusion rate had not been optimized yet, resulting in a lower degree of cell viability (about 50%).

As a result of the high gas permeability of PDMS, the cells were able to derive sufficient oxygen from the interior atmosphere of the incubator despite growing at a high packing density within the microchannel. If glass which is not gas-permeable were to be used in our microvessel model, the design of our setup will become more complicated due to the need for additional oxygenation of the cell medium. In our present work, culturing of cells within endothelialized microchannels had been continued for up to four days. If so desired, we expect that viability can be sustained for a longer period of time, as demonstrated by [37].

Fully cured PDMS with 10:1 base/curing agent ratio has an elastic modulus of 1.783 MPa, as determined by tensile tests [6], while the elastic modulus of silica glass is about 73 GPa. The mean elastic modulus E of native microvessels (arteries, arterioles, veins, venules, capillaries) spans a wide range from 0.1 to 2 MPa. For example, the carotid artery has $E=0.396\pm0.101$ MPa [1]; the radial artery has $E=2.68\pm1.81$ MPa [26] and the iliofemoral artery / vein has $E=1.54\pm0.33$ / 3.11 ± 0.65 MPa [33]. Therefore, compared to glass microchannels, our microvessel model is much more physiologically representative of native microvessels.

By virtue of their lack of smooth muscle and their embedment in surrounding tissue ("tunnel-in-gel concept" [18]), capillaries are stiffer than arterioles. Given that PDMS is a flexible material, our microvessel model can be tailored to match the stiffness of arterioles or capillaries by varying PDMS processing conditions (i.e. time and temperature of curing, ratio of base to curing agent).

4.4.3 Cell Viability in Bubble Motion Experiments

Under a high shear stress (caused by bubble motion at 2 mL/h), about 75% of cells were detached. About 50% of the remaining cells were tested to be non-viable. An example of the cell-viability test is shown in Figure 4.8.

Under a low shear stress (caused by bubble motion at 0.2 mL/h), more cells remained attached, and the cell-viability test showed that overall, about 42% of the undetached cells were non-viable. An example of the cell-viability test is shown in Figure 4.9.

Figure 4.9 shows the results of cell viability along different sections of the microchannel length, for the experiment involving the low shear stress (note: due to the small number of cells remaining in the experiment involving the high shear stress, it was not possible to have a meaningful count of the viable/non-viable cells along the microchannel).

The shear stresses resulting from the two infusion rates were both much higher than the normal physiological levels (up to 20-30 dyne.cm^{-2}) of shear stresses experienced by endothelial cells. This was why in one case the cells were detached from the walls and in the other case there was extensive injury to the cells.

Although the experimental results were rather inconclusive, the following outcomes were achieved:

(i) The feasibility of the endothelialized microchannel as a benchtop microvascular model was demonstrated.

(ii) The results suggested that bubble motion of a sufficiently high speed could induce a high shear stress to detach the endothelial cells from the walls of the microchannel.

(iii) The shear stress from the bubble motion, probably highest at the front of the bubble, could also damage undetached cells along the microchannel.

4.4.4 Potential Applications of Benchtop Model

Notwithstanding the simple geometric configuration of a straight microchannel used in our microvessel model, a quick survey of research literature has suggested many areas of experimental work where our model can potentially find application :-

(i) microfluidics, biorheology and hemodynamics research, such as velocity and viscosity profiles near the endothelial surface layer or glycocalyx [13, 39], velocity, pressure and shear stress measurements in microchannels [3, 12, 25, 28, 50], cell partitioning in two-phase flow [48], red blood cell deformation [36, 43];

(ii) endothelium function and growth [15, 16, 19, 30, 35, 44];

(iii) cell adhesion and migration, and interaction studies involving leucocytes and platelets [8, 21, 22, 29, 34, 40, 41, 49];

(iv) biomedical ultrasound experiments such as acoustic vaporization in microvessels, ultrasound flow studies using contrast agents and tissue phantoms, ultrasound-microbubble-cell interactions, and experimental

comparison with numerically predicted dynamics of cavitation microjets near a rigid boundary [2, 4, 7, 9, 31, 42, 45, 46];

(v) investigating vascular effects of targeted drug delivery via microbubbles [14, 32, 38] and developing diagnostic methods based on targeted bubble adhesion [27, 47].

4.5 Concluding Remarks

In conclusion, we have demonstrated a novel non-lithographic method of fabricating a PDMS microchannel with a circular lumen, which can be endothelialized to produce a model of a microvessel. This method provides advantages in physiological relevance (circular lumen and biologically relevant mechanical properties such as elastic modulus and density), simple fabrication (short time required for preparation and processing, no requirement for accurate assembling of two microchannel halves nor clean-room facilities), low cost, as well as reliable consistency and high reproducibility.

These advantages are in addition to the well-documented merits of PDMS: optical transparency, non-toxicity, and permeability to gases, especially oxygen, but not to water. Our method may not be well suited for fabricating complex microvessel geometry but it might be possible to fabricate simple bifurcating microvessel models, which can be a topic for future research. In its present form, our benchtop microvascular model was demonstrated to be feasible for simple experiments, and it can find

application potentially in many areas of experimental research. In our own laboratory, it will be useful for investigating bubble interactions with the endothelium, as part of our ongoing research in gas embolotherapy.

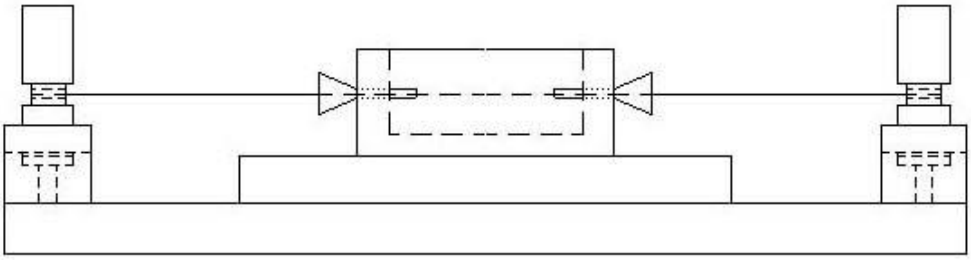

Figure 4.1: Device for fabricating PDMS microchannel of a circular lumen.

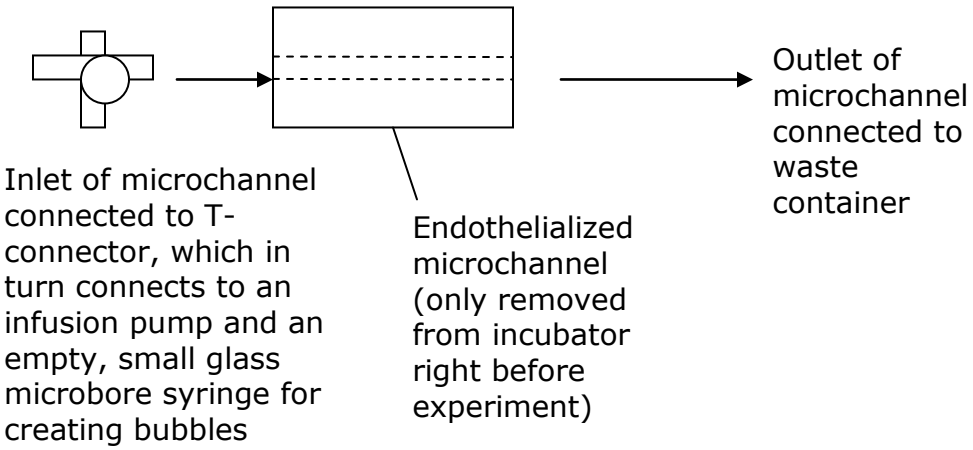

Figure 4.2: Illustration of experimental setup for bubble motion experiment

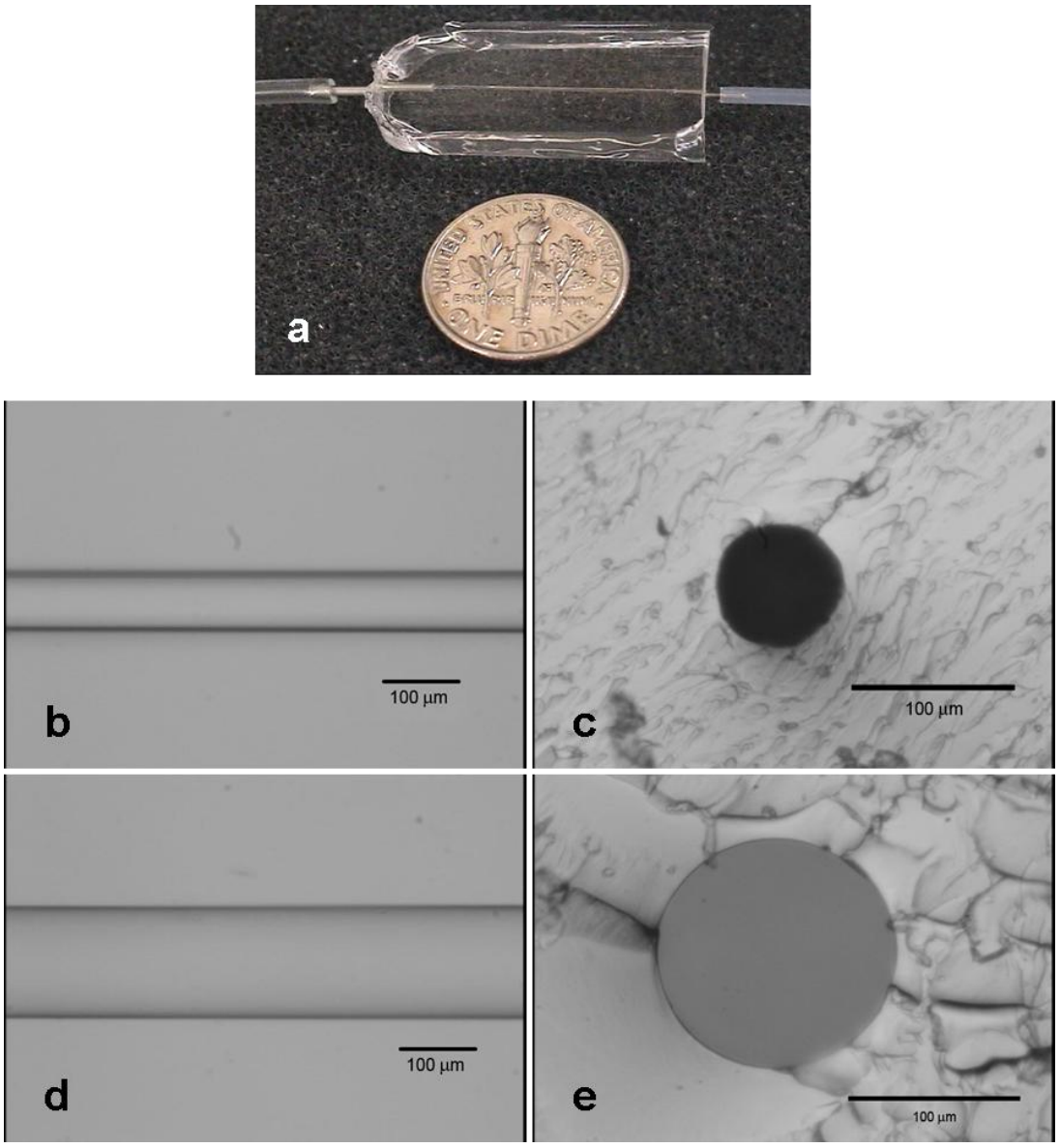

Figure 4.3: Images of microchannels and their circular cross-sections.

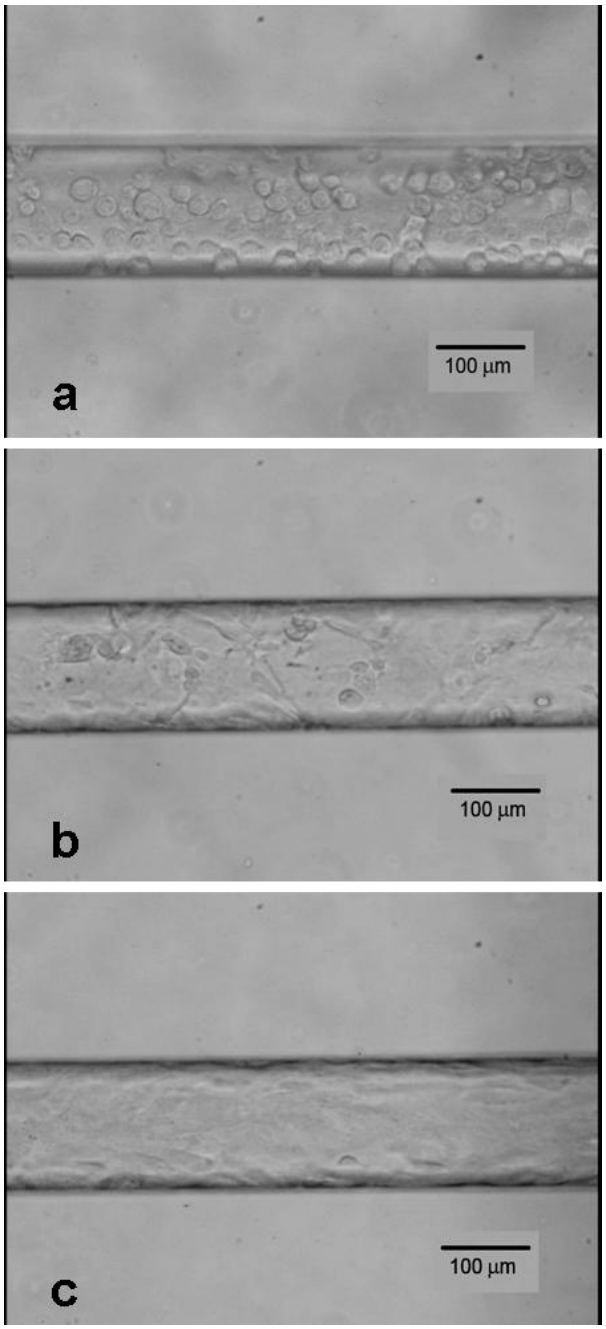

Figure 4.4: Images showing progress of endothelialization at (a) seeding, (b) 5 hours after seeding, (c) 2 days after seeding

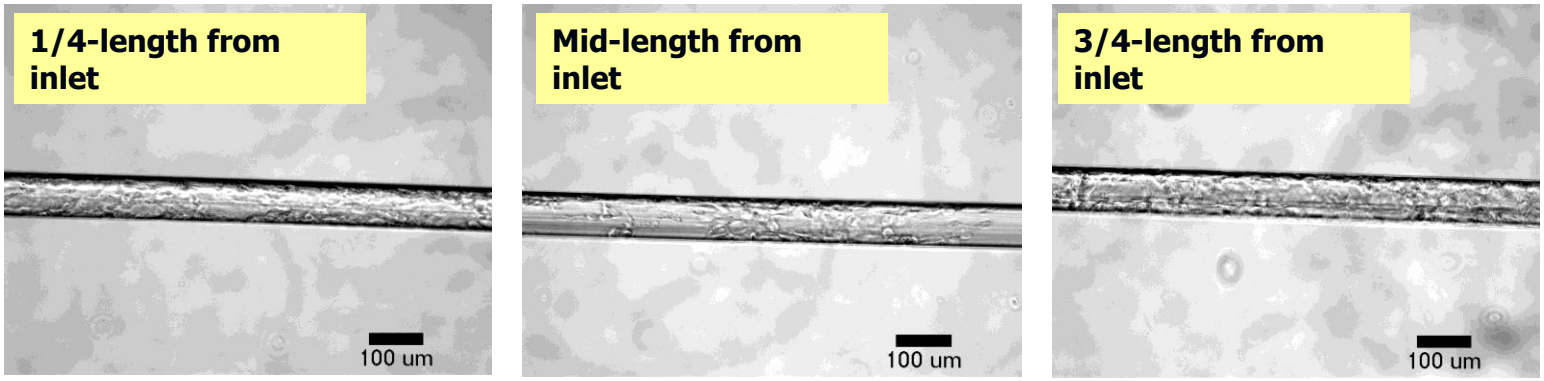

Figure 4.5: Endothelialization was fairly homogeneous along the microchannel length.

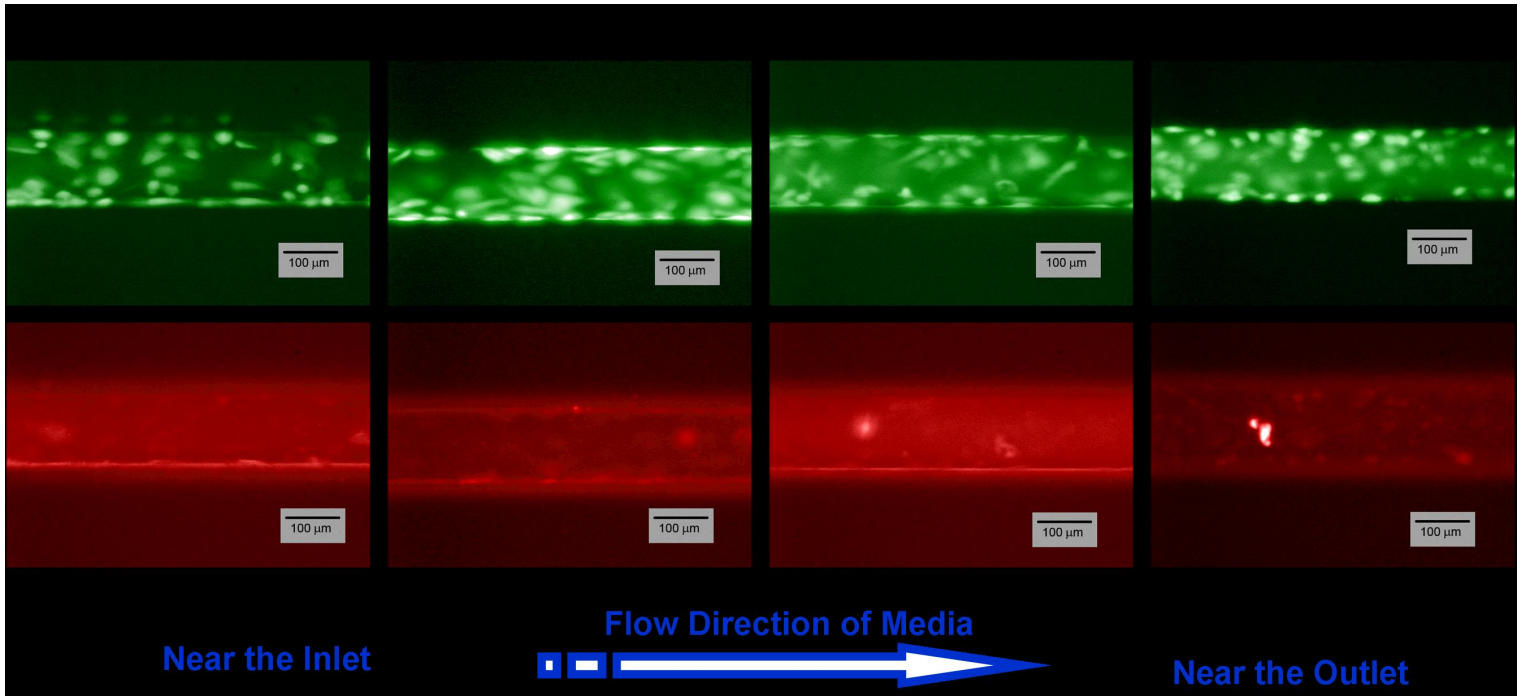

Figure 4.6: Assessment of viability of endothelialized microchannel at 4 different sections using fluorescent microscopy. (top and bottom images in each column correspond to the same section of the microchannel)

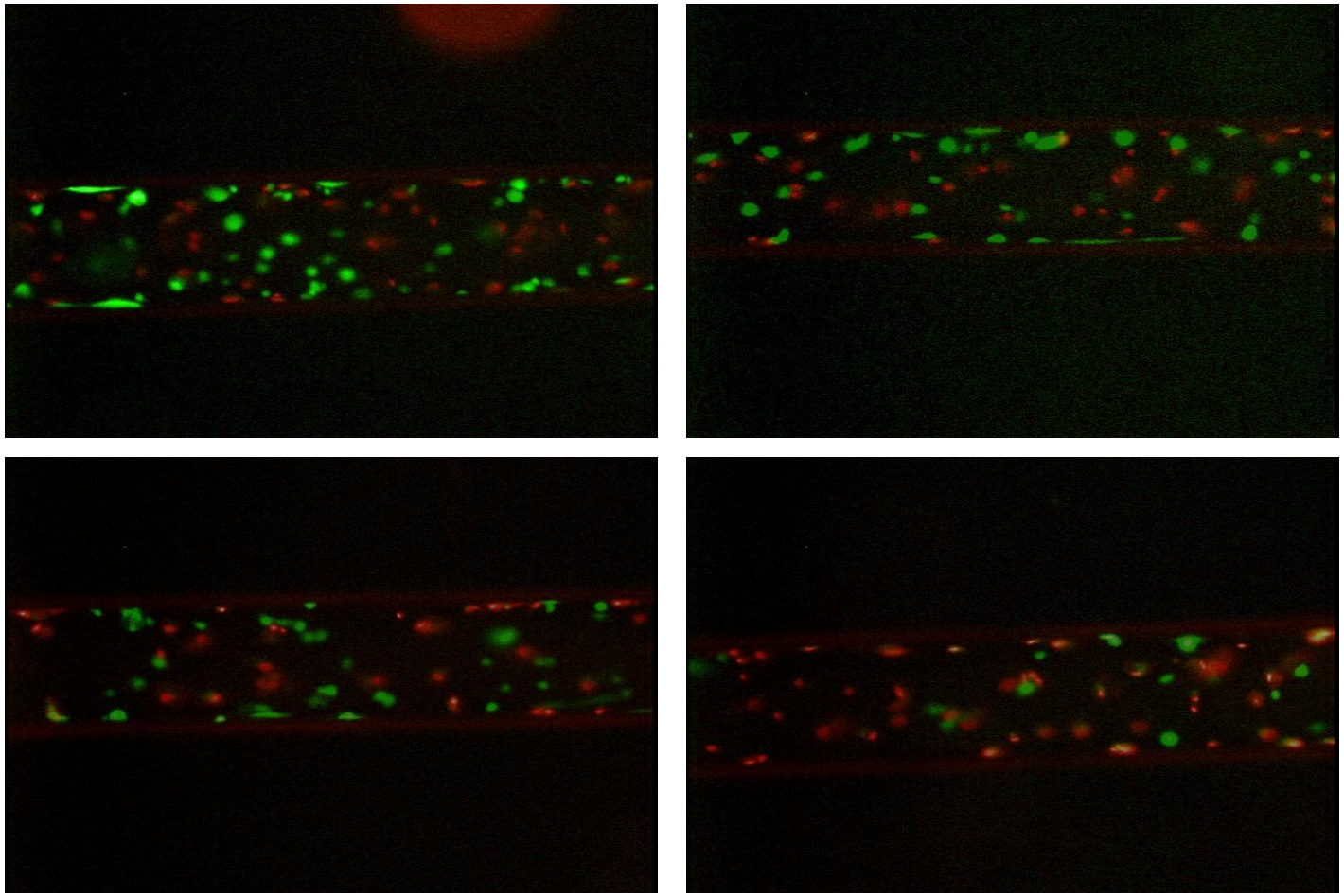

Figure 4.7: A less successful attempt at endothelialization of the microchannel.

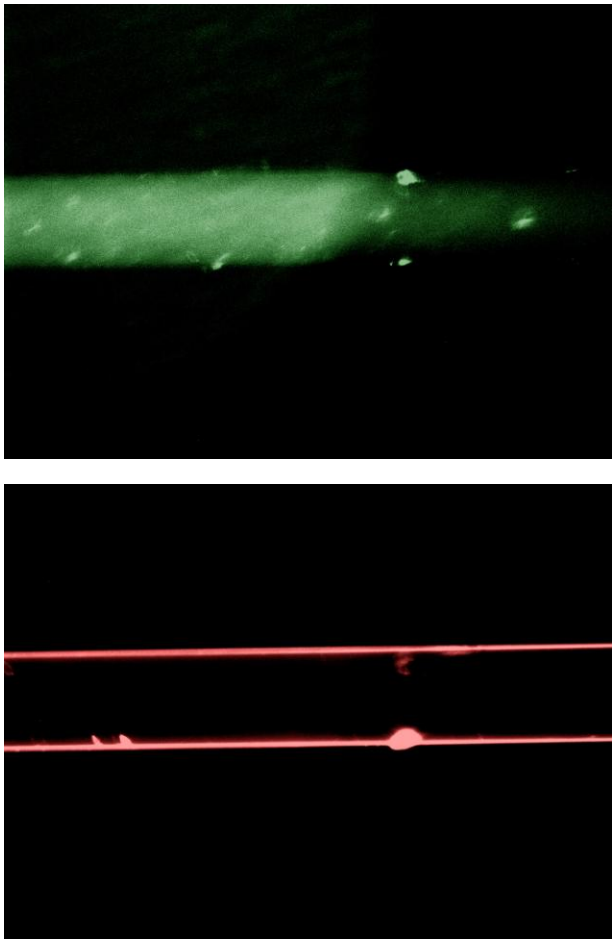

Figure 4.8: Example of cell viability test results for bubble motion inducing high shear stress. (a lot of cells have been detached, leaving very few as shown)

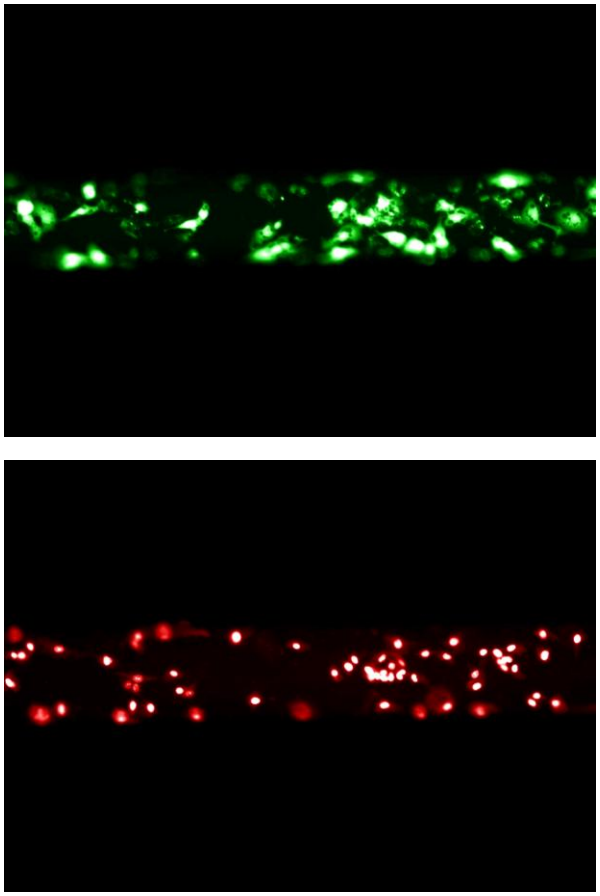

Figure 4.9: Example of cell viability test results for bubble motion inducing low shear stress. (fewer cells have been detached)

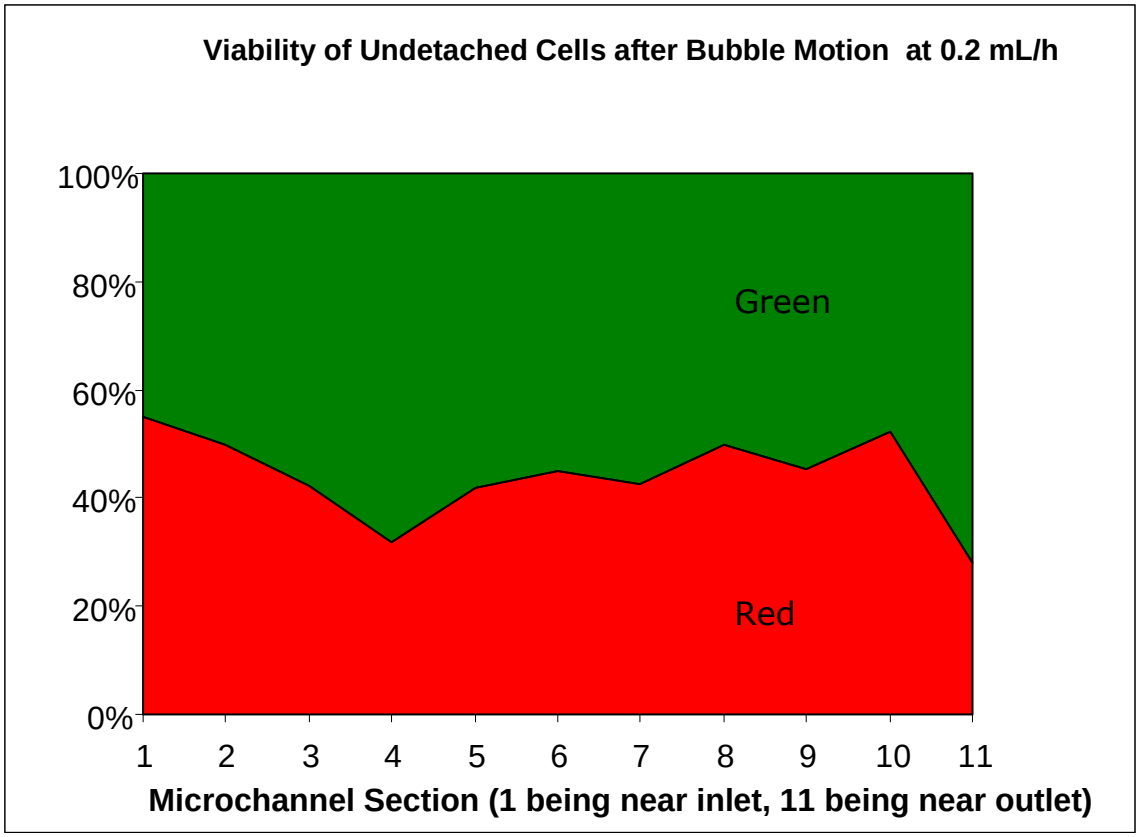

Figure 4.10: Viability of cells counted from images taken at different sections along the microchannel length.

References

1. Armentano, R.L., et al., *An in vitro study of cryopreserved and fresh human arteries: a comparison with ePTFE prostheses and human arteries studied non-invasively in vivo.* Cryobiology, 2006. **52**(1): p. 17-26.

2. Bouakaz, A., M. Versluis, and N. de Jong, *High-speed optical observations of contrast agent destruction.* Ultrasound Med Bio, 2005. **31**(3): p. 391-399.

3. Bown, M.R., J.M. MacInnes, and R.W.K. Allen, *Micro-PIV simulation and measurement in complex microchannel geometries.* Meas Sci Technol, 2005. **16**(3): p. 619-626.

4. Brayman, A.A., L.M. Lizotte, and M.W. Miller, *Erosion of artificial endothelia in vitro by pulsed ultrasound: Acoustic pressure, frequency, membrane orientation and microbubble contrast agent dependence.* Ultrasound Med Bio, 1999. **25**(8): p. 1305-1320.

5. Bretherton, F.P., *The Motion Of Long Bubbles In Tubes.* Journal Of Fluid Mechanics, 1961. **10**(2): p. 166-188.

6. Brown, X.Q., K. Ookawa, and J.Y. Wong, *Evaluation of polydimethylsiloxane scaffolds with physiologically-relevant elastic moduli: interplay of substrate mechanics and surface chemistry effects on vascular smooth muscle cell response.* Biomater, 2005. **26**(16): p. 3123-3129.

7. Brujan, E.A., *The role of cavitation microjets in the therapeutic applications of ultrasound.* Ultrasound Med Bio, 2004. **30**(3): p. 381-387.

8. Cao, T.V., et al., *Inhibitory effects of TSG-6 link module on leukocyte-endothelial cell interactions in vitro and in vivo.* Microcirc, 2004. **11**(7): p. 615-624.

9. Cloutier, G., et al., *A multimodality vascular imaging phantom with fiducial markers visible in DSA, CTA, MRA, and ultrasound.* Med Phys, 2004. **31**(6): p. 1424-1433.

10. Cokelet, G.R., et al., *Fabrication Of In-Vitro Microvascular Blood-Flow Systems By Photolithography.* Microvas Res, 1993. **46**(3): p. 394-400.

11. Cooke, B.M., et al., *A Simplified Method For Culture Of Endothelial-Cells And Analysis Of Adhesion Of Blood-Cells Under Conditions Of Flow.* Microvas Res, 1993. **45**(1): p. 33-45.

12. Damiano, E.R., D.S. Long, and M.L. Smith, *Estimation of viscosity profiles using velocimetry data from parallel flows of linearly viscous fluids: application to microvascular haemodynamics.* J Fluid Mech, 2004. **512**: p. 1-19.

13. Damiano, E.R. and T.M. Stace, *Flow and deformation of the capillary glycocalyx in the wake of a leukocyte.* Phys Fluids, 2005. **17**(3).

14. Dhoot, N.O. and M.A. Wheatley, *Microencapsulated Liposomes in controlled drug delivery: Strategies to modulate drug release and eliminate the burst effect.* J Pharm Sci, 2003. **92**(3): p. 679-689.

15. Egginton, S. and M. Gerritsen, *Lumen formation - In vivo versus in vitro observations.* Microcirc, 2003. **10**(1): p. 45-61.

16. Frame, M.D. and I.H. Sarelius, *Flow-induced cytoskeletal changes in endothelial cells growing on curved surfaces.* Microcirc, 2000. **7**(6): p. 419-427.

17. Frame, M.D.S. and I.H. Sarelius, *A System for Culture of Endothelial Cells in 20-50 um Branching Tubes.* Microcirc, 1995. **2**: p. 377-385.

18. Fung, Y.C., *Biomechanics: Mechanical Properties of Living Tissues*. 1993: Springer-Verlag.

19. Gray, B.L., et al., *Microchannel platform for the study of endothelial cell shape and function.* Biomed Microdev, 2002. **4**(1): p. 9-16.

20. Harding, S.I., et al., *Engineering and cell attachment properties of human fibronectin-fibrinogen scaffolds for use in tissue engineered blood vessels.* Bioprocess And Biosystems Engineering, 2002. **25**(1): p. 53-59.

21. Hernandez, M.R., et al., *Evaluation of effects of rofecoxib on platelet function in an in vitro model of thrombosis with circulating human blood.* Eur J Clin Invest, 2004. **34**(4): p. 297-302.

22. Itoh, Y., et al., *Platelet adhesion to aortic endothelial cells in vitro after thrombin treatment: Observation with video-enhanced contrast microscopy.* Thromb Res, 1998. **91**(1): p. 15-21.

23. Kaihara, S., et al., *Silicon micromachining to tissue engineer branched vascular channels for liver fabrication.* Tissue Eng, 2000. **6**(2): p. 105-117.

24. King, K.R., et al., *Biodegradable microfluidics.* Adv Mater, 2004. **16**(22): p. 2007-+.

25. Kohl, M.J., et al., *An experimental investigation of microchannel flow with internal pressure measurements.* Int J Heat Mass Tran, 2005. **48**(8): p. 1518-1533.

26. Laurent, S., et al., *Elastic-Modulus Of The Radial Artery Wall Material Is Not Increased In Patients With Essential-Hypertension.* Arteriosclerosis And Thrombosis, 1994. **14**(7): p. 1223-1231.

27. Lindner, J.R., et al., *Noninvasive imaging of inflammation by ultrasound detection of phagocytosed microbubbles.* Circulation, 2000. **102**(5): p. 531-538.

28. Long, D.S., et al., *Microviscometry reveals reduced blood viscosity and altered shear rate and shear stress profiles in microvessels after hemodilution.* Proc Nat Acad Sci, 2004. **101**(27): p. 10060-10065.

29. McEvoy, F.J., et al., *An In-Vitro Circulation Model For Thrombosis - Influence Of Circulating Plasmas On The Binding Of Monoclonal-Antibodies To Human Fibrin Clots.* Fibrinolysis, 1995. **9**(5): p. 309-315.

30. Peirce, S.M. and T.C. Skalak, *Microvascular remodeling: A complex continuum spanning angiogenesis to arteriogenesis.* Microcirc, 2003. **10**(1): p. 99-111.

31. Poepping, T.L., et al., *A thin-walled carotid vessel phantom for doppler ultrasound flow studies.* Ultrasound Med Bio, 2004. **30**(8): p. 1067-1078.

32. Price, R.J., et al., *Delivery of colloidal, particles and red blood cells to tissue through microvessel ruptures created by targeted microbubble destruction with ultrasound.* Circulation, 1998. **98**(13): p. 1264-1267.

33. Pukacki, F., et al., *The mechanical properties of fresh and cryopreserved arterial homografts.* European Journal Of Vascular And Endovascular Surgery, 2000. **20**(1): p. 21-24.

34. Rickard, A., et al., *Measurement of the motility of endothelial cells in confluent monolayers.* Microcirc, 2003. **10**(2): p. 193-203.

35. Satcher, R., C.F. Dewey, and J.H. Hartwig, *Mechanical remodeling of the endothelial surface and actin cytoskeleton induced by fluid flow.* Microcirc, 1997. **4**(4): p. 439-453.

36. Secomb, T.W., R. Hsu, and A.R. Pries, *Blood flow and red blood cell deformation in nonuniform capillaries: Effects of the endothelial surface layer.* Microcirc, 2002. **9**(3): p. 189-196.

37. Shin, M., et al., *Endothelialized networks with a vascular geometry in microfabricated poly(dimethyl siloxane).* Biomed Microdev, 2004. **6**(4): p. 269-278.

38. Skyba, D.M., et al., *Direct in vivo visualization of intravascular destruction of microbubbles by ultrasound and its local effects on tissue.* Circulation, 1998. **98**(4): p. 290-293.

39. Smith, M.L., et al., *Near-wall mu-PIV reveals a hydrodynamically relevant endothelial surface layer in venules in vivo.* Biophys J, 2003. **85**(1): p. 637-645.

40. Sukavaneshvar, S., K.A. Solen, and S.F. Mohammad, *An in-vitro model to study device-induced thrombosis and embolism: Evaluation of the efficacy of tirofiban, aspirin, and dipyridamole.* Thromb Haemost, 2000. **83**(2): p. 322-326.

41. Szuwart, T., et al., *Vitamin E reduces platelet adhesion to human endothelial cells in vitro.* Am J Hematol, 2000. **65**(1): p. 1-4.

42. Tho, P., et al. *Measurement of microbubble-induced acoustic microstreaming using micro particle image velocimetry*. in *Biomed Applications Micro- & Nanoengineering II*. 2005.

43. Tsukada, K., et al., *Direct measurement of erythrocyte deformability in diabetes mellitus with a transparent microchannel capillary model and high-speed video camera system.* Microvas Res, 2001. **61**(3): p. 231-239.

44. Ueda, A., et al., *Effect of shear stress on microvessel network formation of endothelial cells with in vitro three-dimensional model.* Am J Physiol -Heart C, 2004. **287**(3): p. H994-H1002.

45. Unger, E.C., et al., *In vitro studies of a new thrombus-specific ultrasound contrast agent.* Am J Cardiol, 1998. **81**(12A): p. 58G-61G.

46. Van Wamel, A., et al., *Micromanipulation of endothelial cells: Ultrasound-microbubble-cell interaction.* Ultrasound Med Bio, 2004. **30**(9): p. 1255-1258.

47. Weller, G.E.R., et al., *Modulating targeted adhesion of an ultrasound contrast agent to dysfunctional endothelium.* Ann Biomed Eng, 2002. **30**(8): p. 1012-1019.

48. Yamada, M., et al., *Continuous cell partitioning using an aqueous two-phase flow system in microfluidic devices.* Biotech Bioeng, 2004. **88**(4): p. 489-494.

49. Yasu, T., et al., *Activated leukocytes and endothelial cells enhance retention of ultrasound contrast microspheres containing perfluoropropane in inflamed venules.* Int J Cardiol, 2005. **98**(2): p. 245-252.

50. Zohar, Y., et al., *Subsonic gas flow in a straight and uniform microchannel.* J Fluid Mech, 2002. **472**: p. 125-151.

Chapter 5

Conclusions

This chapter will provide a recapitulation of the salient points discussed in the preceding chapters, as well as propose suggestions for future work.

The evolution of a bubble formed from droplet vaporization triggered by a single pulse of ultrasound was investigated experimentally by imaging the details of evolution via an ultra-high speed camera system. The experiments were conducted under two types of temperature conditions --- physiological and room, the former being important in consideration of the potential medical application of ADV for gas embolotherapy, while the latter being useful in elucidating the fundamental science behind the phenomenon of ADV.

With the boiling point of DDFP below physiological temperature, seeing a droplet vaporize into a full-blown bubble was to be expected. The experiments revealed critical information such as the observable details of the nucleation, explosive initial growth and a subsequent, more controlled growth into a spherical gas bubble. The average experimental value of 5.05 for the radial expansion ratio matched well with the theoretical ratio of 5.27,

and it was found to be independent of the initial droplet size, the acoustic pressure as well as the number of cycles in the acoustic pulse.

Such knowledge about the bubble expansion ratio can help predict whether the DDFP bubble will extend through more than one generation of capillary network, which might be critical for the bubble lodging.

Careful examination of the bubble evolution, in particular the radial growth rate, led to the proposition of an experimental law of 4-stage growth for physiological-temperature conditions. The first stage, Stage I, of the evolution is explosive with a linear growth rate and only lasts about 1.5 microsecond. The bubble will still grow linearly in Stage II but at a lower rate of 3.56 m/s on average. In Stage III, which starts from about 3.5 to 7 microseconds into the ADV process, bubble expansion proceeds proportionally with the square root of time. Non-dimensionalization of the equation has revealed that the Stage III growth rate also varies inversely with the square root of the initial droplet radius. Stage IV growth is asymptotically slow as the bubble approaches towards its maximum size.

A substantial part of the discussions was spent on whether the one can assume phase change is completed before the bubble of gas begins its expansion. While the jury is still out on this issue, the discussions have highlighted several experimental nuggets of evidence to weaken the assumption. The validity of the assumption, or otherwise, will determine whether the proposed experimental law can be related to the established models of inertia-controlled and heat-transfer-controlled bubble growth. In

addition, this assumption of phase change will affect the accuracy of computational / theoretical models that relies on it.

Comparison of the experimental results was made with a published computational model that used direct numerical simulations involving a fixed-grid, sharp-interface, moving boundary method. A simplified theoretical model was derived from the modified Bernoulli equation and compared with the experimental results. Both the computational and theoretical models were able to predict the initial growth rate with reasonable accuracy. But they both over-predict the expansion ratio initially, due to an overshoot in the growth, followed by a series of collapse-growth oscillations, which will, however, eventually lead to a final expansion ratio quite similar to the experimental value, albeit over a longer timeframe than that of the experimental.

The computational model had assumed rather arbitrary initial pressure values, with the expectation that experimental data would provide feedback in calibrating the model. The experiments themselves had parameters that did not match those in the computational model, for example, the tube length, number of open ends, other minor losses in the feeder tubings, etc.

The theoretical model, despite its relative simplicity, can predict the growth rate and final expansion ratio, but it breaks down whenever the bubble expands and approaches the wall. This is a result of the theoretical assumption to neglect flow details near the bubble surface. Thus, the theoretical model will be more suitable in predicting the evolution of smaller droplets that do not grow big enough to be near the wall.

Under room-temperature conditions, bubble evolution did not reach anywhere near the expansion ratio of 5. The bubble expansion proceeded rather quickly and overshot to reach a maximum ratio of 1.43 on average, before oscillating down to a final ratio of only 1.13 on average. Details shown in the images were different from those seen for the physiological-temperature expansion. The final product appeared to be a gas bubble suspended in some liquid DDFP (the liquid was perhaps unconsumed, or perhaps re-condensed).

It was determined that the bubble growth rate under room-temperature conditions, 2.70 m/s on average, was lower than the growth rate under physiological-temperature conditions.

The interesting phenomena of coalescence and bubble contact with the wall were observed in some cases. The average approach speed of the bubble towards a neighboring bubble or a wall was estimated to be about 0.32 m/s. Given that the ultimate goal is to lodge bubbles in the vasculature, it will be useful to know how coalescence works in creating larger bubbles that might or might not lodge.

An important prediction of the computational model is the stresses due to the expanding and collapsing bubble, and the implications of potential damage to endothelial cells. The experimental results for physiological temperature have shown no bubble collapse. In a clinical setting, if the presence of nearby, pre-existing occluding bubbles (or other factors causing heavy damping) results in the lack of collapse in expanding bubbles, the

absence of high shear stress known to be associated with the collapse process will likely lead to less cellular damage.

Possible mechanisms (which might or might not be mutually exclusive) at work during ADV include the cavitation within the DDFP, the rupture of the albumin shell, and cavitation of the liquid surrounding the encapsulated droplet. The experimental results have demonstrated the occurrence of cavitation within the DDFP but it remains unclear whether there is (complete or incomplete) rupture of the albumin shell, and whether cavitation of the surrounding liquid (beyond the field of view of the experimental images) is possible.

In view of all above-mentioned discussions and arguments, future work proposed for investigating bubble evolution can be described in the three categories of experimental, computational and theoretical work:

<u>Experimental</u>

- Determine the Stage I growth rate, by concentrating more or all of the image frames within the initial 1.5μs. This is within the capabilities of the ultra-high speed camera, although the lack of sufficient light to differentiate details in the image might pose a challenge
- Investigate whether the albumin shell of the droplet breaks completely or incompletely during ADV. This factor is important in understanding the mechanics of the evolution, since the shell could provide additional resistance against expansion and contribute towards damping of bubble oscillations.

- Conduct a systematic study of the effect of temperature on the bubble evolution, which might provide more information on understanding the thermodynamics behind the droplet vaporization and subsequent bubble evolution
- Investigate whether the DDFP is completely consumed in the case of room-temperature bubble evolution, which might also help elucidate the thermodynamics of ADV
- If a rigid tube of smaller diameter and with suitable optical, acoustical and mechanical properties can be found or fabricated, investigate the contact of bubble with tube walls during the bubble evolution.
- Extend experiments to the case of bubble evolution in a flexible tube, provided that a suitable tube can be found or fabricated
- Investigate the fluid mechanics of flow near the wall, or near neighboring particles, or in a bifurcation, during droplet vaporization and subsequent bubble evolution. Particle-image velocimetry (PIV) might be a useful tool for this investigation.
- Imaging experiments have so far been done with a droplet in a stationary flow. To mimic in vivo conditions, imaging a droplet moving with flow will be desirable (but this involves huge technical hurdles with the optics and acoustics).

<u>Computational and Theoretical</u>

- If the experimental parameters could be changed to better match the computational model's parameters, calibrate the computational model by

testing different initial bubble pressures until a match of the terminal size from experiment is found

- Investigate whether using a different time scale for the computational model improves its accuracy.
- If possible, relax the model's assumption of phase change being completed before bubble expansion. This might require a combination of two different models --- one for the evaporation process, the other for the expansion process.
- Improve the theoretical model to include terms for minor losses. The experimental setup can also be made as idealized as possible (e.g. by reducing any unnecessary tube length or flow connectors) to aid comparison of experimental results with the theoretical solution.

Besides studying the evolution of bubbles in the aforementioned work, research efforts were also put into the design of a benchtop model of a microvessel. This was motivated by the need for a microvascular model that could be used in our ongoing research in gas embolotherapy.

The design process was explained in detail. First, the advantages and disadvantages of previous benchtop microvascular models were discussed. The desired characteristics and functionalities of the ideal model were also discussed. An explanation of the rationale behind our method of microchannel fabrication, and its pros and cons, was provided. The method of endothelialization was described in detail, and images from brightfield and fluorescent microscopy, together with cell-viability test results, were used to prove the viability of the model. A simple bubble motion experiment was

carried out to demonstrate the feasibility of the benchtop microvascular model.

The following improvements to the benchtop microvascular model can form part of future work:

- Provide evidence that the morphology of the endothelial cells within the microchannel is similar to in vivo. One way is to stain with silver nitrate to identify cell shape [4, 5]. Another way is to check for confluence by stain for gap junctions with connexin 43 [2, 3] or to test whether the monolayer of cells supports cytokine-mediated leukocyte rolling [1]. The Z-drive and MetaMorph software on the Nikon microscope can capture multiple focal-depth images and re-construct them into a 3D-like image, which might reveal more details of the success of endothelialization.
- Characterize fluid mechanics in our circular-lumen microchannel vis-à-vis those with rectangular or elliptical cross-sections, so as to substantiate the benefits of having a circular lumen.
- Apply silanization to the 30μm diameter wire before covering with PDMS, so that it might be easier to extract the wire from the cured PDMS (although finding sufficiently small needles to insert into the 30μm microchannel will be another challenge).

In all, many questions remain to be answered in the research of gas embolotherapy and its associated science.

References

1. Alon, R. and K. Ley, *Cells on the run: shear-regulated integrin activation in leukocyte rolling and arrest on endothelial cells.* Current Opinion In Cell Biology, 2008. **20**(5): p. 525-532.

2. Johnson, T.L. and R.M. Nerem, *Endothelial connexin 37, connexin 40, and connexin 43 respond uniquely to substrate and shear stress.* Endothelium-Journal Of Endothelial Cell Research, 2007. **14**(4-5): p. 215-226.

3. Li, A.F. and S. Roy, *High Glucose-Induced Downregulation of Connexin 43 Expression Promotes Apoptosis in Microvascular Endothelial Cells.* Investigative Ophthalmology & Visual Science, 2009. **50**(3): p. 1400-1407.

4. Shi, Q., et al., *Evidence for circulating bone marrow-derived endothelial cells.* Blood, 1998. **92**(2): p. 362-367.

5. Wu, M.H.D., et al., *Histologic observation of continuity of transmural microvessels between the perigraft vessels and flow surface microostia in a porous vascular prosthesis.* Annals Of Vascular Surgery, 1996. **10**(1): p. 11-15.

Appendix A

Calibration Data for Ultrasound Transducer

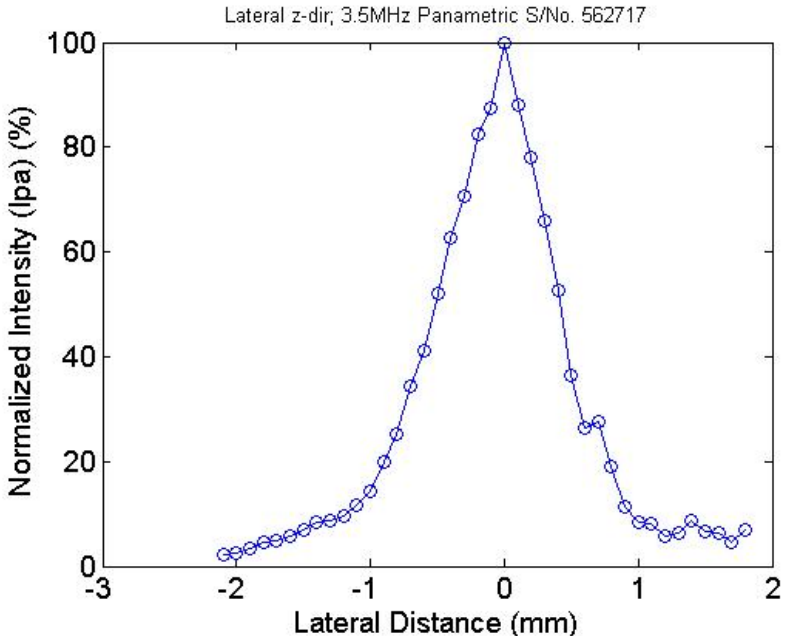

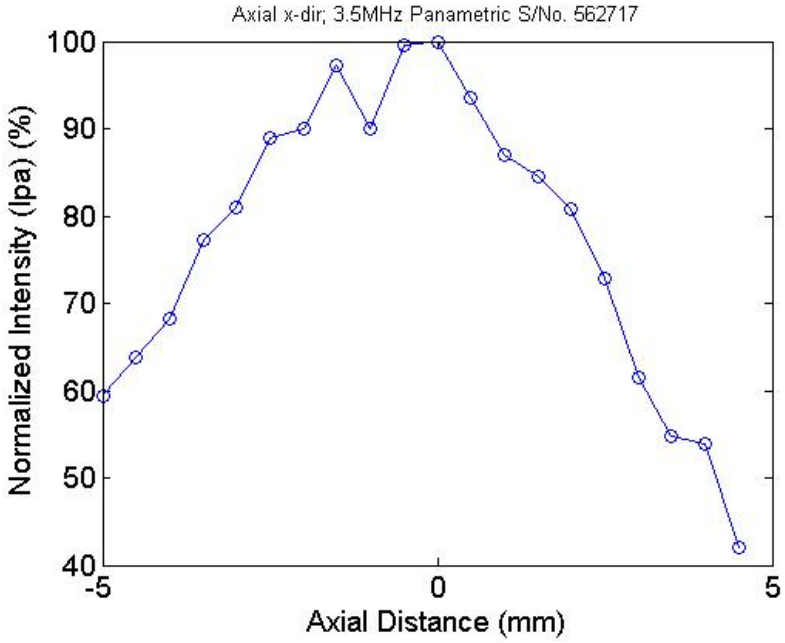

Appendix A (continued)

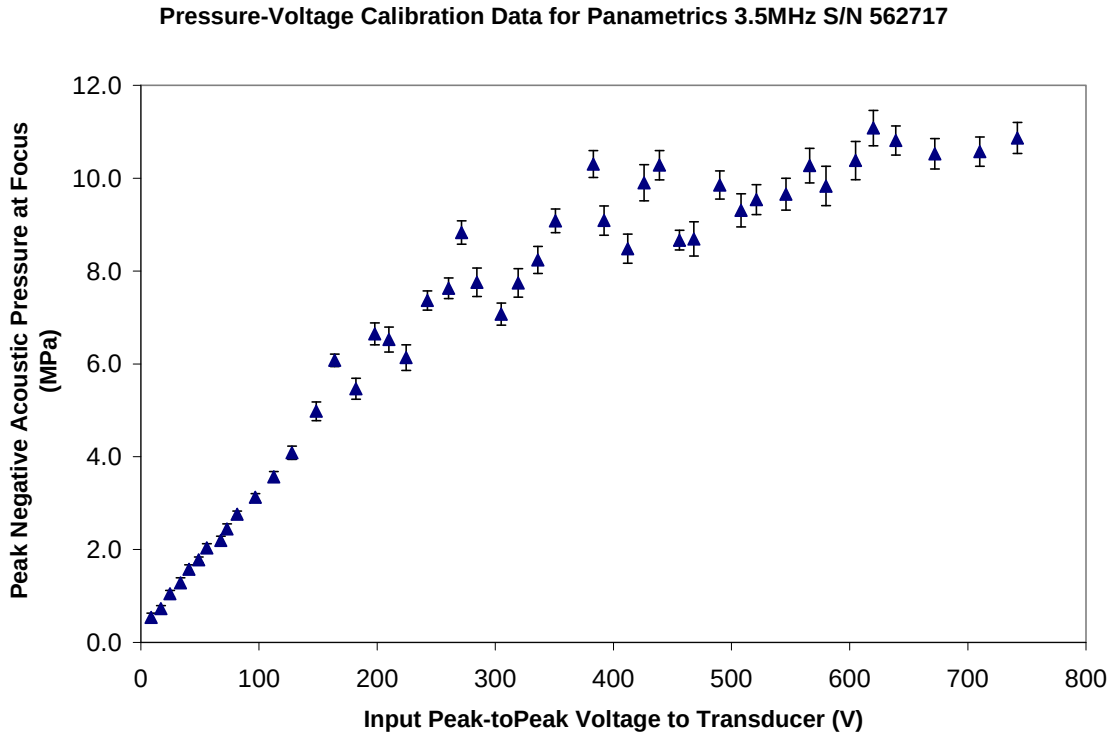

Appendix B

Expected (Theoretical) Expansion Ratio

Applying Young-Laplace equation across the interface of the final bubble with pressure P_B and radius R_f, we have

$$P_B - P_{atm} = \frac{2\sigma}{R_f}$$

Using ideal gas law, $P_B = \frac{nR_{gas}T}{4/3\,\Pi R_f^{\,3}}$

and applying conservation of mass between the liquid DDFP in the droplet of radius R_i and the DDFP gas in the bubble gives:

$$\frac{nR_{gas}T}{4/3\,\Pi R_f^{\,3}} - P_{atm} = \frac{2\sigma}{R_f}$$

With the DDFP liquid density as 1660 kgm^{-3}, atmospheric pressure as 101325 Pa, surface tension of DDFP gas and water as 70 mN/m, and R_g = 8.314 $Jmol^{-1}K^{-1}$, we get a cubic equation:

$$1.486\times10^{7}\,\frac{R_i^{\,3}}{R_f^{\,3}} - 101325 = \frac{2(70\times10^{-3})}{R_f}$$

Solving this cubic equation numerically in Mathematica for different values of R_i, we arrive at $\mathbf{R_f = 5.27R_i}$

Appendix C

T-Test Scores for Figures 2.10 to 2.12

At 7.7 MPa				T-Test p value					
No. Cycles	Exp Ratio	Std Dev		4	7	10	14		
4	5.06	0.088444		NA	0.180	0.437	0.762		
7	5.01	0.067961			NA	0.122	0.299		
10	5.09	0.037594				NA	0.805		
14	5.07	0.094202					NA		
All acoustic pressures				T-Test p value					
No. Cycles	Exp Ratio	Std Dev		3	4	7	10	14	17
3	5.03	0.117652		NA	0.573	0.730	0.467	0.597	0.808
4	5.07	0.105262			NA	0.047	0.708	0.924	0.649
7	5.01	0.067682				NA	0.199	0.304	0.370
10	5.09	0.121375					NA	0.823	0.525
14	5.07	0.094202						NA	0.696
17	5.05	0.064227							NA
				T-Test p value					
M-Pa	Exp Ratio	Std Dev		4.7	6.1	7.7	9.9	10.8	
4.7	5.10	0.135921		NA	0.246	0.481	0.247	0.722	
6.1	5.01	0.057512			NA	0.150	0.828	0.011	
7.7	5.05	0.08309				NA	0.361	0.055	
9.9	5.00	0.132814					NA	0.052	
10.8	5.12	0.086662						NA	

Appendix D

Simplified model of bubble expansion in a tube

Modified Bernoulli equation (obtain same results if start from conservation of momentum too)

$$\rho\int_{l_1}^{l_2}\frac{\partial\overline{V}}{\partial t}ds+\rho g h_L=P_1-P_2 \qquad (1)$$

P=pressure, $\overline{V}$ = cross-sectional average velocity, s is streamline coordinate, ρ=liquid density, g=acceleration due to gravity, and h_L = head loss

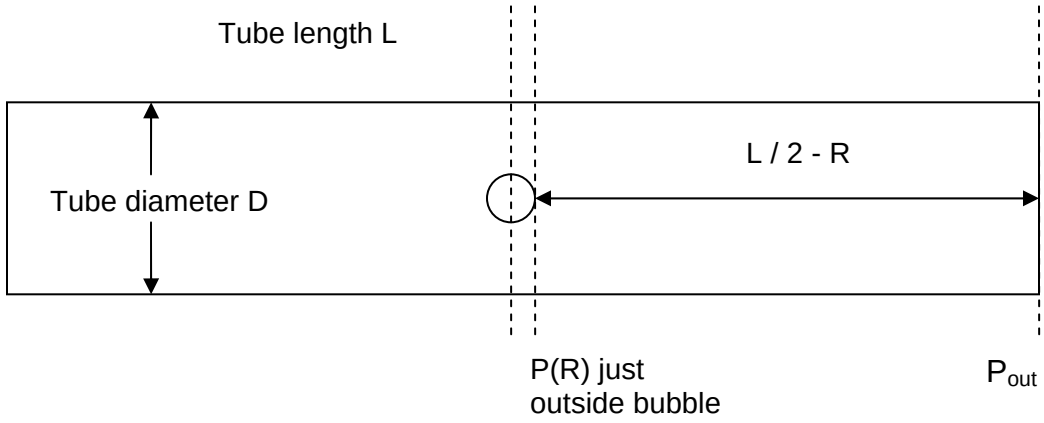

Apply between point ~ at bubble surface to tube outlet, e.g. R to L/2

Assume laminar flow in liquid between bubble and tube outlet to estimate head loss term.

$$\rho g h_L=\frac{64}{\mathrm{Re}}\frac{l}{D}\frac{\rho\overline{V}^2}{2}=\frac{32\mu}{D^2}\left(\frac{L}{2}-R\right)\overline{V} \qquad (2)$$

Where D=tube diameter, R=bubble radius, L=tube length.

Conservation of mass for entire tube

$$\frac{d}{dt}\left[\frac{L\pi D^2}{4}-\frac{4\pi R^3}{3}\right]=-\beta Q=-\beta\bar{V}\frac{\pi D^2}{4} \qquad (3)$$

where β is the number of outlets (1 or 2)

Rearranging yields

$$\bar{V}=\frac{16}{\beta D^2}R^2\frac{dR}{dt} \qquad (4)$$

$$\frac{d\bar{V}}{dt}=\frac{16}{\beta D^2}\left[R^2\frac{d^2R}{dt^2}+2R\left(\frac{dR}{dt}\right)^2\right] \qquad (5)$$

Pressure jump at the bubble interface (Young-Laplace for moving interface)

$$P(R)=P_{B0}\left(\frac{R_0}{R}\right)^{3\gamma}-\frac{4\mu}{R}\frac{dR}{dt}-\frac{2\sigma}{R} \qquad (6)$$

where P(R) is pressure in the liquid at the bubble surface, P_{B0} is initial bubble pressure, gamma = 1 for isothermal expansion (used) or 1.4 for adiabatic expansion, R_0 = initial bubble diameter

Substituting equations (2), (4), (5), and (6) into equation (1) yields

$$\frac{16\rho}{\beta D^2}\left(\frac{L}{2}-R\right)\left[R^2\frac{d^2R}{dt^2}+2R\left(\frac{dR}{dt}\right)^2\right]+\frac{512\mu}{\beta D^4}\left(\frac{L}{2}-R\right)R^2\frac{dR}{dt}=P_{B0}\left(\frac{R_0}{R}\right)^{3\gamma}-\frac{4\mu}{R}\frac{dR}{dt}-\frac{2\sigma}{R}-P_{out}$$

Solved with the following parameter values (modifications from these noted in graph):

ρ=993.3 kg/m^3
μ=6x10^{-4} Ns/m^2

$\sigma=70x10^{-3}$ N/m
$P_{out}=101300$ Pa
$P_{B0}=14.6x10^{6}$ Pa
L=16cm

Assumptions:

- Ignores details of flow very close to bubble
- One-dimensional flow model
- Neglect "minor losses"
- Tube length approximation
- Some parameters approximated (e.g. P_{B0} , σ)